

MASTER OF SCIENCE THESIS

**Horizontal Axis Wind Turbine (HAWT)
wake stability investigations**
Insights Through a Vortex-Ring Modelling Approach

D. Baldacchino B.Eng.(Hons)(Melit.)

October 8, 2012

Faculty of Aerospace Engineering · Delft University of Technology

**Horizontal Axis Wind Turbine (HAWT)
wake stability investigations
Insights Through a Vortex-Ring Modelling Approach**

MASTER OF SCIENCE THESIS

For obtaining the degree of Master of Science in Sustainable Energy
Technology at Delft University of Technology

D. Baldacchino B.Eng.(Hons)(Melit.)

October 8, 2012



The research work disclosed in this publication is partially funded by the Strategic Educational Pathways Scholarship (Malta). This scholarship is part-financed by the European Union - European Social Fund (ESF) under Operational Programme II - Cohesion Policy 2007-2013, "Empowering People for More Jobs and a Better Quality of Life".



Operational Programme II - Cohesion Policy 2007-2013
*Empowering People for More Jobs and a Better Quality of
Life*

Scholarship part-financed by the European Union
European Social Fund (ESF)
Co-financing rate: 85% EU Funds; 15% National Funds



Investing in your future



Copyright © D. Baldacchino B.Eng.(Hons)(Melit.)
All rights reserved.

DELFT UNIVERSITY OF TECHNOLOGY

DELFT UNIVERSITY WIND ENERGY RESEARCH INSTITUTE (DUWIND)

The undersigned hereby certify that they have read and recommend to the Faculty of Aerospace Engineering for acceptance a thesis entitled “**Horizontal Axis Wind Turbine (HAWT) wake stability investigations**” by **D. Baldacchino B.Eng.(Hons)(Melit.)** in partial fulfillment of the requirements for the degree of **Master of Science**.

Dated: October 8, 2012

Head of department and Supervisor:

prof.dr. G.J.W. van Bussel

Reader:

dr. ir. C.J. Simão Ferreira

Reader:

dr. ir. L.L.M. Veldhuis

Summary

As wind energy technology continues to take the helm of renewable energy deployed throughout the world, and wind farms become a more common sight on the horizon, increased emphasis is placed on wind farm aerodynamics. Obtaining insight into this complex flow problem requires a deeper understanding of the nature of individual wind turbine wakes, and subsequently wake interactions.

The topic of wake stability and wake meandering, has received particular attention in recent years. Recent work by Larsen et al. [1] investigated this wake meandering phenomenon based on the hypothesis that the wake behaves as a passive tracer, governed by large-scale lateral and horizontal turbulent components. In contrast, Medici and Alfredsson [2] propose that a meandering mechanism similar to bluff body vortex shedding is responsible for the wake oscillations of their two-bladed model. Thus conflicting views with respect to the triggering mechanisms of wake instability exist and are addressed in this thesis.

The approach taken was to use a simple inviscid vortex ring (VR) modelling method to represent the developing rotor wake. This allows for a straight forward investigation and comparison of the impact of uniform, yawed and sheared flow conditions on the development of the wake, with the additional possibility of including ground effect. The phenomenon of vortex filament interaction or *leapfrogging*, could play a role in the observation of unsteady phenomena and is therefore also addressed. Such a study is hence performed in light of recent conflicting views on the causes of wake meandering.

The main conclusion from this study is that the presence of the ground and external perturbations, most notably changes in the wake pitch and the rotor thrust coefficient, can significantly affect the steady development of the wake. The phenomenon of vortex filament leapfrogging, whilst displaying interesting periodic behaviour, does not correlate with periodic wake behaviour reported in Medici et al. [2]. However, in the absence of unsteady inflow, it is shown that the wake of a Horizontal Axis Wind Turbine (HAWT) is certainly prone to displaying unstable, dynamic behaviour caused by these additional factors.

The main results of this thesis have been published in the open access proceeding of the The Science of Making Torque, Oldenburg, 2012:

D Baldacchino and G J W van Bussel 2014 J. Phys.: Conf. Ser. 555 012111.

Acknowledgements

First and foremost, I wish to thank my supervisor, Prof. dr. Gerard van Bussel. His vision and enthusiasm was unwavering throughout the course of my thesis project. Most of all, I greatly appreciated his role as a mentor and for taking a sincere interest in my ambitions and personal development.

I am indebted to Dr. Ing. Tonio Sant for encouraging me to come to Delft for my post-graduate studies, and for always taking an interest in my work. Once again I am deeply grateful to Mr. Daniel Micallef. You never thought twice about offering your advice or sharing enthusiasm about different topics and ideas. Thanks also to dr. ir. Carlos Ferreira for taking an interest in my project.

The two year SET master programme at TU Delft has delivered much more than it promised. New friendships made and old ones strengthened. Life lessons learnt and experiences had. I have to thank and acknowledge a true friend, Teysis. We have lived many moments together these last couple of years, and I hope many more will follow in the future. Mitsos, Kokstas, I enjoyed my best times in Delft with you and you helped make this a memorable experience.

To all my friends back home, meeting you twice a year is a great injustice, but we built friendships to last, and knowing you are always there, is the best comfort in the world.

I would also like to thank Ms. Mirjam van der Geur for her complete support throughout the master programme, on both a personal and academic level.

I would also like to take this opportunity to thank Mrs. Janatha Stubbs, for her deep generosity and belief in me and my passion. Her financial assistance helped pave a smoother path to my master completion. Above all, thank you for taking a sincere interest in my choice of study.

To my extended family here in the Netherlands, the Roelse's and the Tienhoven's. You welcomed us with open arms and treated us so well. It made our experience in the Netherlands that bit more special. Thank you.

Completing my studies would not have been possible, were it not for my girlfriend, Martina. We thought we had been through a lot, then we came to Delft! You helped me

through troubling times with unconditional love, and I owe what I have accomplished here to you. You're a star.

Last, but definitely not least, to my mum and dad, my best friends. Your unconditional love and support through thick and thin, allowing me to follow my dreams at the expense of your own, and to be my own person - no son could wish for more. No words can come close, but thank you. And to Wallace, although you'll never read this, I couldn't have made it without your own unconditional love and sense of humour!

Delft, The Netherlands
October 8, 2012

D. Baldacchino B.Eng.(Hons)(Melit.)

*"If I have seen further, it is by
standing on the shoulder of giants."*

– **Sir Isaac Newton, 1675**

Contents

Summary	v
Acknowledgements	vii
List of Figures	xv
List of Tables	xvii
Nomenclature	xix
1 Introduction	1
1.1 Research in Wind Energy	1
1.2 Thesis Motivation and Research Goals	2
1.3 Thesis Outline	4
2 Wind Turbine Wake Stability	5
2.1 Large scale turbulence as a driver for wake meandering	5
2.1.1 Controlled scaled experiments	5
2.1.2 Meandering modelling studies	6
2.1.3 Open field validation and observations	7
2.2 Intrinsic-instabilities as a driver of wake meandering	7
2.2.1 Controlled experiments - The KTH experiments	7
2.2.2 Modelling considerations	9
2.3 Wake Stability Studies	9
2.3.1 Theoretical analyses	9
2.3.2 Experimental evidence	10
2.4 Conclusions	12

3	Modelling techniques	15
3.1	Characterising the wake	15
3.2	Vortex Methods	16
3.2.1	Vortex ring representations	17
3.3	Navier-Stokes models	18
3.4	Far wake models	18
3.5	Applications	19
4	Development of a Free-Wake Vortex Ring Model	21
4.1	Model Conceptualisation	21
4.1.1	Underlying assumptions and simplifications	21
4.1.2	Overview of the modelling approach	22
4.2	The ideal vortex ring	23
4.2.1	Induced velocity field	26
4.3	Analytical HAWT wake model	27
4.3.1	Evaluating the induced velocities	28
4.3.2	Averaging the induced velocities	28
4.3.3	Modelling flow instabilities	29
4.3.4	The self-induced vortex ring velocity	33
4.3.5	Modelling wake expansion	36
4.3.6	Wake strength	37
4.4	Interacting vortex rings	38
4.5	Simulations Description	38
4.5.1	Discrete FW-VRM	38
4.5.2	Coupled FW-VRM interaction model	40
4.5.3	Detailed vortex ring interactions	41
4.5.4	Dealing with starting effects on the FW-VRM	41
5	Model testing and preliminary results	43
5.1	Vortex ring behaviour - induced velocity fields	43
5.1.1	Dual vortex ring system	43
5.1.2	Triple vortex ring system	44
5.2	Vortex ring interactions	47
5.2.1	Convergence to a stable solution	47
5.2.2	Mutual threading behaviour of a dual vortex ring system	47
5.2.3	Mutual threading behaviour of a triple vortex ring system	48
5.3	Vortex rings as wake elements	53
5.3.1	Actuator disk characteristics	53
5.3.2	Axial induced velocity	54

6	Results	57
6.1	Test Cases	57
6.2	Vortex ring array dynamics	57
6.2.1	Triple vortex ring array	58
6.2.2	Prescribed expanded rings	59
6.3	Leapfrogging	63
6.4	Free-Wake results	67
6.4.1	Effects of yawed inflow	67
6.4.2	Effects of a sheared inflow profile	67
6.4.3	Ground Effect	68
6.5	Detailed wake interactions	74
6.5.1	Instability in ground effect	74
7	Conclusions and recommendations	77
7.1	Conclusions	77
7.2	Recommendations	78
	References	81
A	Governing Equations	85
A.0.1	Closed form induced velocity expressions	86
A.0.2	Closed form solution of the stream function	87
A.0.3	Elliptic Integrals	87
A.1	Coordinate Systems	89
A.2	Transformation matrices	90
B	Expressions for an inclined vortex ring	93
B.0.1	Induced velocities at an arbitrary point from inclined ideal vortex rings	93
B.0.2	Combined tilting and skewing	96
C	Vortex ring approximation using straight vortex line filaments	97
C.1	Biot Savart Law for the induced velocity from a line filament	97
C.2	Correction for finite core size	98
D	Verification Trajectories of Meleshko et al. [3]	101
E	Vortex ring array velocity fields	103
F	Wake visualisations	111
F.1	Discrete FW-VRM	111
F.1.1	Starting effect on ring dynamics	111

List of Figures

1.1	Global cumulative installed wind power capacity from 1996 to 2011. <i>Source:</i> Global Wind Energy Council [4]	2
2.1	Axial velocity signal obtained in the KTH experiments. The low and high frequency peaks (f and F) signify the vortex passage and wake shift respectively [2].	8
2.2	Manual offset mechanism for the tuning of an applied wake model (b), motivated as shown in (a). <i>Source:</i> Sørensen et al. [5]	9
2.3	Experimental evidence of the leapfrogging behaviour between two coaxial vortex rings. <i>Source:</i> An Album of Fluid Motion [6].	10
2.4	Visualisation of wind turbine wakes displaying unstable characteristics . .	11
2.5	Mutual inductance mode between adjacent vortex filaments, observed for a 4-bladed propeller for an advance ratio of 0.65. <i>Source:</i> Felli et al. [7] .	12
3.1	Simplified rotor wake representation using discrete vortex rings and flow conservation. <i>Source:</i> Øye [8].	17
3.2	Wake in ground effect (top) and outside of ground effect (bottom). <i>Source:</i> Grasso [9].	20
3.3	Wake in ground effect modelling method. <i>Source:</i> Madsen et al. [10]. . . .	20
4.1	Wind turbine rotor representation	22
4.2	Wake representation due to different rotor models	23
4.3	Positive convention for the assigned ring strength Γ_i	24
4.4	Global and local coordinate system definitions	24
4.5	Coordinate System and angular definitions	26
4.6	Variation of the radial velocity of an ideal vortex ring	27
4.7	Variation of the radial velocity of an ideal vortex ring	27
4.8	Element discretisation for velocity evaluation	29

4.9	Principle of zero-boundary flow underlying the ground effect model	31
4.10	Ground effect modelling with ideal vortex rings	32
4.11	Vortex ring self-induced velocity	34
4.12	Illustration of methods to compute self-induced velocity	35
4.13	Wake expansion characteristics	37
5.1	Layout of the investigated dual vortex ring system	44
5.2	Induced velocities in the ring planes of a coaxial dual ring system	45
5.3	Induced velocities in the ring planes of an offset dual ring system	45
5.4	Induced radial velocities at the ring planes of a coaxial triple ring system	46
5.5	Induced axial velocities at the ring planes of a coaxial triple ring system	46
5.6	Convergence behaviour for the solution of equations for predicting vortex ring mutual interaction	47
5.7	Triple vortex ring system layout	48
5.8	Dual vortex ring interaction trajectories	48
5.9	Motion of a dual vortex ring system displaying approximately one leapfrog cycle	49
5.10	Spatial trajectory of a triple vortex ring system subject to small spatial (axial displacement) perturbations	51
5.11	Spatial trajectory of a triple vortex ring system subject to small strength perturbations	52
5.12	Actuator disk characteristics	53
5.13	Comparison of the analytical and VR array induced velocities in the actuator region	54
5.14	Model prediction of the average axial induced velocity for ideal operating conditions	55
6.1	Induced velocities for a triple ring system with an offset middle ring.	58
6.2	Ring trajectories for the case on an offset mid-ring.	59
6.3	Radial trajectory for an ideally expanded vortex ring array with $B = 3$; snapshots are shown at $5s$ intervals.	61
6.4	Radial trajectory for an ideally expanded vortex ring array with $B = 2$; snapshots are shown at $5s$ intervals.	62
6.5	Pitch, strength and thrust simulation parameters extracted from [2]	64
6.6	St as a function of tip speed ratio in axial flow, $U_\infty = 8.3m/s$	65
6.7	Characteristic leapfrogging frequency obtained using data extracted from Medici and Alfredsson [2]	66
6.8	Leapfrog frequency as a function of pitch and strength	66
6.9	Wake development in sheared flow	68
6.10	Wake views: <i>red line</i> - wake centreline trajectory, <i>black line</i> - projection of rotor axis. $R = 50$, $R/HH = 1.4$, $\Psi = 10^\circ$, $C_T = 0.889$	69
6.11	Wake development in sheared flow	70
6.12	Wake views: <i>red line</i> - wake centreline trajectory, <i>black line</i> - projection of rotor axis. $R = 50$, $R/HH = 1.4$, $m = 0.1$, $\Psi = 10^\circ$, $C_T = 0.889$	71

6.13	Frontal (xy plane) wake views for 6 revolutions: <i>red line</i> - wake centreline trajectory, <i>black line</i> - projection of rotor axis. $R = 50$, $R/HH = 1.4$, $C_T = 1.0$	72
6.14	Rotor in ground effect	73
6.15	Illustrations of non-uniform wake evolution due to shear and ground effect	73
6.16	Snapshots of the development of the wake in ground effect, exhibiting the mutual inductance mode, resulting from the misalignment and interaction of respective wake elements. Panels (a) through (b) are equispaced in time by $3s$; $C_T = 0.889$, $HH/R = 1.5$	76
A.1	Flow field of an ideal vortex ring	87
A.2	Complete elliptic integral characteristics, as a function of the parameter m	89
A.3	Principal Coordinate Systems	90
B.1	(<i>Left</i>) Original ring orientation with evaluation point in the $x - z$ plane; (<i>Right</i>) Transformed coordinates about ring centre (p_i, q_i)	94
B.2	Schematic showing the method for the correct root selection in eqn. B.11	95
B.3	(<i>Left</i>) Original ring orientation with evaluation point in the $y - z$ plane; (<i>Right</i>) Transformed coordinates about ring centre (p_i, q_i)	96
C.1	Vortex ring approximation using a closed loop of consecutive straight line filaments. Notation is shown for filament i for an arbitrary ring composed of n discrete vortex filaments.	98
D.1	Trajectories of a dual vortex ring system with equal and similar strength. (a) Mutual threading (b) Initial radii and ring separation constraints at various strengths giving rise to leapfrogging - shaded regions display possible combinations (c) Slip-through motion. <i>Source</i> : Meleshko et al. [3].	101
D.2	Vortex Ring trajectories computed with a fourth order Runge-Kutta estimation	102
E.1	Influence of ground effect on an array of 2 equispaced, upright IVRs; Unit strength, $HH/R = 2$	105
E.2	Influence of ground effect on an array of 2 equispaced, $-0.2rad$ IVRs; Unit strength, $HH/R = 2$	106
E.3	Influence of ground effect on an array of 2 equispaced, upright IVRs; Unit strength, $HH/R = 2$	107
E.4	Influence of ground effect on an array of 3 equispaced, $-0.2rad$ IVRs; Unit strength, $HH/R = 2$	108
E.5	Total velocity contours for a 10 ring vortex ring system in ground effect	109
F.1	Effect of unbalanced velocity field on the dynamics of the first three starting rings; $C_T = 0.889$, $m = 0.2$	112

List of Tables

4.1	Salient quantities evaluated from the analytical ideal vortex ring equations in local vortex ring coordinates	26
4.2	Disk loading characteristics	38
5.1	Parameters for testing 3-ring interaction with a variation in (a) initial ring plane separation: $\Gamma_1 = \Gamma_2 = 1$; $R_1 = R_2 = 1$ (b) initial ring strength. $R_1 = R_2 = 1$; $h_{12} = h_{23} = 1$	50
6.1	Actuator disk characteristics	57
6.2	Average axial and radial velocities at $t = 0$	58
6.3	Schematic descriptors for Figures 6.15b and 6.15a	70

Nomenclature

Latin Symbols

$a_{x,i}, a_{y,i}, a_{z,i}$	Induction velocity factors at the location of the i^{th} vortex ring	[–]
a_x, a_y, a_z	Induction velocity factors at the actuator disk	[–]
B	Number of blades	[–]
C_T	Rotor thrust coefficient	[–]
$E(m)$	Elliptic integral of the second kind	[–]
$K(m)$	Elliptic integral of the first kind	[–]
m	Wind shear exponent; elliptic integral parameter	[–]
R	Actuator disk radius	[m]
R_i	Wake vortex ring radius	[m]
Re	Reynolds Number	[–]
St	Strouhal Number	[–]
$u_{z,i}^{\mathbf{m}}, u_{r,i}^{\mathbf{m}}$	Mutual axial and radial induced velocities from i^{th} vortex ring	[m/s]
$u_{z,i}^{\mathbf{v}}, u_{r,i}^{\mathbf{v}}$	Virtual axial and radial induced velocities from the i^{th} reflected vortex ring	[m/s]
U_∞	Undisturbed upstream wind speed	[m/s]

Coordinate Systems

$\{r_i, \theta_i, z_i\}$	Local vortex ring system
$\{x, y, z\}$	Global cartesian system

Greek Symbols

β	Wake tilt angle, about the x -axis	[deg]
χ	Wake skew angle, about the y -axis	[deg]
$\Gamma, \Gamma_\theta, \Gamma_i$	Vortex ring strength	[m^2/s]
γ_θ	Wake surface vortex density	[m/s]
ψ	Streamfunction	[-]

Subscripts

∞	Represents the value of a quantity specified infinitely upstream or downstream
i	Ring number designation
max	Indicates the maximum of the associated quantity
opt	Indicates the optimum of the associated quantity

Superscripts

m	Indicating mutually induced velocity components
s	Indicating self induced velocity components
v	Indicating virtual induced velocity components

Abbreviations

BEM	Blade Element Momentum
CFD	Computational Fluid Dynamics
FW-VRM	Free Wake Vortex Ring Model
HAWT	Horizontal Axis Wind Turbine
HH	Hub Height
IGE	In Ground Effect
OGE	Outside Ground Effect
SIV	Self Induced Velocity
VR	Vortex Ring

Chapter 1

Introduction

1.1 Research in Wind Energy

The importance of addressing our climate's welfare and the prudent use of precious terrestrial resources hardly needs any introduction in this day and age.

Accessing the conventional fuels that have fuelled growth in post-industrial revolution times becomes increasingly difficult, posing higher financial burdens and altogether riskier activities, both to man and ecosystems. Harnessing wind power for satisfying an energy-hungry human race is of course, just one of a number of options at hand, as evident from heightened global efforts to harness increasingly renewable and sustainable energy resources.

These factors are some of the main drivers for the gradual growth in sustainable energy technologies such as wind power. It is thus an every day challenge to drive down costs of these green energy systems, making them more cost-competitive and ultimately, the natural choice for consumers and developers alike. The reduction of these fundamental costs is ultimately the goal of research and development in these fields of technology.

The statistics for wind energy growth are certainly encouraging, especially in light of the recent, ongoing economic downturn (see Figure 1.1). Although the market has not been completely immune to the financial crisis, wind power is still expected to perform rather steadily in the next few years to come. This is particularly true of the offshore sector. The United Kingdom for instance is set to dominate the offshore wind energy market with ambitious projects over the next few years, and offshore wind will be capable of providing in excess of 20% of the UK's electricity demand. On the European level, it is expected that wind energy will contribute approximately 16% of European electricity demands by the current target year of 2020 [11].

As the proliferation of wind energy continues, one can observe a steady trend in increasing wind farm sizes, both in the number of turbines installed per wind farm, but also in the average rated power of an individual turbine. The growth in the offshore wind sector has further consolidated these trends, where it becomes favourable to install larger

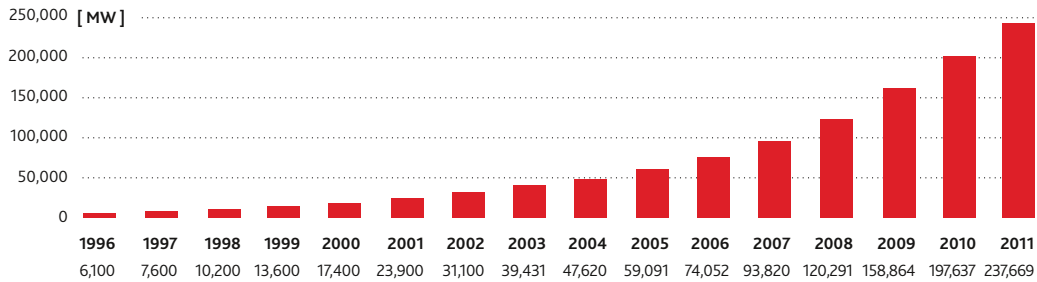


Figure 1.1: Global cumulative installed wind power capacity from 1996 to 2011. *Source:* Global Wind Energy Council [4]

wind farms at remote but attractive locations in terms of site conditions. Thus, it is of paramount importance to obtain a better understanding of wind farm aerodynamics, shifting from stand-alone rotor and wake aerodynamics, to the complex understanding of interacting wind turbine wakes. The wake of a wind turbine is that region of affected air behind the rotor, which in response to the operational regime of the turbine, will have an impact on downstream turbines. A wind turbine operating in the wake of another turbine experiences higher fatigue loading which can result in premature failure, and this indirectly leads to a higher cost of energy. Wind farm efficiency also decreases when wake effects are present.

It is therefore important to characterise and understand the development and stability of wakes since a stable wind turbine wake threatens to jeopardise the attractiveness of the resource.

1.2 Thesis Motivation and Research Goals

A number of recent findings with regards to the stability and motion of the wind turbine wake, revealed that wakes do not move steadily behind a wind turbine rotor, and rather, have a tendency to oscillate randomly, a phenomenon dubbed “wake meandering”. This is a significant observation, considering the importance of understanding wind farm behaviour in light of the aforementioned considerations.

Research by Larsen et al. [1] investigated this wake meandering phenomenon based on the hypothesis that the wake behaves as a passive tracer, governed by large-scale lateral and horizontal turbulent components. In contrast, Medici and Alfredsson [2] propose that a meandering mechanism similar to bluff body vortex shedding is responsible for the wake oscillations of their two-bladed model. Additionally, it is known that certain instability modes occur in helical vortex systems, which serve to hasten the transition from the defined near-wake region, to the far-wake [12, 7, 13, 14].

These pieces of evidence serve to highlight the uncertainty in our current understanding of the meandering phenomenon and the triggering mechanisms leading to the development of instabilities. This is what motivated the present principal research question: *what is the root cause for the observed wake meandering phenomenon?*

The underlying backbone of this thesis is therefore to investigate, using simple modelling techniques, important factors which determine the stability of wind turbine wakes.

Research Goals

The research goals of this thesis are therefore the following:

1. *Wake stability* is a key phenomenon that needs to be addressed. Simple insight into typical causes of wake deflection and instability modes is envisioned using a simple model that can capture the dynamic interaction of wake elements.
2. Pertaining to the above mentioned aim, it is desired to model the effects of yaw, shear as well as the presence of the ground on the stability of the wake.
3. The results of Medici et al. [2] are addressed from the perspective of vortex ring interactions, drawing comparisons with the mutual instability mode of parallel vortex rings. It is hypothesised that a correlation could exist between the periodicity in the two phenomena.

Approach Overview

In the context of wake meandering and stability, a simple yet physically insightful wake model is sought. As will be discussed through the first few chapters, the evidence for dynamic wake behaviour is present but rather inconclusive as to the root cause of the phenomenon.

The number of methods available for examining rotor performance and wake development are numerous: from complex Navier-Stokes codes on the one hand representing the most advanced and computationally expensive, to simple engineering models providing rapid but limited insights.

It is the aim of this thesis to take the route of vortex ring modelling to achieve the above mentioned goals. It is important to understand the motivation for this choice at the outset, in order to set the context for the first chapters of this thesis:

- ideal vortex rings are known to behave similarly to helical vortices with a fine pitch, but are particularly useful because a closed-form solution for the Biot-Savart integration exists
- the use of a discrete number of vortex rings to represent the rotor wake facilitates the description of wake dynamics through the manipulation of ring geometry and rigid-body kinematics.

It is important to clarify at the outset, that the observations made in this thesis work are mostly of a qualitative nature. Thus we are more concerned with understanding and explaining the general trends observed, rather than to accurately quantify the monitored physical quantities such as induced velocities and spatial trajectories. Notwithstanding, a physically consistent description of the problem is sought through carefully deduced assumptions and simplifications.

1.3 Thesis Outline

This thesis report is organised as follows:

- **Chapter 2** of this thesis presents some of the most pertinent studies related to the investigation of wake stability. This chapter thus further sets the tone for this thesis work;
- **Chapter 3** of this thesis gives a brief overview of wake modelling tools available and sets the context of these studies in relation to the work performed in this project;
- The following **Chapter 4** describes the vortex-ring wake modelling tool which was developed;
- Complementary to the previous chapter, the model developed is verified against different requirements and test cases in **Chapter 5**;
- **Chapter 6** contains the main results and observations and sets out to answer the research questions identified at the outset;
- Conclusions from this work are presented in **Chapter 7** alongside some insights for future suggestions of related work.

Extended derivation details, and additional verification and analyses may be found in the Appendices at the end of this report.

Wind Turbine Wake Stability

This chapter presents different studies, in relation to the stability and meandering tendencies of a wind turbine wake. The first section details the open field, controlled testing and modelling evidence for meandering, as a turbulence-driven phenomenon. Section 2.2 presents similarly structured evidence, from the perspective of intrinsically triggered wake meandering, focusing mainly on the evidence presented in Medici et al. [2]. The chapter is concluded with a review of studies on wake stability, followed by an overview of the presented literature.

2.1 Large scale turbulence as a driver for wake meandering

2.1.1 Controlled scaled experiments

The first title in a series of important publications by España et al. [15, 16, 17], encapsulates the uncertainty surrounding the wake meandering phenomenon

”Is the meandering of a wind turbine wake due to atmospheric length scales?” [15]

The aim of their experimental study was to dissociate the different mechanisms which could possibly contribute to the meandering behaviour of the wake. To achieve this, they performed experiments with the following key features:

1. wind tunnel conditions were such that both Atmospheric Boundary Layer (ABL) and Homogeneous and Isotropic Turbulent (HIT) requirements were satisfied
2. the use of disks of different solidities were employed so as to distinguish rotor induced phenomenon - namely, to pinpoint whether vortex shedding due to flow separation could be a contributing factor.

In their boundary layer wind tunnel, a geometric 1 : 400 scale was configured, allowing for the presence of integral length scales larger than the turbine diameter. This was an essential part for studying large scale eddies on the initiation and progression of a meandering wake.

The use of porous disks to represent the wind turbine rotor avoids intricate aerodynamic detailing which at small scale is particularly difficult to execute. Thus, disk solidity is an important disc parameter to produce similar velocity deficits and thrust coefficients to wind turbines. In this study, solidities less than 45% were used, in order to prevent Eddy detachment, reducing the possibility of vortex shedding [15].

Measurements of the power spectral density and space time correlations essentially pinpoint salient flow signals in the measured wake and their results are summarised below:

- solid-disc wake oscillations were indeed periodic, whereas with porous disks, these were non-periodic;
- the meandering oscillations detected were of a random, chaotic nature;
- in HIT conditions, to examine effects of large scale eddies, the integral length scales were 3-10 times the rotor diameter, and wake oscillations were detected;
- to dissociate between large-eddy driven meandering and flow separation due to vortex shedding, porous and solid disks were used. The observed meandering could not be attributed with vortex shedding phenomena;
- with a porous disk (45%) no periodic meandering phenomena whatsoever were identified.

This study shows the role of large scale eddies in wake meandering, and that, at least using a porous disk approach, no periodic meandering can be observed, in response to the proposition of Medici et al. [2].

2.1.2 Meandering modelling studies

The study of wake meandering has also successfully been tackled numerically, where the main aim of the studies has been to characterise the large scale motion of the entire wake region downstream of a wind turbine rotor. Subsequently, the effective additional turbulence introduced by the meandering of the wake is used to investigate the added loads borne by wind turbine rotors in wake or partial wake operation¹.

The work presented in Larsen et al. [1] covers an extensive theoretical and experimental programme designed for characterising the dynamics of the wind turbine wake and has led to a commonly accepted method for predicting the effective loads of wind turbines operating in wind farms, where the effects of impinging wakes can result in additional loads, fatigue damage and power losses. The most relevant observation in relation to this thesis is that in these studies, the wake was assumed to behave as a passive tracer, convected by the local flow.

¹A wind turbine in wake operation refers to a rotor upon which an upstream wind turbine wake impinges.

2.1.3 Open field validation and observations

A series of field experiments were conducted as part of the Dynamic Wake Meandering project. The basis of the experiments was to verify one of the basic conjectures of the DWM model, that is, that the wake region is transported much like a passive tracer in atmospheric flow driven by large scale turbulent eddies. Their data also tells something about the general development of the far-wake.

An important observation was made by Whale et al. [18] on the results they obtained when comparing field and controlled experimental data. The field models showed better agreement with wind tunnel experiments rather than with open field tests. A number of possible factors were highlighted, one of which was the meandering of the wake. In the presence of this phenomenon, turbine flow fields can be significantly altered, leading to mismatches between the different data sets.

Advances in LiDAR technology have however enabled instantaneous flow measurements, allowing for a better understanding of wake dynamics, and also to serve as a verification for the predictive model, which has in general been successful in predicting the velocity deficits observed [19].

2.2 Intrinsic-instabilities as a driver of wake meandering

2.2.1 Controlled experiments - The KTH experiments

Particular mention must be given to the work carried out by Davide Medici at KTH Mechanics [2].

In contrast to the research documented in Larsen et al. [1], Medici's wind tunnel observations raised doubts over the true understanding of the mechanisms behind wake meandering. They perform wind tunnel experiments where flow velocities were taken at fixed points, downstream of the rotor. A characteristic oscillatory flow pattern was found, an order of magnitude lower than frequencies associated with the passage of tip vortices, reproduced in Figure 2.1. It is proposed by the authors that this could be linked to the observed wake meandering, a mechanism which bears resemblance to the vortex shedding of bluff bodies. An important parameter in this study is the Strouhal number,

$$St = \frac{fD}{U_\infty} \quad (2.1)$$

where the 'meandering frequency' is denoted by f , the free-stream velocity by U_∞ and D the rotor diameter. In their results it was evident that the observed phenomenon only occurs above a certain disc loading, which is why they chose to represent the characteristic frequency using the St number.

They additionally investigated different types of actuator disks and turbine models to ascertain the influence of disk solidity on the observed frequency spectra. The authors state that their experimental data is supported by low frequency peaks reported in field wake measurements in the Alsvik wind farm [20].

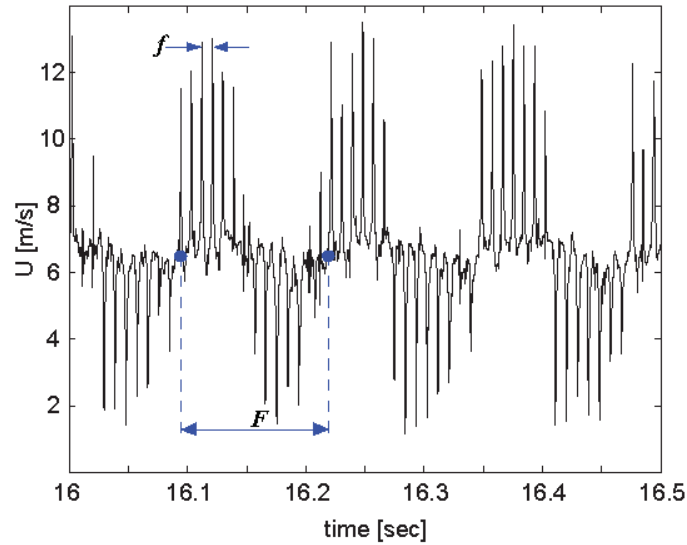


Figure 2.1: Axial velocity signal obtained in the KTH experiments. The low and high frequency peaks (f and F) signify the vortex passage and wake shift respectively [2].

Criticisms

Numerous other authors have pointed out certain issues with the work of Medici et al. [2]. Related to the operating conditions of their model rotor,

- a rather high ratio of the hub-to-rotor frontal area was present
- the thrust coefficient and the ensuing wake velocity deficits were unrealistically high, compared with wind turbines in normal operation mode

At high loads, the rotor presents a higher effective solidity to inflowing air and hence behaves similarly to a solid plate. Due to viscous friction, fluid flow around the edges tends to separate, shedding vortices periodically in the region of the wake surface, similar to bluff body vortex shedding. In addition, the higher load generates higher deficits.

As for the wind tunnel conditions in their experiments,

- the tunnel turbulence produced contained at maximum, integral length scales three times smaller than the model rotor diameter

The contribution of this high frequency component is known to cause wake dispersion. However, the role of large scale eddies (low frequency components), could not have been present in their experimental findings. Given that the latter components are now known to be of considerable significance in the meandering of the wake, the turbulence spectra in their wind tunnel do not describe the complete picture.

Notwithstanding, it could also be argued that the presence of the low frequency components would merely add an additional random oscillatory component to their observed signals. Thus, it is in a sense convenient that these scales were not present since a more lucid picture of the underlying "shedding" is portrayed.

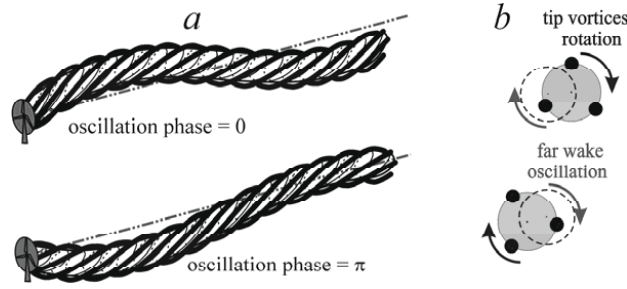


Figure 2.2: Manual offset mechanism for the tuning of an applied wake model (b), motivated as shown in (a). *Source:* Sørensen et al. [5]

2.2.2 Modelling considerations

A follow up study was conducted by Sørensen and Okulov [5] using an analytical helical wake model and a similar velocity signal as found in [2] was obtained. The underlying meandering mechanism is however not fully addressed since the vortex wake model was specifically tuned to obtain a matching velocity signal (see Figure 2.2).

2.3 Wake Stability Studies

2.3.1 Theoretical analyses

A frequently cited publication in relation to understanding the stability of helical vortices is by Widnall [21]. A detailed stability analysis was conducted for an infinite helical vortex filament with a finite core size, excited by small sinusoidal displacements of the helix centreline. The instabilities were categorised as follows:

- a short-wave instability
- a long-wave instability and
- a mutual inductance instability mode

As the helix pitch decreases, the stronger interaction of adjacent filaments was found to cause instabilities in the overall motion of the filament, which is the mutual inductance mode. Self-induced effects were thought to be the cause of the short-wave instability mode. These modes of instability also pertain to vortex rings, and vortex ring arrays. In fact, Levy and Forsdyke [22] conducted a detailed analytical study of an infinite array of vortex rings. The aim of their study was to determine if such an ideal system is stable in response to small disturbances. By expressing the dynamics of the vortex ring array in terms of absolute ring dimensions and location (i.e. ring radii and ring separation) as well as in terms of a small perturbation in the axial and radial position of a ring, they were able to conclude that such a system is always unstable, for all values of ring separation and dimensions.

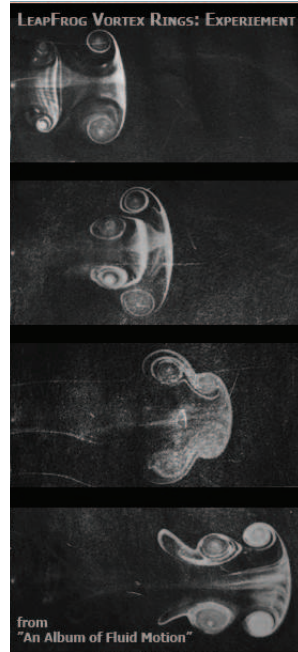


Figure 2.3: Experimental evidence of the leapfrogging behaviour between two coaxial vortex rings. *Source:* An Album of Fluid Motion [6].

Ivanell [23] performed stability studies using a Large Eddy Simulation (LES) of the Navier-Stokes equations. Artificial perturbations introduced upstream caused an out-of-phase interaction between vortex filaments which correspond to the mutual inductance mode, responsible for vortex pairing. The agreement with the results of Felli et al. [7] would seem to indicate the *cause* of the tip vortex instability mode. It is instructive to consider the physical implications of this. Wind turbine blades are of course subject to aeroelastic fluctuations. Larger scale rotors may very well introduce relatively higher perturbations in the flow, which could potentially result in quicker dissipation of the wake.

Okulov and Sørensen [24] conducted an in depth study on the stability of helical rotor wakes where they extend the theory of Joukowsky with regards to the stability of the rotor wake. The model of Joukowsky, for which the wake is represented by B helical tip vortices (B representing the number of turbine blades), was found to be unconditionally unstable. However it was found that the additional contribution of the trailing vortex sheet serves to stabilise the tip vortex system, thus partly explaining that despite Joukowski's implications of an unconditionally unstable wake, stable wind turbine wake are often visualised. The reason behind the stabilisation is due to the mutual interaction of the helical filaments.

2.3.2 Experimental evidence

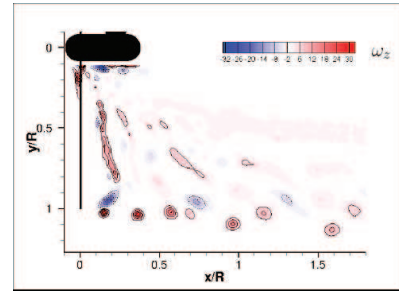
Experimental investigation of the instability modes in rotor wakes is rather limited. Aside from the numerous investigations of near wake rotor aerodynamics, experimental analysis of the transition to far-wake region has been largely limited to the measurement of velocity deficits and turbulence profiles; detailed wake visualisations are therefore somewhat

limited to the near wake regions.

One of the earliest wake visualisations was performed by Alfredsson and Dahlberg [13] at KTH mechanics in the 1970s. The two bladed rotor wake is lucidly shown in Figure 2.4a. The onset of filament interaction can already be spotted at the tip vortex locations after two revolutions, and most notably at the three revolution position where vortex pairing is then evident.



(a) Wind tunnel smoke visualisation showing tip vortex spiral interaction. *Source:* Alfredsson and Dahlberg [13]



(b) Phase averaged wake of a model turbine operating at a higher than optimal tip speed ratio. *Source:* Sherry et al. [25]

Figure 2.4: Visualisation of wind turbine wakes displaying unstable characteristics

Sherry et al. [25] performed experimental measurements on a scaled Tjæreborg rotor in a water channel. In their work, they characterise the evolution of the near wake through visualisations of the wake core cross-section, shown in Figure 2.4b, where they too observe a pairing behaviour between adjacent vortex filaments at a location approximately $1D$ downstream.

Self-induced motion of the curved filament causes deformation of the nearest points, giving rise to a short-wave instability. Successive instances of the helical filament cause a mutual instability mode as their proximity increases. In the recent work of Felli et al. [7], wake visualisations behind marine propellers confirmed these instabilities in remarkable detail for the first time (see for e.g. Figure 2.5). Respective filaments cause a roll-up and 'leap-frogging' process, reminiscent of the leapfrogging phenomenon of parallel vortex rings. The leapfrogging phenomenon of successive helical turns of a wake have also been observed by Stack et al. [14]. In this work, the flow pattern was visualised using fluorescent dye injection².

Felli et al. [12, 7] conclude from a series of detailed wake stability studies the following key characteristics in relation to tip vortex structure breakdown:

- the critical wake transition region shifts further upstream for propellers with a higher number of blades (the authors of this referenced work studied 2-4 bladed propellers)
- the same trend was observed for a given propeller operating at lower advance ratios

²The terms "leapfrogging", "mutual interaction" and "mutual instability mode" are used interchangeably in this thesis and all refer to the periodic interaction, such as shown in Figure 2.3

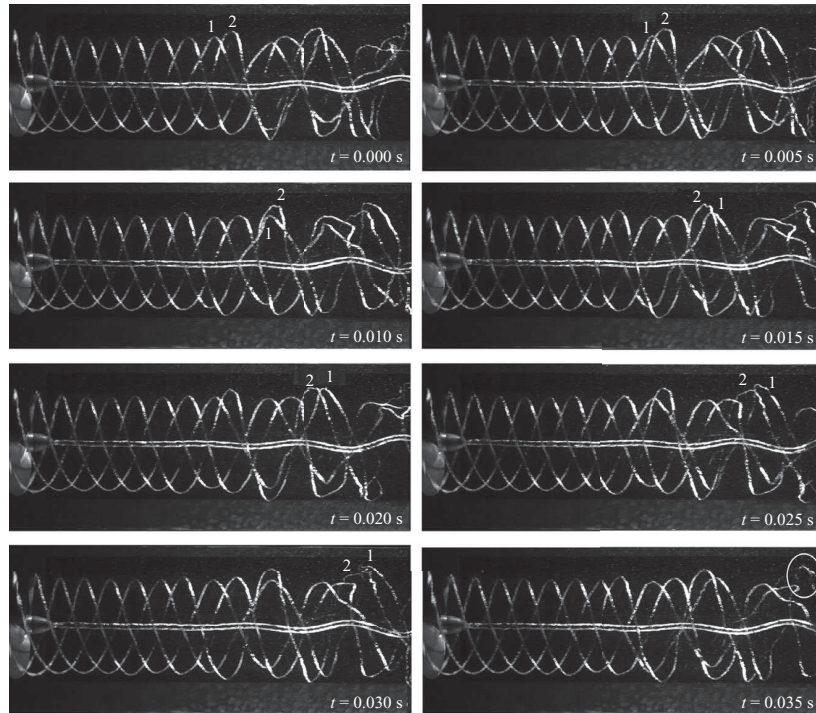


Figure 2.5: Mutual inductance mode between adjacent vortex filaments, observed for a 4-bladed propeller for an advance ratio of 0.65. *Source:* Felli et al. [7]

Similarly for a wind turbine rotor, a higher number of blades means that consecutive wake sheets are relatively closer. This is the case, notwithstanding the fact that rotors with a higher number of blades also operate optimally at lower tip speed ratios. Thus in relation to observations in [7], if such instabilities were to occur within a wind turbine wake, they could be expected to occur at higher tip speed ratios for a given rotor.

2.4 Conclusions

Numerous efforts have been directed in the past few decades towards obtaining a better understanding of the stability of wake aerodynamics. The motivation behind these studies has gradually grown from interest in helicopter and propeller performance, and gradually expanded also to horizontal axis wind turbine rotors.

Vast literature exists on the theoretical modelling and understanding of wake stability regimes. The analysis methods used in each case are rather complex in nature, usually stemming from fundamental mathematical considerations of the pure helical filament. Notwithstanding, these studies have failed to address the understanding of the trigger mechanisms behind wake instabilities. It is evident that the correct modelling of turbulence, viscous effects and vortex breakdown and diffusion pose significant challenges in undertaking such studies computationally. On the other hand, approaching the problem experimentally has yielded useful insights. The shortage of published experimental studies dealing with wake instability mechanisms demonstrates the challenges in setting up the complex testing equipment required for identifying these subtle triggering mechanisms.

Thus the works of Sherry et al. [25] and more so that of Felli et al. [7] are particularly insightful.

The increasing trend in wake studies, in particular the recently published works mentioned in the previous paragraph, are an indication that interest has now also shifted towards acquiring a better understanding of the far-wake, supporting complex theoretical models dealing with far-wake evolution and interaction. This is of course relevant for understanding wind farm performance and dynamics.

Modelling techniques

Rotor and wake modelling techniques are briefly reviewed in this chapter. Vast knowledge has been accumulated over decades of research and experimentation, and thus this chapter will lightly review these methods. Focus is aimed towards simple wake development models and interaction by relatively simple yet insightful means. The first section of this chapter reviews some of the main principles of rotor and wake aerodynamics. The following sections discuss briefly vortex methods, Navier-Stokes models and far-wake models. A particular section is devoted to simple vortex methods using ring models. Some examples of applications to the main modelling criteria described in Chapter 1 are then mentioned in the context of the modelling techniques used.

3.1 Characterising the wake

The flow description of a rotor wake is one of a complex nature. If it were feasible, powerful simulations using full Navier-Stokes codes could provide descriptions of the flow characteristics of single and multiple wind turbine wakes in wind farms. However, in spite the challenges of doing so, it can be argued that the simulation method should also be tailored to the problem of interest using simplified and sometimes, analytical means.

In order to do so effectively, assumptions and simplifications need to be devised carefully. One such simplification in models follows through the identification of the near- and far-wake regions. No strict definition exists as to where the near-wake ends, and the far-wake commences and in fact, a transition region exists. The near-wake is that region, typically within two diameters downstream of the rotor, where the effect of the blades and persistence of tip vortex structures is still a defining feature of the flow.

In the far-wake region, the wake is fully developed and the shear at the wake boundary is less prevalent. Thus in modelling the near-wake, a good description of the rotor geometry is essential, whilst this is not the case for the far-wake region.

3.2 Vortex Methods

A recent in-depth review is presented by Stock [26] and the sheer number of methods discussed here is testament to the wide spread take up of this technique by many an engineering discipline. These methods are suited to the description of rotor and wake aerodynamics, offering a compromise between CFD and simpler more common methods such as BEM.

Vortex models describe the transport of vorticity, which is subsequently used to describe the flow field using Biot-Savart integration. In the near wake, the structure is determined primarily by the distribution of the blade bound vorticity. For most purposes, evaluating this distribution is the primary objective for evaluating the new wake induced velocities, as done in most vortex method procedures, using the Kutta-Joukowski theorem:

$$\mathbf{L} = \rho \mathbf{\Gamma} \times \mathbf{U}_{rel} \quad (3.1)$$

The statement that the circulation that is bounded by the blade is trailed into the wake, is captured in Helmholtz's theorem, which essentially states that a vortex tube cannot start or end in a fluid [27]. For both viscous and inviscid flow, the tip and root vortices have a different sense of strength. Actually, the continual strength variation along the blade tends to trail vortices all along the blade, the sense of which depends on the gradient of the distribution. The steepest gradients exist near the extremities, which give rise to the strong concentration of tip and root vortices. The tip vortex is normally the dominant part since the distribution gradient is normally higher in this region. The continuous trailing and shedding of vortices thus creates a vortex sheet, with a strong concentration at the inner and outer edges (corresponding to the blade extremities).

In potential flow theory, where vorticity is lumped to represent lifting surfaces, the underlying assumption is that the vortex core accounts fully for the presence of vorticity, whilst treating the outer flow as completely inviscid. The simplified incompressible Navier-Stokes equations in inviscid flow can therefore be used to solve for the velocity field at any point in the domain.

Vortex models manifest most simply as *lifting line models*, where vorticity is lumped into a single line, representing the lifting surface. This was proposed originally by Prandtl and is rather useful for evaluating near wake regions. An extension of lifting line models using straight line vortex filaments, is the curved *vortex filament*. The concept being that the curvature of the helical rotor wake is represented more accurately, allowing more reasonable discretisations, but most importantly, a reduction of singular behaviour close to the location of the curved vortex filament. Some example efforts from literature include the works of van Hoydonck [28] and Xu et al. [29], where the development of the curved arc vortex filaments are explored for use with analyses of helicopter rotor wakes.

Attaining a higher level of detail, *panel methods* represent the blade as a lifting surface more closely by imposing panel solutions of constant strength over the surface. This results in a much better flow resolution over the lifting surfaces and hence makes for a handy tool for assessing in more blade design.

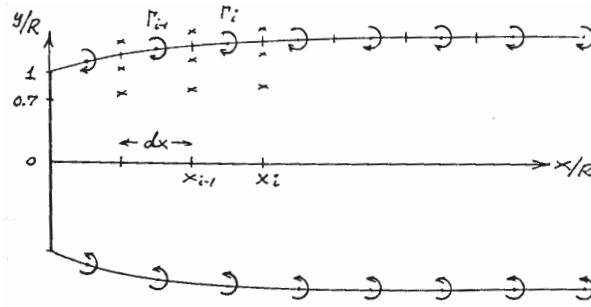


Figure 3.1: Simplified rotor wake representation using discrete vortex rings and flow conservation. *Source:* Øye [8].

3.2.1 Vortex ring representations

Øye [8] developed a simple vortex wake model by considering a uniformly loaded actuator surface and an ensuing expanded vortex wake, consisting of only tangential (azimuthal) surface vorticity, illustrated in Figure 3.1. This was done using an array of discrete vortex rings and by considerations of mass continuity to model wake expansion, enabling the author to conjure up straight forward corrections for BEM predictions, based on the derived relations between the rotor thrust coefficient and the calculated induced velocities. The simplified yet physically consistent model yielded appreciable results and was certainly a useful contribution to estimated load and induction predictions derived from the BEM method.

Similarly using analytical expressions of vortex rings to model flow conditions, Stubblefield [30] describes the improvement of a commercial propeller analysis tool, *OpenProp*, through the use of vortex rings, which are used to represent the influence of the ducted intake for the propellers. Widnall also describes the surface vorticity contribution of ducts in potential flow calculation for ducted wind turbines [31].

The application of ideal vortex rings to model actuator wakes is not a novel one. However, most examples found in literature actually use a surface or tube of vorticity, which can be thought of as a continuous distribution of vortex rings. Wake expansion (or contraction, depending on the operational state of the rotor) is normally neglected.

Micallef et al. [32] described a simplified method using an array of equispaced, tilted vortex rings to provide an estimate for the wake skew angle due to shear flow. In this work, the vortex rings are treated as a collapsed single helical turn of a wind turbine wake, at locations determined by the pitch. Using the analytical expression for the velocity induced by ideal vortex rings, the wake is prescribed downstream of the rotor. The results for the wake skew angle were in appreciable agreement with results from a dedicated panel code.

In this simplest of vortex ring models, the vortex rings considered are ideal, preserving axisymmetric flow in local ring coordinates. The shape of the vortex core is assumed to be circular with a cross-sectional diameter much smaller than the ring major radius, with a uniform distribution of vorticity throughout the core.

3.3 Navier-Stokes models

A recent comprehensive review is presented in Sanderse et al. [33] on the use of CFD codes for wind turbine calculations. The computational techniques are easily identified according to the method of turbulence modelling employed, which is of particular importance with the modelling of wind turbine wakes. The large Reynolds number characterising the flow field concerned is large, which means that a wide range of turbulent scales must be resolved in order to fully solve the complete Navier-Stokes equations. This may be done through Direct Numerical Simulation (DNS). However resolving the range of scales is extremely computationally expensive. Thus wake and rotor simplifications are employed, as well as additional turbulence models in order to estimate the effect of unresolved turbulent scales on the flow.

Reynolds Averaged Navier-Stokes (RANS) and Large Eddy Simulation (LES) are most often encountered in wind turbine wake modelling. In RANS modelling, an elegant yet widely accepted solution to solving the complete set of Navier-Stokes equations is adopted. The flow is broken down into a mean flow with an overlaid fluctuating turbulent component. This manifests as the Reynolds stress. An integral component of RANS modelling is the choice of the physical model according to which the turbulent components are approximated.

LES finds its way between RANS and DNS. It is superior to RANS models in that it does away with the dependence on turbulence models. Large turbulent scales are explicitly computed and only the smaller scales are modelled. This method is gaining popularity in wind turbine simulations and wind farm modelling since it is possible to directly estimate wind velocity deficits and additional turbulence intensities. Lu et al. [34] present an LES simulation of a large wind farm, coupled with an actuator line technique, in a stable boundary layer. The authors investigate the effect of boundary layer stability and wind farm layout on wake interaction inside the wind farm and draw insights regarding the effects of wind farms on local meteorology, as well as the extent of wake interaction and dissipation inside the wind farm.

3.4 Far wake models

Some of the better known far-wake descriptor models include the model of Jensen, Larsen and Frandsen. These are *kinematic models* which are coupled with separate turbulence models in order to evaluate wind speed deficits for wind turbines in wind farm configurations. The former model, one of the older models available, produces a typical top-hat velocity deficit by assuming a linear increase in the deficit velocity in the wake of a wind turbine. Other kinematic models aim to improve the description of the velocity deficits in the wake using better physical representations of rotor aerodynamics and the atmospheric boundary layer.

Field models incorporate the well known Ainslie model as well as commercial programmes Wakefarm by ECN [35]. The former is based on a simple two dimensional representation of the turbulent momentum equations, neglecting pressure gradients in the far-wake. A more complex 3D representation of the RANS equations governs the working of the Wakefarm model by ECN using the common $\kappa - \epsilon$ model to provide closure.

Other models aim to combine the strength of the kinematic and field models, however with the main aim of characterising velocity deficits in the far-wake regions.

3.5 Applications

In light of the methods described in this section, it is useful to now consider the techniques which have been adopted for studying particular external effects on wake modelling, which are of course pertinent to this thesis.

Two notable studies which deal particularly with the influence of the ground are efforts by ECN [9], as well as a detailed study performed by Madsen et al. [10]. It must be mentioned at this point that in fact, these studies also investigate effects of wind shear. Sample wake plots from these works are shown in Figures 3.2 and 3.3.

In ECN's AWSM model [9], which is based on Prandtl's lifting line theory, the ground was virtually taken into account by mirroring each influencing point on the lifting lines. More specifically, the location of each mirrored point was opposite to the original one compared with the location of the ground, and the circulation was also inverted in sign. This is done simply by adding the Biot-Savart velocity contribution from the virtual wake elements. This, by definition, satisfies the non-entry boundary condition at the ground plane.

Madsen et al. [10] focused mainly on providing estimates for the differences in power output for turbines in both these operating regimes, and also compared estimates from different numerical codes, however the comparison was rather inconclusive as to the effects of combined shear and ground on the power production of the turbine.

Grasso [9] observed stronger interaction in the lower portion of the wake due to the relative higher contribution from the ground effect. Thus respective tip vortex filaments are seen to tilt, relative to their equilibrium position.

Studies related to yawed and sheared flow have been studied in greater detail. Various techniques have been applied to characterising these complex flow regimes. An interesting recent publication by Jimenez et al. [36] conducted an LES investigation of wind turbine operation in yawed flow, where these authors also aimed to develop simple engineering models to describe the effects of yaw. This example also illustrates that engineering models using simple physical models are gaining popularity.

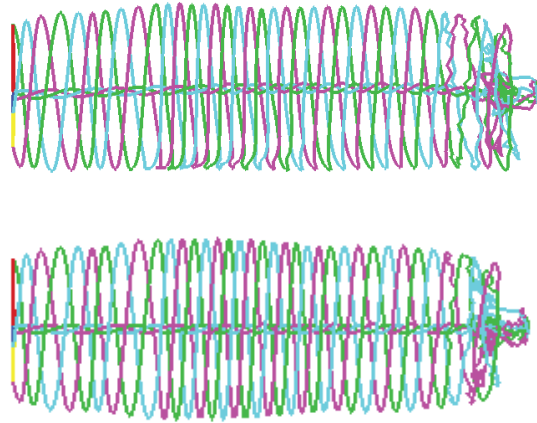


Figure 3.2: Wake in ground effect (top) and outside of ground effect (bottom). *Source:* Grasso [9].

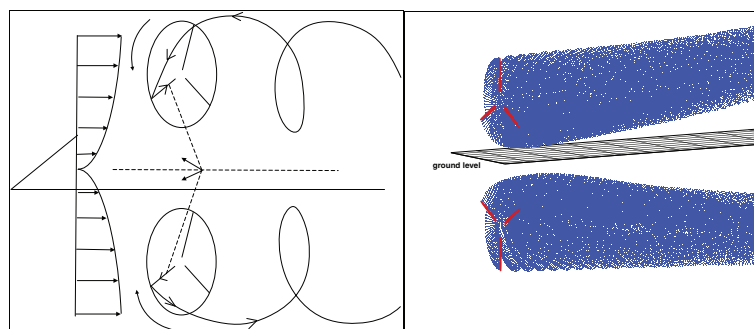


Figure 3.3: Wake in ground effect modelling method. *Source:* Madsen et al. [10].

Development of a Free-Wake Vortex Ring Model

This chapter documents the development and implementation of a HAWT wake model for the investigation of stability behaviour. Having outlined the different options available for modelling the wake in the parametric and simplified fashion desired, applicable theory and assumptions are further highlighted here in section 4.1. The use of the vortex ring and some characteristic velocity field plots are described in section 4.2. The HAWT wake model is then presented in section 4.3, with a treatment of the main modelling consideration. The interaction of vortex rings as an isolated study is briefly described in section 4.4 and finally, simulation procedures are outlined in section 4.5.

4.1 Model Conceptualisation

As described in Chapter 3, there are numerous approaches to modelling the wake of a wind turbine. Key to developing any model reflecting physical phenomena are well devised assumptions and simplifications. These will be outlined briefly in this section, backed by the relevant theoretical considerations.

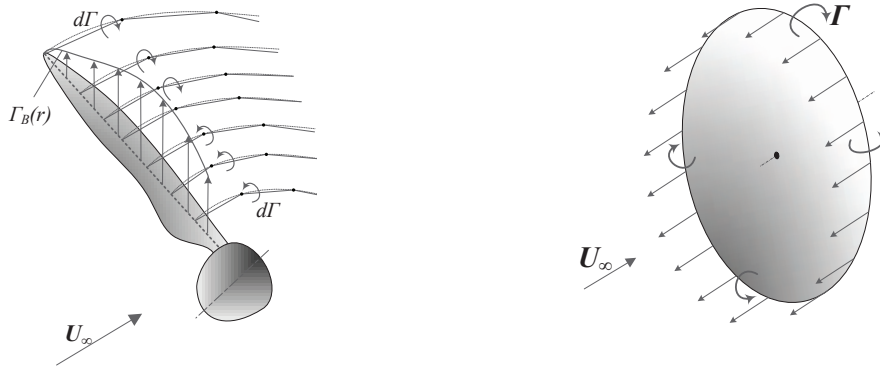
4.1.1 Underlying assumptions and simplifications

The implemented wake model is required to predict the general development of the wake. The detailed interactions of prescribed vortex ring systems is a further necessity in order to identify key parameters governing the nature of the interactions. To investigate the role these vortex filament interactions have on wake stability, it is furthermore desired to incorporate these two types of simulations into a more detailed wake model.

The models are therefore built around the following set of assumptions and simplifications:

1. The simulated rotor wind turbine will be treated as an actuator disk with uniform loading. This means that only azimuthal vorticity γ_θ is generated at the tips or edges of the actuator disk.
2. The wake surface will be modelled discretely using tip vortex rings. Therefore the absence of the root vortex in this model implies that wake rotation is neglected for this study of wake dynamics.
3. The vortex ring elements considered are ideal vortex rings, and are treated as rigidly expanding bodies which rotate about their centroid in response to the applied flow field

4.1.2 Overview of the modelling approach



(a) Lifting line representation of a rotor blade and trailing vorticity (b) Uniformly loaded actuator disk (loaded shown at the periphery only for clarify)

Figure 4.1: Wind turbine rotor representation

The choice of modelling the wake using vortex rings contrasts with more common and detailed rotor/wake representations; for instance, the lifting line representation of an individual rotor blade. In the latter case, depicted in Figure 4.1a, a helical wake consisting trailing and shed vorticity would result, and is commonly approximated using straight vortex line segments. This is shown schematically in Figure 4.2a. This approach will be partially based on the works of Øye [8] and Micallef et al. [32].

On the other hand, with a vortex ring approach, the resulting wake is modelled according to the actuator disk representation of Figure 4.1b. This contains only an azimuthal vorticity component and gives rise to axial and radial velocities. This wake representation is similar to that described by Øye in section 3.2.1 and is illustrated in Figure 4.2b.

The advantage for this study of using vortex rings in this way is that, in contrast to the more complex numerical methods available, the rotor wake can be represented in a simple but physically consistent manner whilst allowing, to a reasonable extent, analytic parametric investigations of the effects of destabilising a vortex ring system and these implications on rotor wake development and stability.

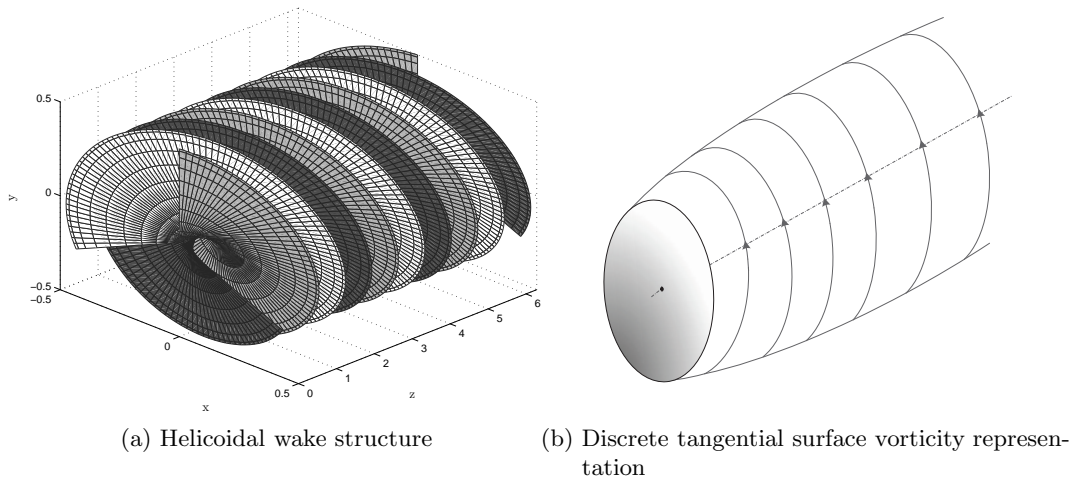


Figure 4.2: Wake representation due to different rotor models

4.2 The ideal vortex ring

For this study, the vortex rings are considered as ideal fluid elements with favourable properties and mathematical attributes, suited to modelling the wake of a wind turbine rotor. Thus, in a sense, a vortex ring in this context does not represent a real, physical vortex ring which may have an arbitrary core vorticity distribution.

From considerations of axisymmetric, inviscid and incompressible flow, we arrive at the important relations for these ideal vortex rings. These useful relations are often given in terms of the streamfunction, as well as the induced velocity field. For a more detailed treatment of the fundamental governing equations, the reader is referred to Appendix A. In mathematical terms, the assumptions and simplifications implied in the derivation of the analytical equations are outlined below in terms salient important vortex ring and flow characteristics:

- **Thin** In the limit as the vortex core tends to an infinitely small size, the rings can be considered thin, with a uniform core vorticity distribution
- **Axisymmetric** In order to simplify the analysis, the vortex rings are considered perfectly circular in shape, enabling a straightforward integration of the influence of the contributing elements around the perimeter of the ring. Thus the vortex ring profile may expand and/or contract, but will always maintain a circular periphery
- **Uniform** A further simplification is to consider a uniform strength distribution around the perimeter of the rings. This is to say that when integrating the contribution of each elemental filament, the strength is an independent parameter which may be removed from the integral, simplifying the analysis further
- **Inviscid** The effects of viscosity on the evolution of the core are neglected in line with the assumption of a *thin* ring

- **Incompressible** The flow field is considered incompressible, such that the fluid density is invariable.

The analysis yields simple analytical expressions for the induced velocity from ideal vortex rings, in terms of elliptic integrals. The reference frame for the following equations is shown in Figure 4.4. The inducing ring is centered at $C(x_i, y_i, z_i)$, and in this illustration, we are interested in the velocity induced on the periphery at $p(x, y, z)$ of another vortex ring. Note also that a positive vortex ring strength, in line with the local and global coordinate systems is defined in such a way that the resulting axial induced velocity is in the positive sense. Thus a positive Γ_θ leads to a positive axial induced velocity u_z . This is illustrated in Figure 4.3.

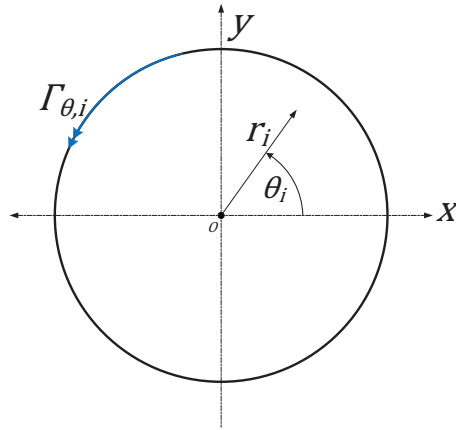


Figure 4.3: Positive convention for the assigned ring strength Γ_i

The axial and radial induced velocities from the i^{th} vortex ring, at an arbitrary point p in 3D space are given by the following:

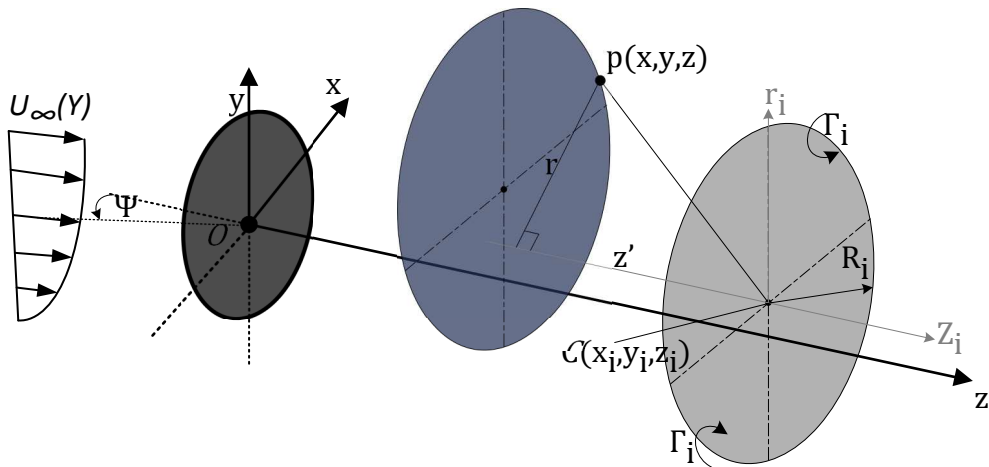


Figure 4.4: Global and local coordinate system definitions

$$u_z = \frac{\Gamma_i}{2\pi\sqrt{[(z - z_i)^2 + (r + R)^2]}} \cdot \left[K(m) + \frac{R_i^2 - r^2 - (z - z_i)^2}{(z - z_i)^2 + (R_i - r)^2} E(m) \right] \quad (4.1)$$

$$u_r = \frac{\Gamma_i(z - z_i)}{2\pi r\sqrt{[(z - z_i)^2 + (r + R_i)^2]}} \cdot \left[K(m) - \frac{R_i^2 + r^2 + (z - z_i)^2}{(z - z_i)^2 + (R_i - r)^2} E(m) \right] \quad (4.2)$$

where $K(m)$ and $E(m)$ are elliptic type integrals of the first and second kind, expressed in terms of the parameter m . Note that in these equations, since Γ_θ is the only circulation component describing the flow field, the symbol Γ will be used in simplification. As indicated in the schematic, r represents the normal radial distance from the point in consideration to the axis of the inducing ring. Thus it is clear from these equations that the important geometric quantities are the relative distance to the ring axis r and the relative axial separation, z' .

The parameter m is given by

$$m = \frac{4rR_i}{[(z - z_i)^2 + (r + R_i)^2]} \quad (4.3)$$

Evaluation of these integrals has been treated in great depth in literature, with many authors exploring different approaches for the solution of the integrals. The method of geometric means of Abramowitz et al. [37] is considered by far the superior approach for evaluating the first and second kind integrals. This method is conveniently readily available in the Matlab function `ellipke`.

An inclined vortex ring

Since we are interested in modelling the effect of non-uniformities such as shear and yawed flow (as illustrated in Figure 4.4), it can be expected that the overall resultant of the induced velocity acting on a vortex ring will result in its displacement, but will also affect its orientation. Thus it is required to predict the induced velocities from inclined vortex rings. This means that for each evaluation point, we require the effective radial distance from the inducing ring centreline axis r and the axial separation from the inducing ring plane, z' .

In order to maintain the analysis in terms of these two geometric quantities, the equivalent point method as first described in Micallef et al. [32] is adopted here, and extended to vortex rings with both *skew* as well as *tilt*. Skew (β) is defined here as the rotation of a vortex ring about the y -axis, whilst rotation about the x -axis is denoted as tilting (χ). This convention is shown in Figure 4.5. The derived expressions for the effective radial and axial separation for the case of an inclined vortex ring are then used directly in equations 4.1 and 4.2. More information about the derivation of these extended equations may be found in Appendix B.

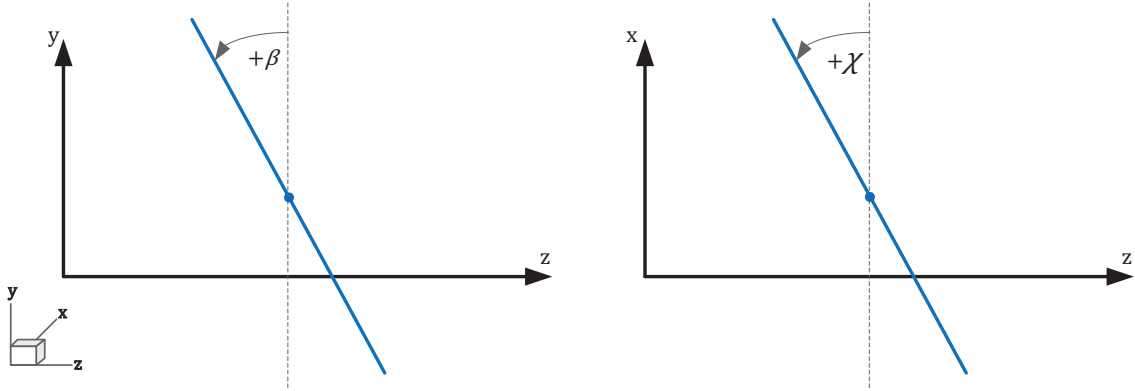


Figure 4.5: Coordinate System and angular definitions

Table 4.1: Salient quantities evaluated from the analytical ideal vortex ring equations in local vortex ring coordinates

Case	Coordinates (r_i, z_i)	u_r	u_z
(i)	$(r, 0)$	0	$\neq 0$
(ii)	$(R, 0)$	∞	∞
(iii)	$(0, z)$	0	$\neq 0$
(iv)	$(0, 0)$	0	$\Gamma/2R$

4.2.1 Induced velocity field

The velocities resulting from the ideal vortex rings are illustrated in Figures 4.6 and 4.7. Further visualisations are presented in Appendix A and E.

As seen in these plots, the analytical equations show asymptotic behaviour for certain regions. Additionally, when the evaluation coordinates approach the periphery of the inducing ring, singular behaviour is observed. Salient values are tabulated Table 4.1 for these regions of interest.

If the evaluation point coincides with a point on the ring itself such as in Case (ii), the solution is undefined. However, realistically speaking, the velocity at $(R, 0)$ would correspond to the centre of the vortex core, where the velocity due to the ring itself is null. Thus should this case arise, it is handled separately and corrected. Case (i) shows that in the plane of the ring, the radial induced velocity is zero everywhere, whereas the axial velocity is finite and maximum at the ring centroid, as shown in Case (iv). The radial velocity is also null along the axis of the vortex ring since the radial components from each infinitesimal ring segment cancel out. The axial velocity induced at the centroid corresponds to the self-induced motion of the vortex ring which occurs due to the influence of each segment of the ring on other segments. This self-induced characteristic is in general observed whenever vortex filament has some finite curvature. The self-induced component is an important feature of the ideal vortex rings which must be accounted for explicitly in the model. The latter is addressed in some more detail in section 4.3.4.

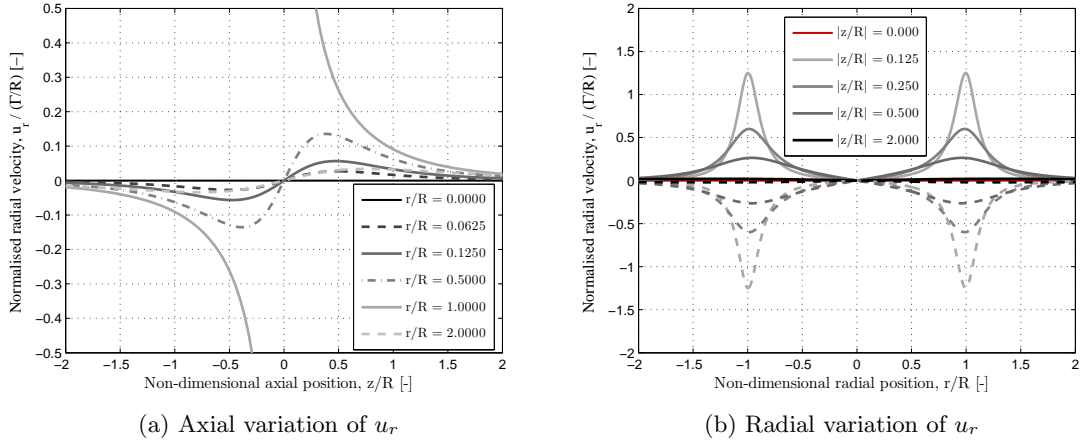


Figure 4.6: Variation of the radial velocity of an ideal vortex ring

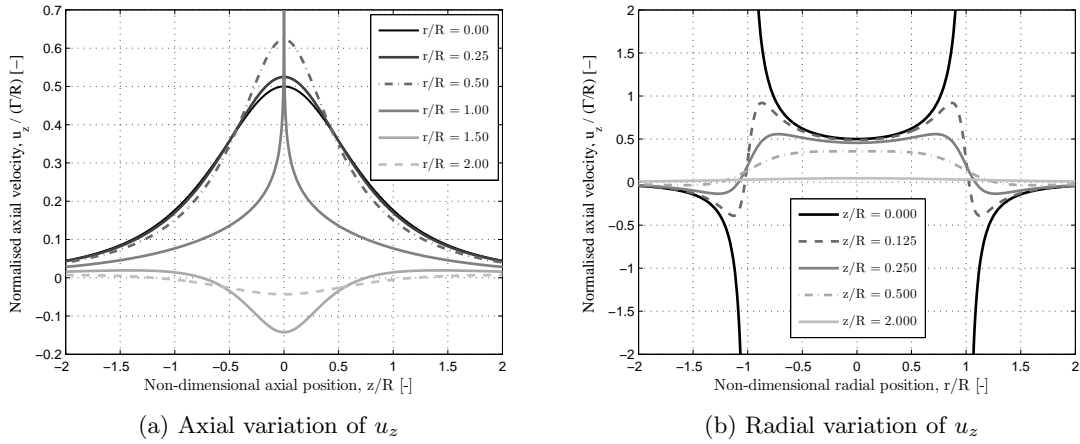


Figure 4.7: Variation of the radial velocity of an ideal vortex ring

4.3 Analytical HAWT wake model

It is of interest to identify the effect of perturbations on the development of the wake using the simple model developed. The procedure initiates with a tip ring being shed after a time step ΔT , set for instance according to a typical tip speed ratio $\lambda = 5$ for an $R = 50m$ rotor, at a wind speed of $10m/s$. The first ring is shed at a spatial location behind the rotor based on the total velocity at the rotor plane at $t = 0$.

The wake vortex rings are treated as rigidly expanding bodies so as to incorporate wake expansion as well as to allow for the inclusion of turning effects on the rings. The general procedure for the development of the wake is as follows

- Evaluate induced velocity components at the vortex ring peripheries, arising due to self and mutually induced effects, and optionally, due to ground proximity effects.

- Average the induced velocities at the periphery of each ring
- Estimate the turning effects of each successive ring caused by any resultant velocities due to perturbations
- Update the new ring positions and orientations, based on the average induced velocities and/or any tilting or skewing effects present

The orientation then must be evaluated in response to the average flow field acting upon the ring. Subsequently, within the wake, each ring's position is updated by evaluating the total velocities and moments on the periphery of the ring and using a forward Euler scheme to estimate the new ring positions and orientations.

Viscous effects are intentionally excluded from the model such that, unless prescribed otherwise, the strength of the vortex rings is fixed and invariable throughout a simulation.

4.3.1 Evaluating the induced velocities

For a full free wake simulation, velocities must be evaluated at wake nodes (i.e. on wake vortex rings) as well as at the actuator surface.

At the actuator disk, the velocities across the whole plane are required. The disk is thus discretised into radial and azimuthal segments as shown in Figure 4.8b. Note that for practical modelling purposes, with reference to Figure 4.4, the rotor plane is located in the xy plane and centered at the origin O . Thus the rotor axis is aligned with the z axis.

The vortex ring elements representing the wake induce velocities on other rings. To evaluate the motion of the wake due to the induced motion on itself, velocities are therefore evaluated at locations on the perimeter of the rings, discretised as shown in Figure 4.8a.

With reference to Figure 4.8, steps of $\frac{2\pi}{d\theta} = 41$ and $\frac{R}{dr} = 21$ offer a good compromise between computation time, and averaging accuracy. For coaxial vortex rings interacting in ideal conditions (no perturbations and in uniform flow), one single evaluation point on the periphery of a ring is sufficient to predict the system dynamics due to flow axisymmetry. However, as soon as the vortex rings become off-centered, it is required to average the induced velocities on the ring periphery. The discretisation levels specified were found to provide a good estimation of this average as further refinement did not yield significantly different averaged quantities.

4.3.2 Averaging the induced velocities

In more detailed representations of the rotor, the resulting helicoidal wake may for instance be described using straight vortex filaments, as shown in Figure 4.2a. The wake nodes as seen in this diagram represent the evaluation points of the wake and after each time step, node positions are updated according to their instantaneous velocities.

With a ring model of the wake, where a single vortex ring represents one helical turn, a ring must maintain its ideal circular shape and must therefore be shifted in its entirety. This of course means that the development of the wake will be limited to the rigid motion of the vortex ring centroid, as well as ring expansion and/or contraction.

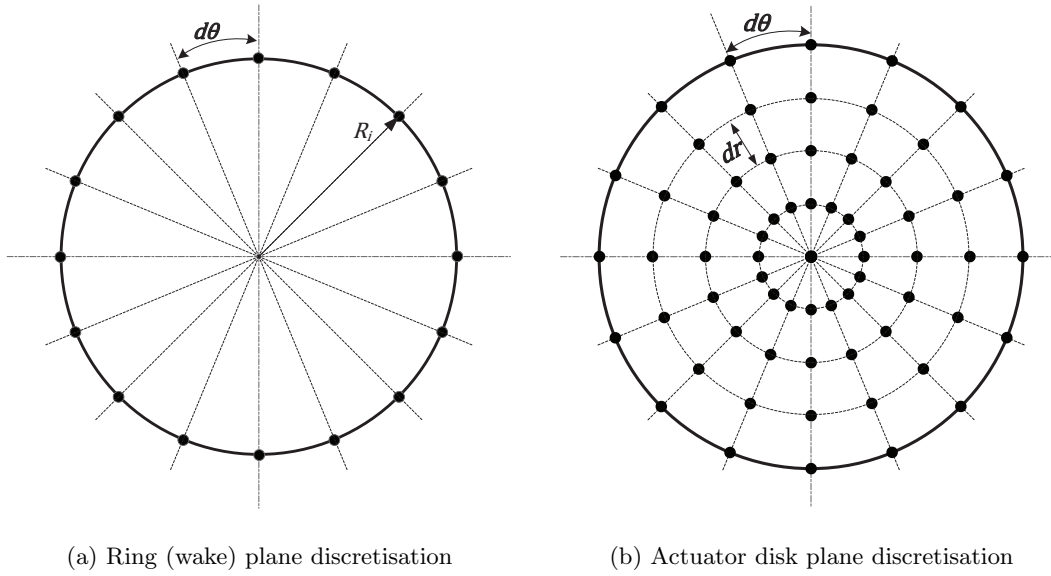


Figure 4.8: Element discretisation for velocity evaluation

Thus, having evaluated the velocities on the periphery of a ring, an averaging procedure must be applied, so as to transport the wake rings according to this averaged quantity. For the i^{th} vortex ring in consideration,

$$\bar{\mathbf{u}}_i = (\bar{u}_x, \bar{u}_y, \bar{u}_z) = \frac{1}{2\pi} \int_{\varrho}^{R_i} \int_0^{2\pi} \mathbf{u}_i(r_i, \theta_i) d\theta_i dr_i \quad (4.4)$$

where the $\bar{\mathbf{u}}$ is the averaged total velocity field acting at the ring and $\mathbf{u}_i(r_i, \theta_i)$ is the vector containing all resolved velocities at each location on the ring. The lower radial integral limit ϱ takes on the value of 0 for the situation at the rotor plane, and R_i if the velocities are being evaluated at the rotor plane.

Combining this with the transformation matrices defined in the previous section, it is possible to express the average velocities in terms of local ring coordinates, which is required if the radial expansion/contraction due to mutual induced velocities is required.

4.3.3 Modelling flow instabilities

An integral part of this model is to enable the modelling of non-uniform inflow effects, as well as the presence of the ground on the development and stability of the wake. The effects of shear and yawed flow on rotor and wake aerodynamics have been heavily investigated, whereas the effect of the ground on wake development has received much less attention. These non-uniformities are therefore implemented in this model and explained in the following sections.

Shear and yawed flow

The influence of a sheared inflow is examined by defining a simple power-law relation for the freestream wind speed $U_\infty(Y)$ with the height above ground level Y ,

$$U_\infty(Y) = U_\infty(HH) \cdot \left(\frac{Y}{HH}\right)^m \quad (4.5)$$

where the wind velocity at an arbitrary height Y is defined in terms of the hub height wind velocity U_{HH} and the shear exponent m . Note that since the rotor is centered at the origin, $Y = y + HH$ for an arbitrary vertical position y ¹.

The ability to handle yawed inflow is also desired and is simply implemented using the generalised equations described thus far in this chapter. The angle lying in the yz plane, subtending the freestream wind vector and the rotor axis (the z axis) is denoted as the yaw angle, Ψ . The presence of yaw introduces instabilities which results in a loss of wake symmetry about the yz plane.

The total freestream velocity field can be generalised to include yawed inflow and a sheared vertical velocity profile,

$$\mathbf{U}_\infty(Y) = \begin{bmatrix} U_{x,\infty} \\ U_{y,\infty} \\ U_{z,\infty} \end{bmatrix} = \begin{bmatrix} U_\infty(Y)\sin(\Psi) \\ 0 \\ U_\infty(Y)\cos(\Psi) \end{bmatrix} \quad (4.6)$$

Ground Effect Modelling

In aircraft aerodynamics, it has long been observed that in the proximity of the ground, the performance of the aircraft is altered. Downwash is reduced, which has the beneficial impact of reducing induced drag, and within one wingspan from the ground, an air cushion effect is also experienced. In wind tunnel testing, this phenomenon was commonly simulated by using a duplicate of the model, mirrored about the ground plane. This imposes the correct zero-flow conditions at the ground plane.

In order to simulate the presence of the ground in this model, a similar mirroring approach is used. The concept is that the induced velocity at all points above ground level will be affected by additional contribution due to the presence of the ground; the ground is virtually taken into account by adding a reflected version of the wake about the ground plane. The sense of strength of the mirrored wake rings must be such that the zero-flow condition at the boundary plane is satisfied. This is illustrated in the schematic of Figure 4.9

An important parameter which will be specifically investigated is the hub height. In the absence of ground effect and wind shear, this parameter is not particularly relevant to the modelling of rotor and wake aerodynamics. In the presence of the ground however, this will clearly be an important parameter characterising the development of the wake in ground effect.

¹The exponent m depends amongst other things on the stability of the atmospheric boundary layer and the terrain roughness. An exponent of $m = 0.2$ is typically used in design practice.

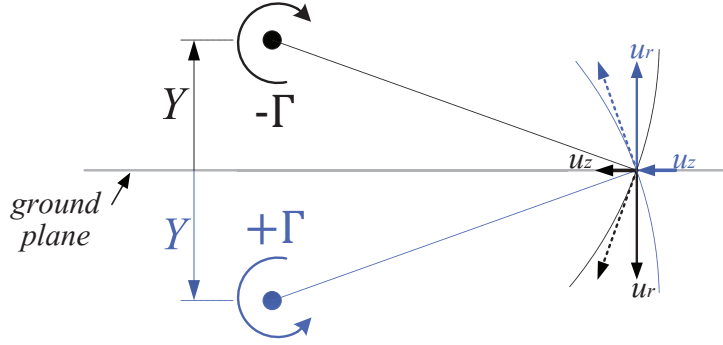


Figure 4.9: Principle of zero-boundary flow underlying the ground effect model

The implementation of the ground effect simply follows from the previous analysis on vortex ring. The induced velocities from the mirrored wake rings at location above ground level are calculated, taking into account the additional vertical separation and the reflecting ring orientations, as shown in Figure 4.10.

Implementation

The non-uniform conditions addressed in this section thus far, if present in a given simulation, would give rise to overall resultant velocities causing off-axis motion as well as ring rotation due to the effective turning moments. Estimating these turning effects are an important component of the model.

A simple method to estimate the average turning effects due to some resultant average velocities along the ring periphery, is based on the simple kinematic relation for the rotational frequency of a solid body. To find the turning moment about the x and y axis, the procedure is applied twice in succession, obtaining an updated value for the ring orientations β and χ .

For a solid body, the rotational frequency $\Omega = \frac{u_{tan}}{d_{eff}}$, where u_{tan} is the tangential velocity which is normal to d_{eff} , which is the effective moment arm. It is first required to estimate the average velocities in the upper and lower semicircular portions of the vortex ring. These average velocities are given as follows for estimating the rotation about the x axis:

$$\bar{u}_{\perp 0, \pi} = \frac{1}{\pi} \int_{\varrho}^{R_i} \int_0^{\pi} u_{\perp}(r_i, \theta_i) d\theta_i dr \quad \text{and} \quad \bar{u}_{\perp \pi, 2\pi} = \frac{1}{\pi} \int_{\varrho}^{R_i} \int_{\pi}^{2\pi} u_{\perp}(r_i, \theta_i) d\theta dr \quad (4.7)$$

$$\bar{\Omega}_{0, \pi} = \frac{1}{\pi} \int_{\varrho}^R \int_0^{\pi} \Omega(r_i, \theta_i) d\theta dr \quad \text{and} \quad \bar{\Omega}_{\pi, 2\pi} = \frac{1}{\pi} \int_{\varrho}^R \int_{\pi}^{2\pi} \Omega(r_i, \theta_i) d\theta dr \quad (4.8)$$

The notation $(\perp 0, \pi)$ and $(\perp \pi, 2\pi)$ is used to denote a quantity averaged over that

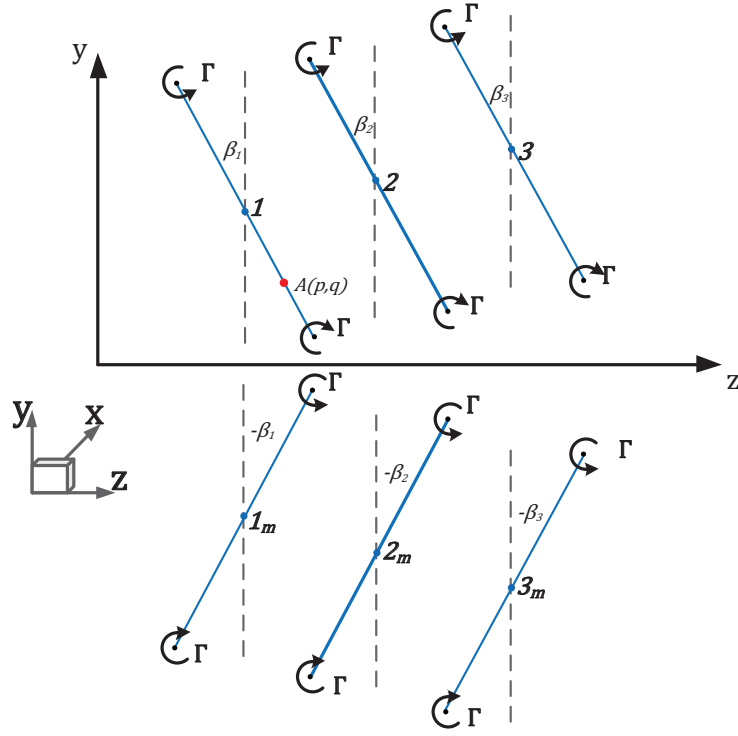


Figure 4.10: Ground effect modelling with ideal vortex rings

respective domain. Therefore, $\bar{u}_{\perp\pi,2\pi}$ indicates the normal averaged velocity over the domain $0, \pi$. Thus, these equations enable one to find the effective moment arm,

$$d_{eff}^{tilt} = d_{0,\pi} + d_{\pi,2\pi} \quad (4.9)$$

where,

$$d_{0,\pi} = \frac{\bar{u}_{\perp 0,\pi}}{\bar{\Omega}_{0,\pi}} \quad \text{and} \quad d_{\pi,2\pi} = \frac{\bar{u}_{\perp \pi,2\pi}}{\bar{\Omega}_{\pi,2\pi}} \quad (4.10)$$

A similar approach is followed for evaluating the skewing of the vortex rings (rotation about the y -axis). In this case, the angular limits of integration in equations 4.11 and 4.12 are shifted by $-\pi/2$. The resulting averaging and rotational effects will manifest as follows,

$$\bar{u}_{\perp -\pi/2, +\pi/2} = \frac{1}{\pi} \int_0^R \int_{-\pi/2}^{+\pi/2} \mathbf{u}_{\perp}(r, \theta) d\theta dr \quad \text{and} \quad \bar{u}_{\perp +\pi/2, +3\pi/2} = \frac{1}{\pi} \int_0^R \int_{+\pi/2}^{+3\pi/2} \mathbf{u}_{\perp}(r, \theta) d\theta dr \quad (4.11)$$

$$\bar{\Omega}_{-\pi/2, +\pi/2} = \frac{1}{\pi} \int_0^R \int_{-\pi/2}^{+\pi/2} \Omega(r, \theta) d\theta dr \quad \text{and} \quad \bar{\Omega}_{+\pi/2, +3\pi/2} = \frac{1}{\pi} \int_0^R \int_{+\pi/2}^{+3\pi/2} \Omega(r, \theta) d\theta dr \quad (4.12)$$

Similarly, for the moment arm

$$d_{eff}^{skew} = d_{-\pi/2,+\pi/2} + d_{+\pi/2,+3\pi/2} \quad (4.13)$$

where,

$$d_{-\pi/2,+\pi/2} = \frac{\bar{u}_{\perp-\pi/2,+\pi/2}}{\bar{\Omega}_{-\pi/2,+\pi/2}} \quad \text{and} \quad d_{+\pi/2,+3\pi/2} = \frac{\bar{u}_{\perp+\pi/2,+3\pi/2}}{\bar{\Omega}_{+\pi/2,+3\pi/2}} \quad (4.14)$$

The overall estimate for the angular velocity of a ring is then estimated from a simple kinematic relation, which assumes that the ring rotates as a solid body with some average angular velocity. Thus, the expression yields,

$$\Omega_{eff}^{tilt} = \frac{\bar{u}_{\perp 0,\pi} - \bar{u}_{\perp \pi,2\pi}}{d_{eff}^{tilt}} \quad (4.15)$$

$$\beta = \text{atan} \left[\frac{(\bar{u}_{\perp 0,\pi} - \bar{u}_{\perp \pi,2\pi}) \Delta T}{d_{eff}^{tilt}} \right] \quad (4.16)$$

For the skew angle χ ,

$$\Omega_{eff}^{skew} = \frac{\bar{u}_{\perp 0,\pi} - \bar{u}_{\perp \pi,2\pi}}{d_{eff}^{skew}} \quad (4.17)$$

$$\chi = \text{atan} \left[\frac{(\bar{u}_{\perp -\frac{\pi}{2},+\frac{\pi}{2}} - \bar{u}_{\perp +\frac{\pi}{2},+\frac{3\pi}{2}}) \Delta T}{d_{eff}^{skew}} \right] \quad (4.18)$$

4.3.4 The self-induced vortex ring velocity

It is well known that a stable vortex ring will propel itself along its axis of symmetry (see Figure 4.11). Evaluation of the velocity at a point coinciding on the vortex ring perimeter using equations 4.1 and 4.2 leads to a singularity. There are a number of ways to describe this self-induced axial motion, some of which have also been examined for similar applications by Stubblefield [30] and Montgomerie [38].

Three possible methods for evaluating the self-induced velocity of vortex rings are identified and described below.

Analytical expression for ideal vortex rings

The analytical induced vortex ring velocity equations can be evaluated at ring centroid at the meridional plane. Relative to local ring coordinates, the radial velocity is zero, whilst the axial velocity gives the simplest form of the self induced velocity:

$$u^s = u_z(z = r_i = 0) = \frac{\Gamma}{2R_i} \quad (4.19)$$

This simple formula indicates that an isolated ideal vortex at ring moves with a constant axial velocity along its axis without affecting a change in shape.

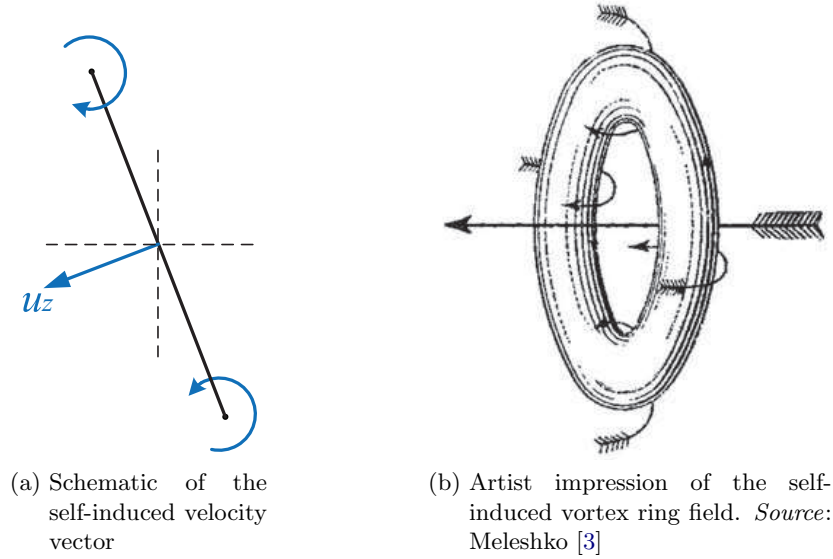


Figure 4.11: Vortex ring self-induced velocity

The Kelvin formula

Fraenkel [39] developed a systematic asymptotic expansion scheme of the Stokes stream function of a vortex ring, leading to a relation between the ring translation velocity U , the strength Γ and the core size r_c ². This allows consideration of a line vortex solution having a finite core. A simple case is considered whereby the core section is circular and has a uniform strength.

The formula is approximated as given in 4.20 and corresponds to the well known Kelvin formula for the translational velocity of a thin vortex ring:

$$U \approx \frac{\Gamma_i}{4\pi R_i} \left[\ln \left(\frac{8R_i}{r_c} \right) - \frac{1}{4} \right] \quad (4.20)$$

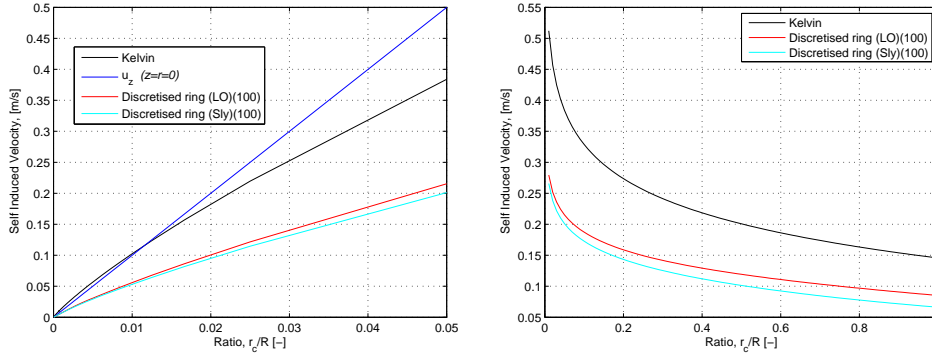
The finite, uniform circular core r_c appears here as the parameter $r_c/R_i \ll 1$.

Vortex ring approximation with straight vortex filaments

The self induced velocity of the vortex ring, or any curved vortex filament, may be thought of as the net effect from all elemental vortex filaments. By finely discretising the vortex ring and evaluating the induced velocity at an arbitrary location on the ring, the resulting quantity is also thought to be representative of the self-induced component.

A consequence of this approach is however the singular behaviour of the analytical velocity expression, as the evaluation point approaches the vortex filament. To desingularise the

²For a complete treatment of the asymptotic approximations to the Fraenkel-Norbury vortex ring family, including thin-ring asymptotics, the reader is referred to Chapter 6 in Wu et al. [40].



(a) Comparison of the induced velocity for a given ring strength, for an increasing rc/R_i ((varying ring radius R_i)) (b) Comparison of the induced velocity for a given ring strength, for an increasing rc/R_i (varying core size r_c)

Figure 4.12: Illustration of methods to compute self-induced velocity

equation, a core model is described and incorporated in order to account for a finite core size. This manifests as shown below, using the model of Vatisstas et al. [41]:

$$u_z = \frac{l^2}{(l^{2k} + r_c^{2k})^{1/k}} \cdot \frac{\Gamma_i}{4\pi l} [\cos(\alpha_1) - \cos(\alpha_2)] \quad (4.21)$$

where Γ_i is the circulation, R is the ring radius, r_c is the vortex core radius, l is the perpendicular distance between a vortex filament and the point of evaluation, and α_1, α_2 are the subtending angles of the line filament and the evaluation point. k can take on integer values 1 or 2, for Scully or Lamb-Oseen vortex core models respectively. A more detailed derivation for this method is given in Appendix C.

Methods comparison

A simple comparison is carried out to identify differences in these approaches. Figure 4.12 illustrates the normalised self-induced velocity component for a varying vortex core radius and ring radius.

For small values of the relative core size, the self-induced components as calculated using the analytical and Kelvin expressions are very much comparable. Interestingly, using a discretised approximation for the vortex ring, the self-induced component differs by approximately 50%, depending on the exact case studied (seen in Figure 4.12b). Highly discretising the ring did not lead to an improved result, and for more than approximately 100 constituent line segments, the estimate for the velocity converged. It was therefore concluded that the ring discretisation method was not an adequate indicator for the self-induced velocity. Montgomerie [38] also noticed this discrepancy and attributed it to a curvature effect which cannot be captured by simply refining the vortex ring approximation with straight line segments.

The choice of the analytical expression over the Kelvin expression is motivated by a brief recall into the nature of the current wake model. We have opted to model the wind turbine

wake using ideal vortex rings, benefitting from the existence of an analytical solution for the resulting induced velocities. In line with this reasoning, it is consistent to consider the velocity evaluated at the ring centroid from the analytical equations as the representative self induced vortex ring velocity. This is backed by the analysis presented above, showing that for small core radii, the two methods yield almost identical results.

4.3.5 Modelling wake expansion

It is desirable to include wake expansion in the analysis. Amongst other things, this will have an influence on the induced velocities at the rotor plane. It is also considered important with respect to the modelling of the detailed vortex ring interactions.

The expansion of the wake is estimated from actuator disk vortex theory as used by Wilson [42] and is further described in Johnson [43]. Depending on the ring's position downstream of the rotor, the radius of the ring is estimated based on this mass conservation expression.

$$u_z = U_\infty [1 - a_z(1 + k_z)] \quad (4.22)$$

where $k_z = \frac{\xi}{\sqrt{1 + \xi^2}}$ and $\xi = \frac{z}{R}$.

By applying the conservation of mass in the cylindrical domain under axisymmetric flow conditions:

$$\frac{1}{r} \frac{\partial(r u_r)}{\partial r} + \frac{\partial(u_z)}{\partial z} = 0 \quad (4.23)$$

A solution of this equation gives the radial velocity in terms of the instantaneous radial position, as well as the local axial velocity gradient:

$$u_r = -\frac{r}{2} \frac{\partial(u_z)}{\partial z} \quad (4.24)$$

This leads to an expression for the radial velocity resulting from the modelled wake expansion and enables determination of the flow streamlines downstream of the rotor.

$$u_r = \frac{U_\infty a_z \eta}{2(1 + \xi^2)^{1.5}} \quad (4.25)$$

where $\eta = \frac{r}{R}$.

Alternatively, the wake radius may be determined using

$$R_w = R \sqrt{\frac{1 - a_z}{1 - a_z(1 + k_z)}} \quad (4.26)$$

This expression was derived for the simple case of uniformly loaded actuator disk in axial flow, producing a straight wake surface and sample expansion trajectories are shown in

Figure 4.13a for different thrust coefficients. Thus, for a skewed wake, the expression is modified such that the quantity a_z is replaced by the total velocity induced at the actuator plane, resolved along the instantaneous wake centreline. This is thought to be more consistent with the current concept for wake expansion used in this model. A comparison is shown in Figure 4.13b whereby equation 4.26 was used to estimate the wake ring radii. A value for $a_z = 1/3$ and $a_z = \frac{u_z}{U_\infty}$ as calculated from the converged wake solution are compared.

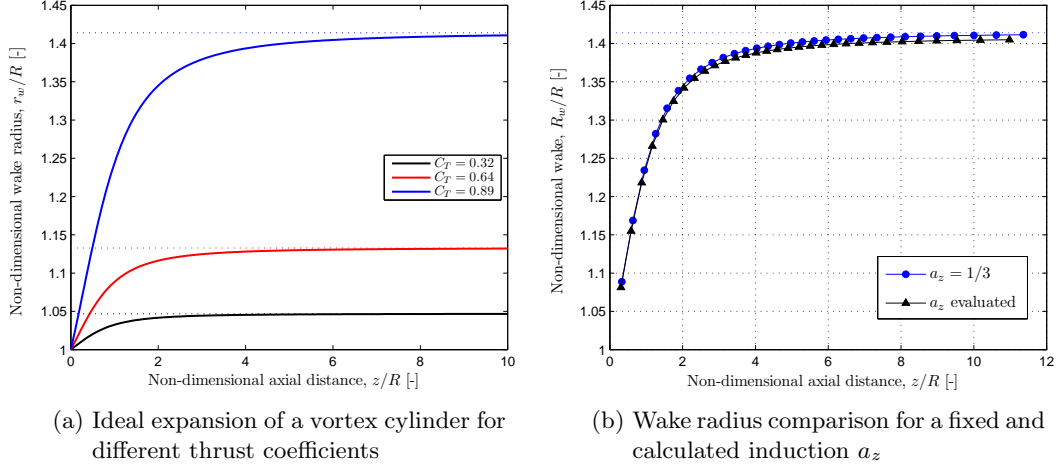


Figure 4.13: Wake expansion characteristics

In the detailed wake simulations, where vortex ring interactions are of particular interest, equation 4.25 is used to estimate the new ring radius. This is detailed further in section 4.5.

4.3.6 Wake strength

An approximate expression for the strength of the released vortex rings Γ_i can be obtained from simple vortex theory of a uniformly loaded actuator disk, generalised for off-design operation:

$$B\Gamma = B\Gamma_{opt} \cdot \frac{3}{2} \cdot \left(1 - \frac{1}{3} \cdot \frac{\lambda}{\lambda_{opt}}\right) \quad (4.27)$$

where

$$B\Gamma_{opt} = \frac{\pi \cdot U_\infty \cdot C_{T(opt)} \cdot R}{\lambda_{opt}} \quad (4.28)$$

where B is the number of rotor blades, U_∞ is the freestream velocity and $C_{T(opt)}$ and λ_{opt} are the optimum thrust coefficient and tip speed ratio. The quantity $B\Gamma$ represents the total bound vorticity on the rotor, subsequently assigned as the ring strength. For obtaining the modified equation 4.27, it was assumed that thrust coefficient can be expressed as

$$C_T = 4a'_z(1 - a'_z) \quad (4.29)$$

where the axial induction factor a'_z can be generalised for non optimum operation, according to $a'_z = \frac{1}{3} \frac{\lambda}{\lambda_{opt}}$. The boundary conditions and corresponding parameters for obtaining equation 4.27 are given in Table 4.2.

Table 4.2: Disk loading characteristics

Tip Speed Ratio	Axial Induction Factor	Thrust Coefficient
λ/λ_{opt}	a'_z	C_T
0	0	0
1	1/3	8/9
3/2	1/2	1

4.4 Interacting vortex rings

For the interaction study of a system of vortex rings, the analytical velocity equations 4.1-4.2 are coupled with the self-induced velocity equation 4.19 and solved using a simple forward Euler scheme with a minimum time step of $\Delta t = 1 \times 10^{-4} s$ to ensure a converged solution. This sensitivity study is presented in Chapter 5. The mutual interaction of physical vortex rings is seldom observed at length due rapidly evolving viscous effects. However, for these inviscid simulations, two vortex rings which initiate leapfrogging should remain doing so indefinitely. It is also known that one such condition for initiating and maintaining the leapfrogging action is that two rings are perfectly aligned coaxially. Any departure from this ideal can result in some initial interaction, but would almost immediately be followed by ring merging.

As mentioned briefly in section 4.3.2, when interested in the interaction of coaxial vortex rings, one need only evaluate the velocity at a single point on the ring periphery. These axial and radial velocities are then sufficient to predict changes in the ring radius and axial position.

4.5 Simulations Description

Having described the main modelling tools to be implemented into the models, the procedure for initialising and conducting the simulations are outlined in the following section.

4.5.1 Discrete FW-VRM

The free wake vortex ring model with time stepping per rotor revolution is described in this section along with the main input parameters and procedure.

Input parameters

The main model input parameters for simulating the rotor wake in this manner involve the following

- the number of wake revolutions to simulate, N_{rev}
- the operating tip speed ratio, λ
- the inflow conditions, including the yaw angle Ψ , the shear exponent m
- the turbine hub height HH , if the presence of the ground plane on the flow is to be taken into account, and/or if a sheared profile has been specified.

The time step can be estimated from the chosen tip speed ratio λ as $\Delta T = \frac{2\pi}{\omega} s$, where the rotational frequency $\omega = \frac{\lambda U_\infty}{R} s^{-1}$, and R is the rotor radius.

If the vortex rings are chosen to be representative of a wake revolution due to a single blade (rather than a combined ring representing the total bound circulation), then the total number of wake rings N and time steps T actually used will be $nrev \times B$, and each successive vortex ring is assigned the strength of a single blade³. This is practically implemented by decreasing the time step ΔT to $\Delta T/B$, therefore effectively increasing the tip speed ratio and obtaining more wake rings.

Algorithm

The simulation procedure for predicting the evolution of the rotor wake follows the procedure described below.

1. A starting vortex ring is initiated at $t = 0$ and placed at a location depending only on the inflow conditions, since no other wake rings will influence its motion. Thus,

$$\mathbf{u}_i = \mathbf{u}^s + \mathbf{u}^v + \mathbf{U}_\infty \quad (4.30)$$

where \mathbf{u}^s is the self-induced velocity and, if included in the simulation, \mathbf{u}^v is the induced velocity at each point due to the presence of the ground; \mathbf{U}_∞ is the free-stream velocity field.

The orientation of the rings is also estimated according to equations 4.16 and 4.18. These velocities are evaluated at the rotor plane for the new wake rings.

2. A second vortex ring is then shed at a location according to

$$\mathbf{u} = \mathbf{u}^s + \mathbf{u}^m + \mathbf{u}^v + \mathbf{U}_\infty \quad (4.31)$$

where, \mathbf{u}^m is total mutually induced velocity contribution from other wake rings present in the system.

The averaged velocities at each wake vortex ring is then computed. Similarly, the ring orientation is also predicted, now with the influence of the other wake vortex rings.

³Note for this type of simulation, $N = T$

3. All subsequent vortex rings are shed as explained in step 2.

During each time step, the influence of the wake on itself is predicted by subsequently considering each wake ring, and calculating the induced velocities affected upon the other vortex rings, until all rings have been cycled through. The position vector of the ring centroid in terms of global coordinates \mathbf{C}_i , and orientations are then updated using a first order Euler scheme according to

$$\mathbf{C}_i^{t+1} = \mathbf{C}_i^t + \frac{1}{2} \cdot (\overline{\mathbf{u}}_i^{t+1} + \overline{\mathbf{u}}_i^t) \cdot \Delta T \quad (4.32)$$

where t denotes the instantaneous time.

The radius of the rings in this simulation method are estimated using the principle of flow conservation and the analytical expression given in equations 4.22 and 4.26.

4.5.2 Coupled FW-VRM interaction model

The most detailed refinement of the model combines the freely convecting wake model with the detailed interaction scheme explained in the section 4.4.

Input parameters

Input parameters for investigating the detailed vortex ring interactions within the wake are similar to the FW-VRM concept. Additionally, also required for this investigation are

- the fine time step Δt for updating the ring positions

Algorithm

Essentially, the main difference between this model variant and the discrete FW-VRM, is that between the releasing of wake rings, the detailed interactions are captured using the finer time step, specified as an input parameter.

The algorithm for this model therefore follows the exact procedure defined in section 4.5.1, with the following key modifications:

- when two or more rings have been released, the influence of the wake rings on each other is predicted and the positions updated using equation 4.32, using the fine step Δt
- a form of triggering algorithm is set up in order to release a new wake ring after $\frac{\Delta T}{\Delta t}$ fine time steps have been simulated.

- the updated ring radii R_i^{t+1} are estimated by summing the effect of expansion due to vortex cylinder theory (equation 4.25) and the resolved radial velocity on the ring periphery due to the other influencing wake rings.

$$R_i^{t+1} = R_i^{t+1} + \frac{1}{2} \cdot (u_{r,i}^{t+1} + u_{r,i}^t) \cdot \Delta t \quad (4.33)$$

where $u_{r,i}$ in this equation represent the summed radial velocity due to vortex cylinder and resultant mutual induced radial velocity.

4.5.3 Detailed vortex ring interactions

Input parameters

The input parameters for the detailed vortex ring interactions are most notably,

- the simulation time step Δt and the number of prescribed vortex rings in the array
- the initial relative positions of the rings, i.e. the ring pitch h
- the ring strengths, which may be prescribed through equations 4.27 and 4.28 in order to assimilate the investigation with realistic strength values
- the ring radii

Algorithm

The procedure for this type of simulation is simply to calculate the induced velocities at single nodes on the ring peripheries and update the axial and radial positions, again using the first order Euler time integration scheme.

4.5.4 Dealing with starting effects on the FW-VRM

In order to study the influence of close vortex filament interactions, the model must be free from artificial perturbations⁴. An in depth study of isolated vortex ring interactions will be described in a later section, and it becomes clear that the motion is particularly sensitive to axial relative axial displacements and changes in relative radius and strength.

Upon start-up, the rotor wake starts to develop in a gradual manner. Thus, the older wake vortex rings experience throughout a different flow field. Failing to recognise this could lead to misinterpretation of the behaviour of these older wake rings.

To overcome this, the simulation could simply be run for longer than normal - the older portion of the wake most affected by the initiation procedure could be disregarded, and only the newer section of the wake is studied. This ensures that interesting characteristics identified in these newer wake rings were not the result of the initiation procedure.

⁴Artificial perturbations here does not refer to the usual understanding of the term, which is related to numerical diffusion, incorrectly triggering some unwanted physical phenomena

Alternatively, to circumvent the lengthier resources in running for a longer time, the simulation can be initialised with a partially prescribed wake structure. This can be considered an initial guess for the system with which to initialise. The disadvantage of this method is that any initial mismatches between the prescribed wake and calculated position of the first vortex ring element could give rise to unwanted artificial perturbations.

Model testing and preliminary results

In this chapter, the implementation of the model is assessed by investigating some of the behavioural characteristics of vortex rings and the ability of the current model to capture close ring-ring interactions. As described in Chapter 4, two forms of simulations will be conducted and thus suitable methods of verifying the models are required. The types of simulations are summarised again here:

1. Wake evolution-type simulations, which involve simulating the rotor-generating VR wake elements. These will provide qualitative information about the evolution of the wake, and the effect of external perturbations.
2. A vortex ring interaction study to understand the nature of mutual interaction and limits of stability

Vortex ring velocity fields are visualised and explained in section 5.1. The ability to correctly predict ideal vortex ring leapfrogging and interaction is investigated in section 5.2 with two and three ring vortex systems. The trajectory profiles are predicted for a set of chosen parameters and compared with those found in literature. Finally, a small study is performed in section 5.3 to show the behaviour of an array of vortex rings and the ability of the FW-VRM to predict results in accordance with actuator disk theory.

5.1 Vortex ring behaviour - induced velocity fields

5.1.1 Dual vortex ring system

The correct prediction of the induced velocities from vortex rings is imperative for the functioning of the model. Visualising the induced velocity field is a useful aid to determine whether the sense and magnitude of the velocity is correct. A simple two and three vortex ring array is analysed from the perspective of the induced velocities at the ring planes.

The layout of the arrays is depicted in Figure 5.1 and in Figure 5.7 for the triple ring system. The ring radii and separation is unity, as well as the ring strength, which also has the same sign.

In Figure 5.2, the coaxial dual vortex ring induced velocities are shown. All radial velocities are normalised by the maximum in-plane radial velocity whilst the axial induced velocity is normalized with the maximum axial induced velocity within the ring array. This allows for a better relative comparison of the mutual effects. With the two rings having the same sense of strength, the axial induced velocity is equal at both ring planes, both in magnitude and direction. The magnitude is highest in the region corresponding to the centroid of the *inducing* ring and gradually decreases with radial position. Conversely, the radial induced velocity is weakest towards the inducing ring centroid, and strengthens towards the inducing ring periphery. The direction of the radial induced velocities is also consistent given the orientation of the rings: the front ring induces *contracting* radial field on the first ring, whilst the first ring gives rise to an *expanding* field on the second ring. The occurrence of the opposing radial fields for this case of coaxial vortex rings, in fact, gives rise to the observed leapfrogging behaviour of vortex rings.

Offsetting the vortex rings in the xy plane as shown in Figure 5.1b, produces velocity fields as shown in Figure 5.2. Similar trends as with the coaxial system are seen. Most notably however, in this case, the mutual effect of off-centering vortex rings is that a resultant destabilising velocity is set up. This contrasts to the previous situation where the velocity field was evenly balanced. The unbalanced axial velocity field (see Figures 5.14a and 5.14a) leads to skewing and tilting.

5.1.2 Triple vortex ring system

The third illustrative case for a triple vortex ring system is shown in Figures 5.4 and 5.5. A distinctive feature is that the axial velocity field at the mid-ring is augmented by the presence of the adjacent rings, whilst the resultant radial field is null. The latter only occurs because the rings are evenly spaced and therefore the induced contribution from each adjacent ring is exactly equal and opposite. In light of the previous illustrations of offset vortex rings, it can be expected that the vortex ring system can destabilise, subject to non-uniform conditions, such as:

- uneven ring spacing or pitch, h
- offsets in the relative ring positions, such as the case considered in Figure 5.2

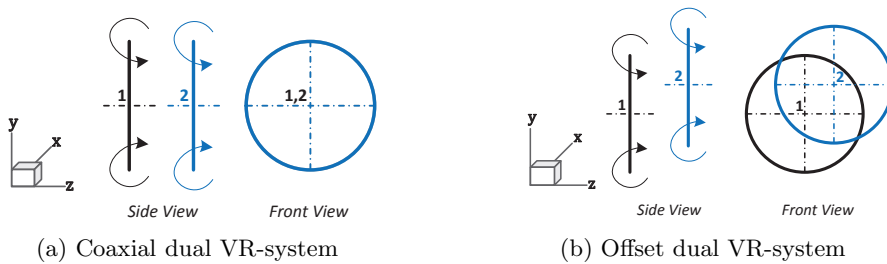


Figure 5.1: Layout of the investigated dual vortex ring system

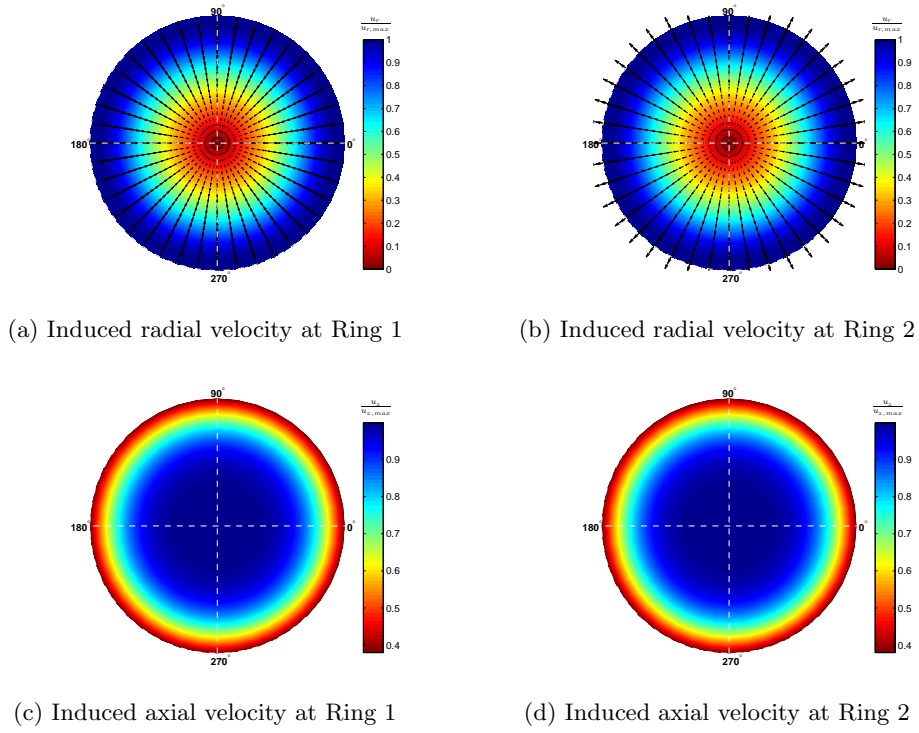


Figure 5.2: Induced velocities in the ring planes of a coaxial dual ring system

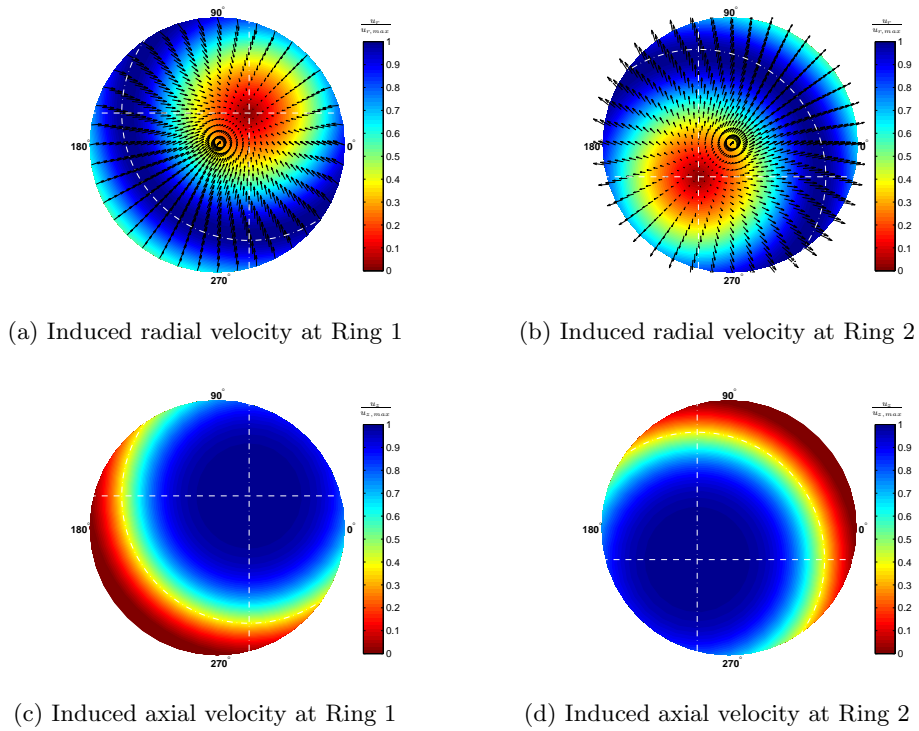


Figure 5.3: Induced velocities in the ring planes of an offset dual ring system

- differing ring element radii, R_i
- differences in the relative strengths of the vortex rings, Γ_i

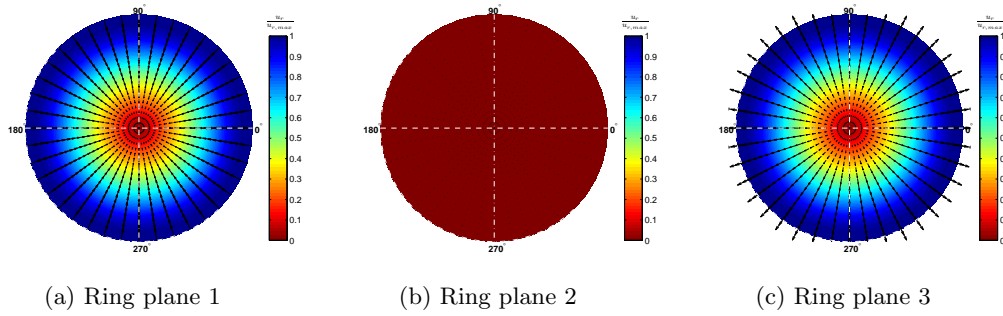


Figure 5.4: Induced radial velocities at the ring planes of a coaxial triple ring system

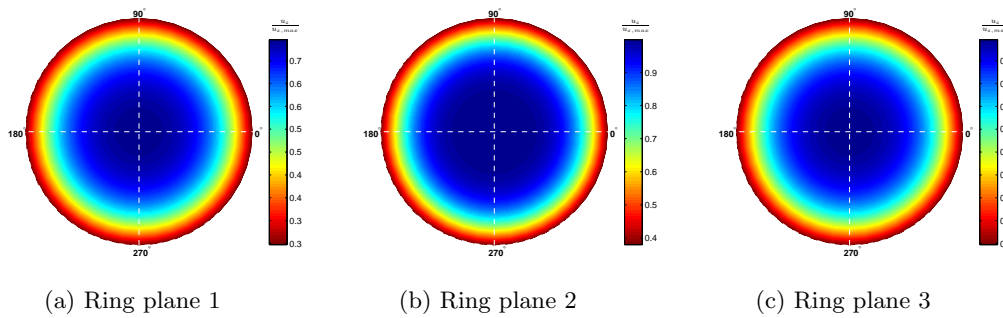


Figure 5.5: Induced axial velocities at the ring planes of a coaxial triple ring system

The mutual interaction of two coaxial vortex rings where leapfrogging is observed follows a notable periodic pattern, as described in the opening paragraphs of this section. With a larger number of vortex rings in the system however, characterising the exact progression of mutual interaction becomes more complex. Furthermore, it is not possible to anticipate what effects the smallest of perturbations will have on the dynamics of the ideal vortex rings. Each case must be considered separately and the resulting motion is often described as chaotic, as noted also in Meleshko [3].

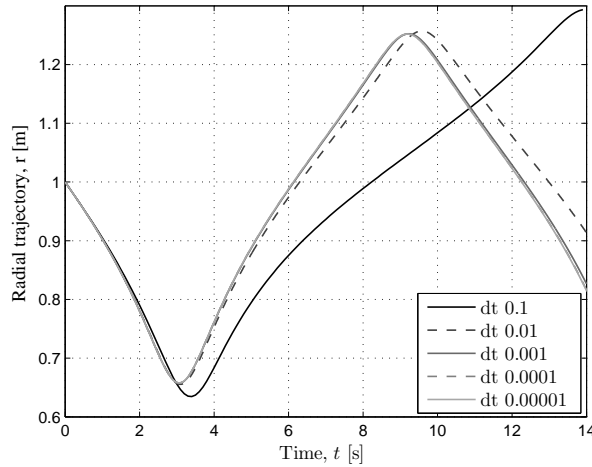


Figure 5.6: Convergence behaviour for the solution of equations for predicting vortex ring mutual interaction

5.2 Vortex ring interactions

5.2.1 Convergence to a stable solution

It is important to ensure that a sufficiently refined time steps is chosen for predicting the correct motion of the system of vortex rings, when we are interested in precise interaction dynamics. A control case is defined for a dual vortex ring system with rings of unit radius, strength and separation ($h = R$). With this configuration, the vortex rings exhibit leapfrogging motion, but if the time step is not sufficiently small, the separation of the rings after performing one interaction cycle gradually increases and the solution diverges. Clearly, for this inviscid ideal description of the flow, vortex rings which initiate leapfrogging should continue to do so indefinitely. In Figure 5.6, the temporal trajectory of the front is shown. With an increasingly refined time step Δt , the path converges and a level of $\Delta t = 0.0001$ is deemed suitable for a reasonable level of accuracy, within practical constraints.

5.2.2 Mutual threading behaviour of a dual vortex ring system

Various trajectory investigations were carried out to observe the behaviour and limitations of vortex ring mutual interactions using the present model. Validating such results is vital but not straightforward due to lack of detailed data in literature. Unique results are found in Meleshko [3], who treated the subject of vortex ring interaction extensively and presents results of the modified *Dyson Model* for the case of two and three vortex ring systems. This author [3] claims that the presented trajectories have been partially validated experimentally.

Meleshko [3] reports that some experimental validation of this model was conducted and good agreement was obtained for both the actual trace, as well as agreement with the constraints shown in Figure D.1b. The red marker and enclosed red region pertain to

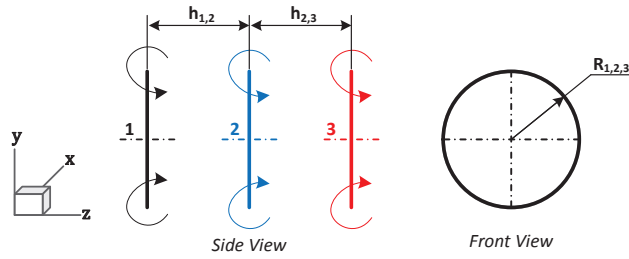


Figure 5.7: Triple vortex ring system layout

the trajectory and conditions given in Figure D.1a. The corresponding blue indicators correspond to Figure D.1c. It is clear that in the latter, the conditions lie outside the predicted permissible region, a fact which reflects in the slip-through motion obtained, rather than a periodic leapfrogging action. These trajectories have been obtained by the present model and are shown in Figure 5.8. For the leapfrogging scenario, snapshots of approximately one cycle¹ are shown in Figure 5.9.

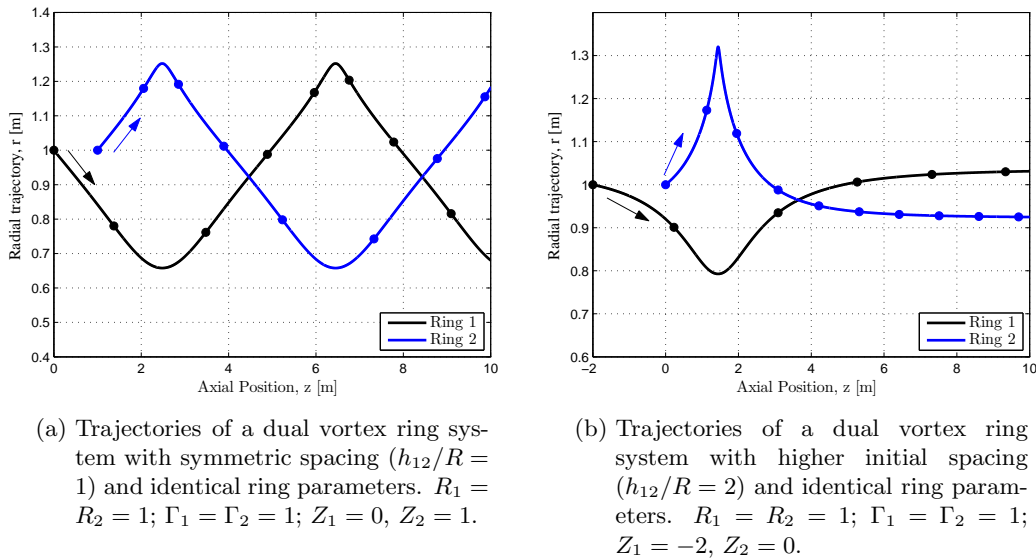


Figure 5.8: Dual vortex ring interaction trajectories

5.2.3 Mutual threading behaviour of a triple vortex ring system

In the work of Meleshko [3], the interaction of three vortex rings of the same sense of strength is also addressed. This problem has received much less attention than the case of two interacting vortex rings. The addition of the third ring to the system significantly complicates the problem. It is observed that with a three ring vortex ring field, the triggering of pairing phenomena is extremely sensitive to the initial placement and conditions of the vortex rings. As was seen for the case of two rings, a certain range exists wherein *mutual threading* will take place. With three rings, three possible pairing combinations

¹One mutual interaction cycle is complete when two vortex rings return to their original starting positions

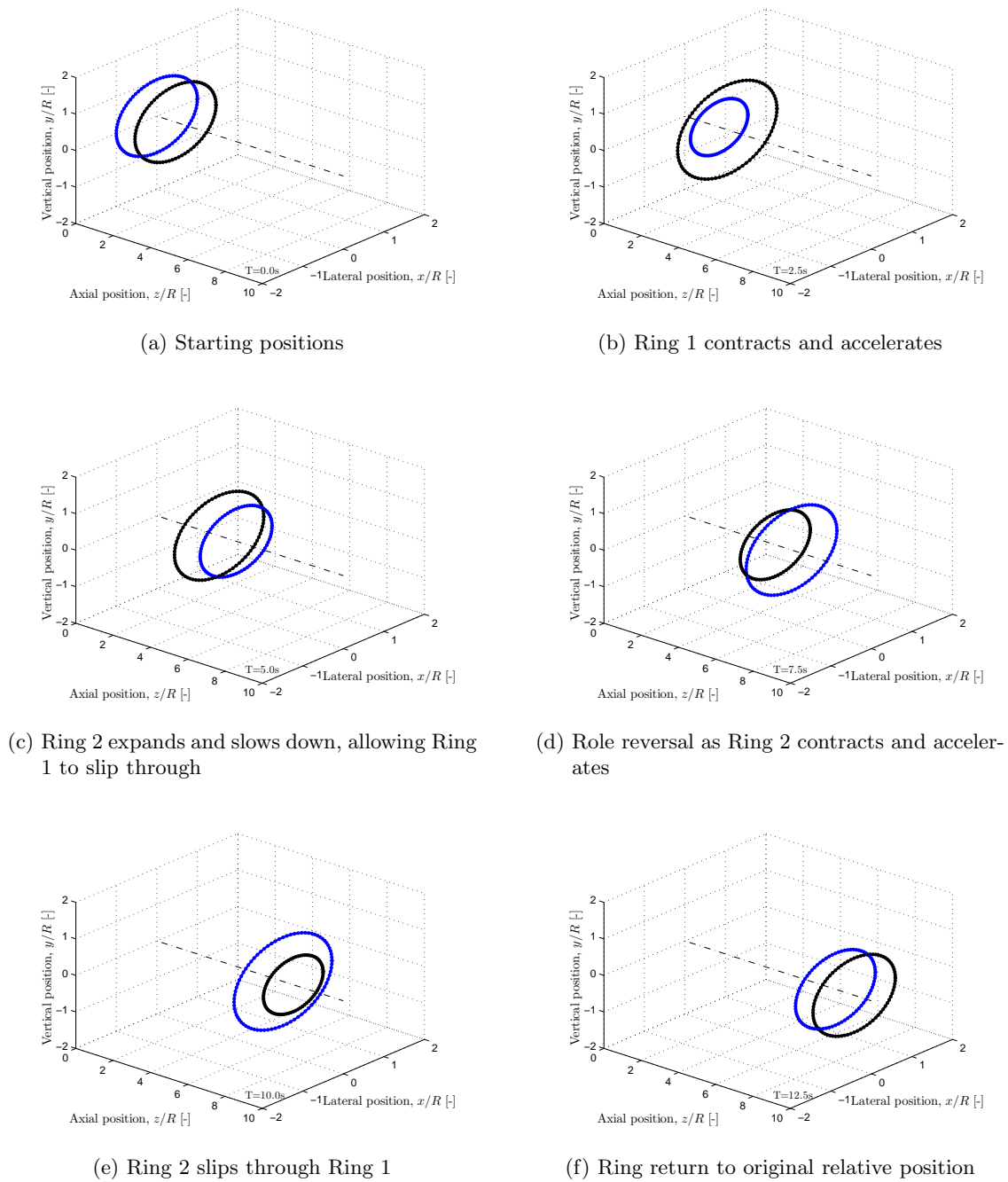


Figure 5.9: Motion of a dual vortex ring system displaying approximately one leapfrog cycle

are possible, and the particular combination is highly sensitive to the initial parameters. The following trajectory plots serve to verify the current model, and also to illustrate some interesting dynamics, in response to small changes in ring separation and relative strength changes.

The current prescribed vortex ring model is tested for the case of three adjacent vortex rings, with parameters as used in [3] to allow for a visual verification of the dynamics and

pairing phenomena initiated in the flow field. Two cases are presented, with parameters used as summarised in Table 5.1.

Table 5.1: Parameters for testing 3-ring interaction with a variation in (a) initial ring plane separation: $\Gamma_1 = \Gamma_2 = 1$; $R_1 = R_2 = 1$ (b) initial ring strength. $R_1 = R_2 = 1$; $h_{12} = h_{23} = 1$

Ring Number	(a)			(b)		
	z_1	z_2	z_3	Γ_1	Γ_2	Γ_3
1	0.00	1.00	2.00	2	1	1
2	0.00	1.01	2.00	1	2	1
3	0.00	1.00	2.01	1	1	2

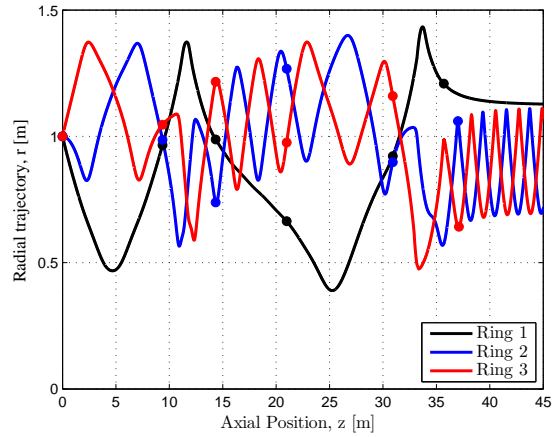
In Figure D.2a, adjusting the position of the middle and end vortex ring by just 1% in the axial direction leads to remarkably dissimilar spatial trajectories. This implies that system stability with three or more rings becomes extremely sensitive to relative axial spacing. The trajectories obtained from the vortex ring model are shown in Figures 5.10

Sensitivity to changes in ring strength

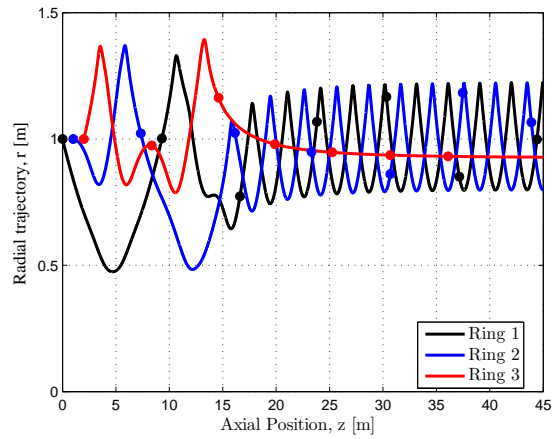
System sensitivity to changes in strength (Figure D.2b) were also obtained by Meleshko et al. [3]. Corresponding trajectory predictions from the vortex ring model compare well as shown in Figures 5.11.

These results highlight the fact that with increasing degrees of freedom, the vortex ring system behaviour and response to small disturbances appears chaotic in nature. One may however ascertain from these simulations that there is always a tendency for pairing, that is that any two vortex rings, given the right conditions, will tend to mutually interact (leapfrog). In the three-ring system, for all three cases presented, a prevalent "higher frequency" interaction takes place, whilst a single unpaired ring interacts about the leapfrogging sub-system.

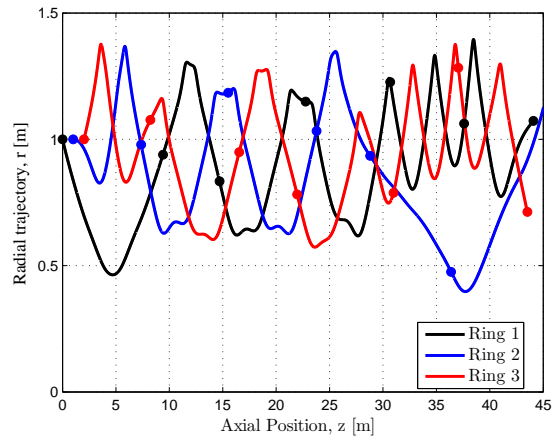
In Figures 5.11a to 5.11c, simulation results are presented for the case of varying strength within a three-ring system, verifying the model against those of Meleshko [3]. Again, the designation "Ring 1", "Ring 2" "Ring 3" is used to denote the three successive rings - Ring 1 at $Z = 0$, and so on. The vortex ring positions at a number of evenly timed instances are indicated by the filled circular markers, equispaced in 10s time intervals.



(a) VR system with symmetric spacing and identical ring parameters: $R_1 = R_2 = R_3 = 1$; $\Gamma_1 = \Gamma_2 = \Gamma_3 = 3$; $Z_1 = 0$, $Z_2 = 1$, $Z_3 = 2$.

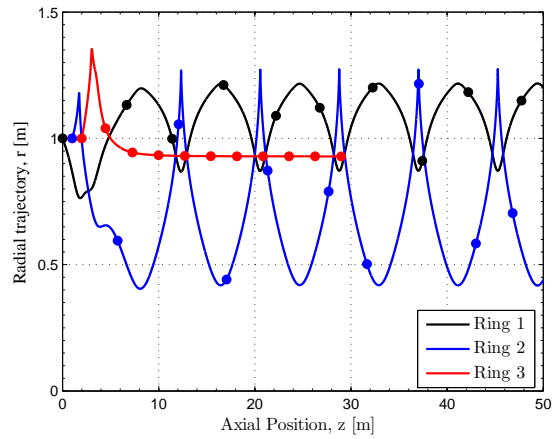


(b) VR system with the *second* ring subject to a slight disturbance in the axial position: $R_1 = R_2 = R_3 = 1$; $\Gamma_1 = \Gamma_2 = \Gamma_3 = 1$; $Z_1 = 0.00$, $Z_2 = 1.01$, $Z_3 = 2$.

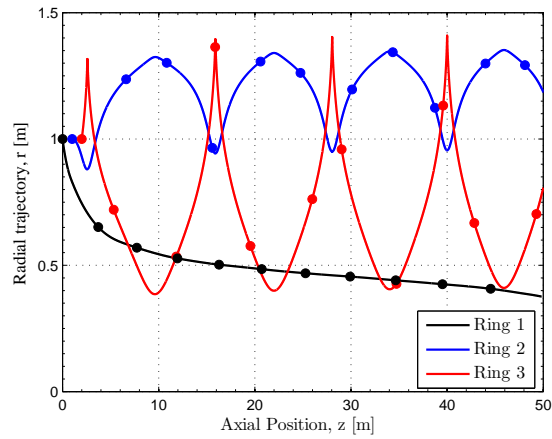


(c) VR system with the *third* ring subject to a slight disturbance in the axial position: $R_1 = R_2 = R_3 = 1$; $\Gamma_1 = \Gamma_2 = \Gamma_3 = 1$; $Z_1 = 0.00$, $Z_2 = 1.00$, $Z_3 = 2.01$.

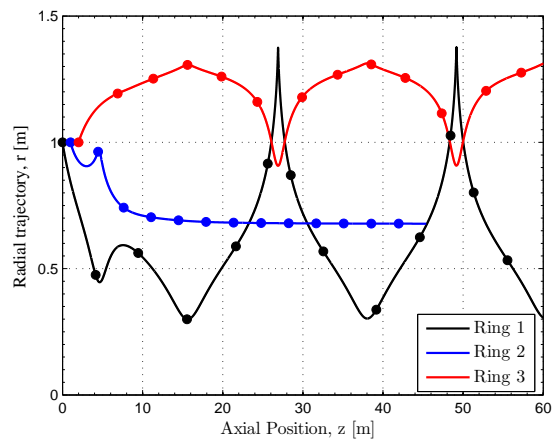
Figure 5.10: Spatial trajectory of a triple vortex ring system subject to small spatial (axial displacement) perturbations



(a) Spatial trajectory of triple vortex ring system subject to a change in strength of the *first* ring.
 $R_1 = R_2 = R_3 = 1.0$; $\Gamma_2 = \Gamma_3 = 1$, $\Gamma_1 = 2$; $Z_1 = 0$, $Z_2 = 1$, $Z_3 = 2$.



(b) Spatial trajectory of triple vortex ring system subject to a change in strength of the *second* ring.
 $R_1 = R_2 = R_3 = 1.0$; $\Gamma_1 = \Gamma_3 = 1$, $\Gamma_2 = 2$; $Z_1 = 0$, $Z_2 = 1$, $Z_3 = 2$.



(c) Spatial trajectory of triple vortex ring system subject to a change in strength of the *third* ring.
 $R_1 = R_2 = R_3 = 1.0$; $\Gamma_1 = \Gamma_2 = 1$, $\Gamma_3 = 2$; $Z_1 = 0$, $Z_2 = 1$, $Z_3 = 2$.

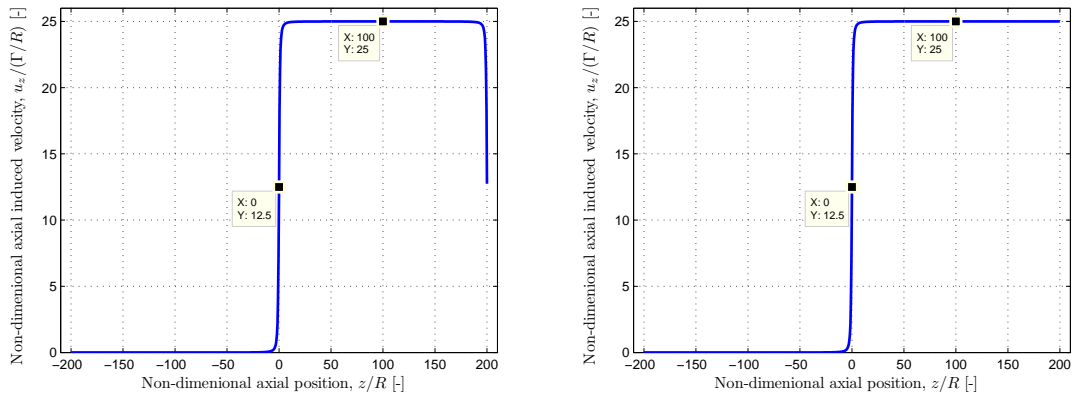
Figure 5.11: Spatial trajectory of a triple vortex ring system subject to small strength perturbations

5.3 Vortex rings as wake elements

The representation of the wake using vortex rings requires verification to show that indeed, under ideal conditions, results in accordance with the momentum and actuator disk theories are obtained. This can most easily be applied to the assessment of the average induced axial velocity at the actuator disk plane, as well as to assess the characteristics of a large vortex ring array.

5.3.1 Actuator disk characteristics

If a sufficiently large system of vortex rings is defined with a relatively small ring separation, the centreline axial velocity should approach that of a semi-infinite vortex cylinder. The latter is the simplest type of actuator disk wake that can be described. The salient point here is that the velocity induced at the location of the disc should be half that induced in the far wake.



(a) Induced axial velocity along the centreline of a large vortex-ring array

(b) Analytical axial centreline velocity

Figure 5.12: Actuator disk characteristics

Figure 5.12a shows the normalised induced axial velocity due to the vortex ring array, and that due to the analytical expression 4.22 is shown in Figure 5.12b. The vortex ring array yields a similar velocity profile with the exception that the axial velocity at the end of the array will always tend towards the value at $z/R = 0$. This is the case since we are approximating the continuous surface of vorticity with discrete vortex rings, and thus, as also explained and illustrated in section 5.1, the axial components of the induced velocity is augmented at the mid-rings, and decreases towards the outer rings. Nonetheless, it can be argued that using vortex rings in this manner, one can expect that for a sufficiently developed wake, the induced velocity trends correspond to those predicted from actuator disk theory, which are also in agreement with 1D momentum theory.

To elucidate the situation at the rotor plane, a refined plot is shown in Figure 5.13 where the predictions from both methods considered for this small study are practically identical and show that an induced velocity of twice that at the actuator disk is predicted in the far wake.

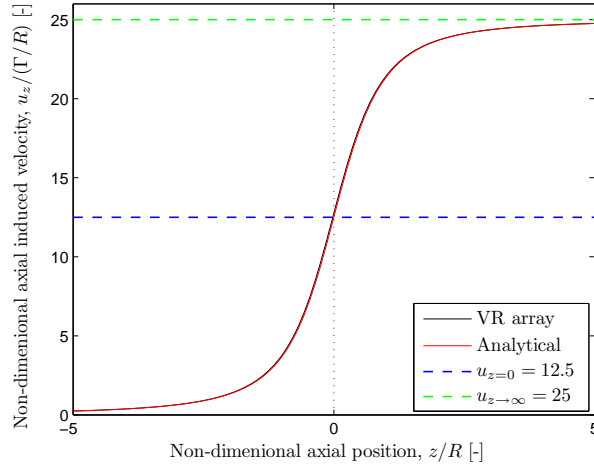


Figure 5.13: Comparison of the analytical and VR array induced velocities in the actuator region

5.3.2 Axial induced velocity

Figure 5.14a shows the local axial induction factor for the converged case of $N_{rev} = 15$. The resulting axial induction factor at the actuator plane is seen to converge to the ideal quantity of $1/3$. It is important to recall at this point that the strength of the vortex rings is prescribed based on the prescription of the ideal operating tip speed ratio and thrust coefficient. Thus, convergence here is influenced by two main properties of the wake:

- the overall number of rings representing the wake (or, equivalently, the number of wake revolutions taken into consideration), and
- the proximity of the first wake ring (or first 3 rings, which equivalently represent one wake revolution) to the actuator plane

In light of this, it is observed that the sensitivity of the induced velocities at the actuator disk to the position of the first wake ring (i.e. the ring closest to the actuator disk) is significant. This is to be expected given the manner in which the induced velocities from the ideal vortex ring behave with increasing distance from the ring centroid (see for e.g. Chapter 4, Figures 4.6a and 4.7a.)

The position of this wake element is of course influenced by older wake rings. This also highlights the importance in clarifying the manner in which the wake rings actually reflect a true developing helicoidal vortex wake. In contrast to say a lifting line rotor representation with ensuing trailing vorticity, there is an immediate influence on the induced velocities from trailing filaments closest to the rotor. With the ring representation, a wake revolution of trailing tip vortex segments from all blades is approximated by a single vortex ring of combined strength, $B\Gamma$. It is found that placement of this ring at the half-pitch location, denoted $h_{1/2}$,² leads to a much better estimation of the induced

²The full pitch position is considered the axial displacement of a wake node after a single time step or rotor revolution. The half pitch is thus half this displacement, i.e. $\frac{\Delta T}{2} * U(1 - a_{z,i})$.

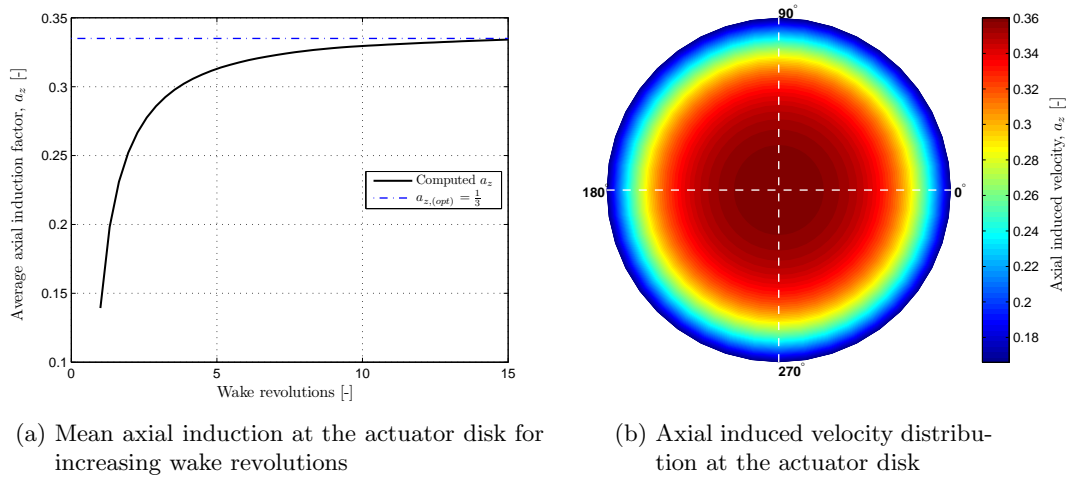


Figure 5.14: Model prediction of the average axial induced velocity for ideal operating conditions

velocity at the actuator disk. In contrast, representing wake rings due to different blades distinctly requires placement of the rings at the $h_{1/3}$ position and the strength of each ring is then due also to a single blade, Γ .

Given that the current formulation does not include turbulence and viscous effects, there is a larger influence from older wake elements. This is particularly clear when considering higher tip speed ratios since relative ring spacing is smaller and the ring system is overall closer to the actuator disk. An illustration of the converged induced velocity field at the actuator disk is shown in Figure 5.14b.

Results

In this chapter, the main results from the presented models are discussed in relation to the general development of the wake. Wake visualisations are also shown to support the observations. The leapfrogging of vortex rings, typical wake conditions is investigated, with a particular focus on drawing comparisons with the work of Medici et al. [2]. Finally in the last section, a more detailed investigation into the mutual inductance effects on the development of the wake is presented with particular reference to the work Felli et al. [7].

6.1 Test Cases

General simulations are carried out for a hypothetical wind turbine rotor with idealised operating parameters, shown in Table 6.1.

Table 6.1: Actuator disk characteristics

Parameter	Value	Units
Radius	50	[m]
λ_{opt}	5	[-]
$C_{T,opt}$	0.889	[-]
$(B\Gamma)_{R,opt}$	-5.58	[m/s]

These nominal parameters are used throughout in order to maintain a level of consistency and to ensure that the observed phenomena are representative of realistic operational characteristics.

6.2 Vortex ring array dynamics

In this section, some simple simulation results with regards to a destabilised vortex ring system are presented. In the earlier Chapters 4 and 5, it was seen that small perturbations

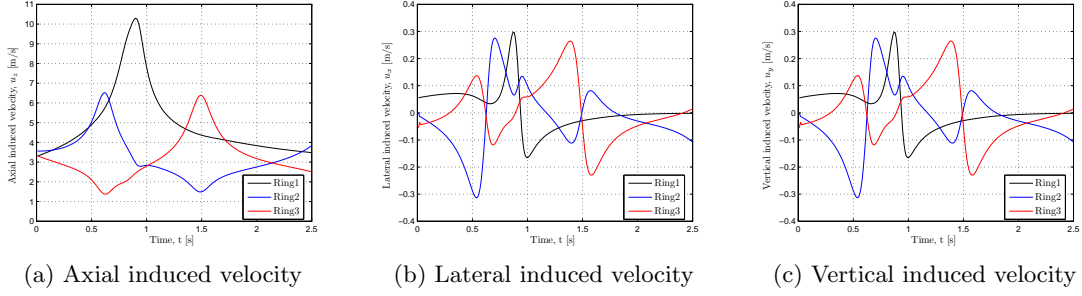


Figure 6.1: Induced velocities for a triple ring system with an offset middle ring.

in the vortex ring system set up non-axisymmetric, destabilising velocity field which could give rise to the mutual interaction mode and dispersal of the vortex rings.

A system of three and 10 vortex rings are investigated to obtain further insight into the dynamics of vortex rings, as well as to help explain other phenomena occurring in the wake model.

Table 6.2: Average axial and radial velocities at $t = 0$

Ring No.	u_z [m/s]	u_x	u_y [m/s]
Ring 1	3.311	+0.055	+0.055
Ring 2	3.560	0	0
Ring 3	3.311	-0.055	-0.055

6.2.1 Triple vortex ring array

In Figure 6.1, the induced velocities are shown for a triple vortex ring system, as designated exactly as shown in Figure 5.7. The difference is that the middle ring has been offset equally in the x and y directions by $0.25R$. The ring strengths are equal and have the same sense.

With reference to Table 6.2, it is seen that the initial lateral and vertical velocities induced at the end rings are equal and opposite, whilst at the middle ring, these components counter balance and the resultant velocity is null. The axial velocity as expected is highest at the middle ring since the effects from the other rings are reinforced at this location.

Figure 6.2 shows the ring translations for this configuration.

Whilst this example illustrates further the dynamics of vortex ring system, a limitation of the model also becomes evident. It is observed that as soon as two rings approach one another in a misaligned manner, the rings simply thread through each other. This implies that the rings physically overlap at some instant and continue interacting as if leapfrogging coaxially. It should therefore be understood that the moments leading up to this type of interaction, and the instances after are invalidated due to this overlap. Physical vortex rings with the same sense of strength, travelling in the same direction but with a slight misalignment will indeed interact and perform a *partial leapfrog*, but are

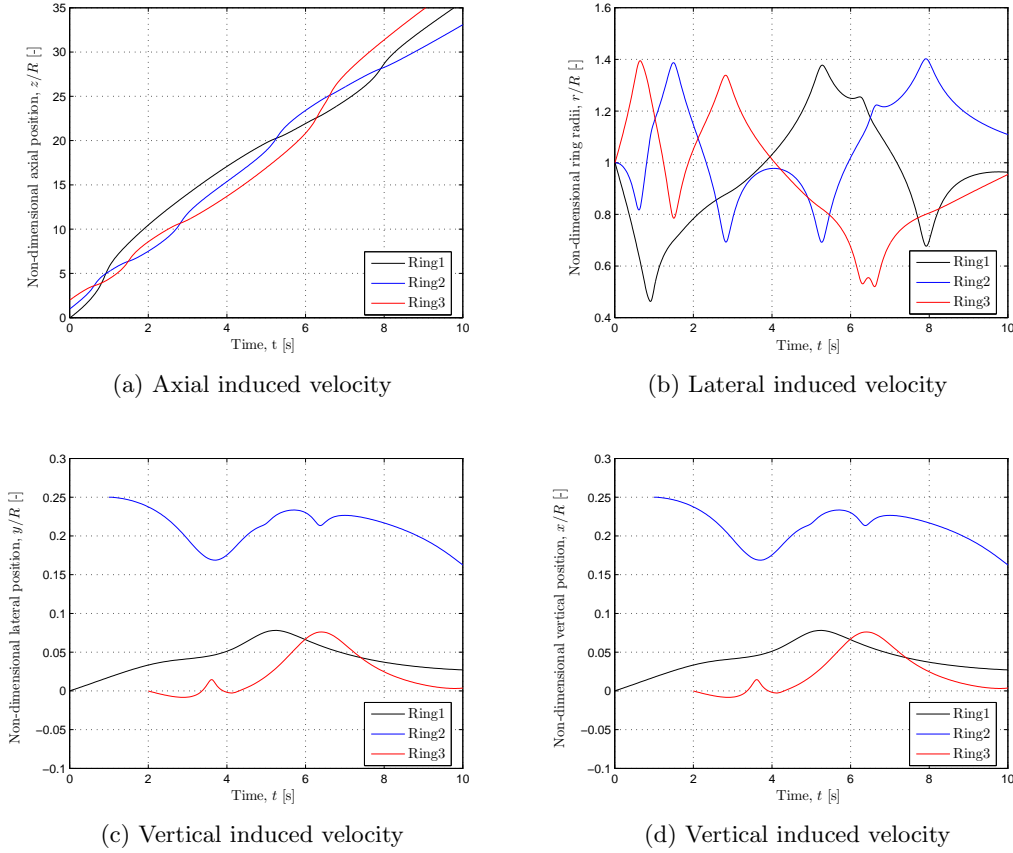


Figure 6.2: Ring trajectories for the case on an offset mid-ring.

almost immediately destroyed because of the strong overlapping and entangling vortex filaments. Lim [44] performed experiments on physical vortex rings and identified that the slightest of variations in vortex ring alignment caused loss of flow axisymmetry. This led to non-axisymmetric vortex pairing, which ultimately, annihilates the structure of the vortex rings via filament entanglement and the formation of secondary vortices. This transition to turbulence and 3D flow cannot be predicted with the current vortex ring model, and it is thus imperative to keep this limitation in mind.

6.2.2 Prescribed expanded rings

It was considered useful to investigate a system of expanded vortex rings, corresponding to the optimum rotor wake profile. Seven rotor revolutions were considered with a wake system set up accordingly, that is using the optimum value for the strength of the wake. Two examples are shown, which correspond to a two- and three-bladed rotor. That is to say that the ring pitch is varied accordingly with the number of blades B , using the following simple expression:

$$h/R \approx \frac{2}{3} \cdot \frac{2\pi}{B\lambda} \quad (6.1)$$

where an ideal induction factor of $1/3$ is assumed. Assuming an optimum $\lambda = 5$ for both cases, the non-dimensional ring pitch using this estimation is approximately $0.28R$ and $0.42R$ for the two- and three-bladed cases respectively. The resulting radial ring trajectories are shown in Figures 6.3 and 6.4.

A few salient points are identified whilst comparing these two radial trajectories:

- *The vortex ring system tends to induce opposing radial fields at either end, with a predicted contraction in the what would be the downstream location of the wake.*

In free wake simulations, a similar effect is observed. Despite the effect the starting ring has on this phenomenon, wake contraction following the initial expansion phase is in fact something which has been observed in controlled experiments and numerical simulations.

- *Stronger pairing is observed for the higher number of blades, and hence for a finer pitch.*

As seen in Figures 6.3 and 6.4, the strongest interactions take place on the end vortex rings due to the augmented radial field in those regions. Note in particular rings 1 and 2, where the mutual interaction is particularly visible over the $25s$ simulation. For the case of $B = 2$, it is seen that over a $25s$ period, approximately a quarter cycle leapfrog has been completed by these two rings, where as with the case of $B = 3$, approximately half a cycle is completed.

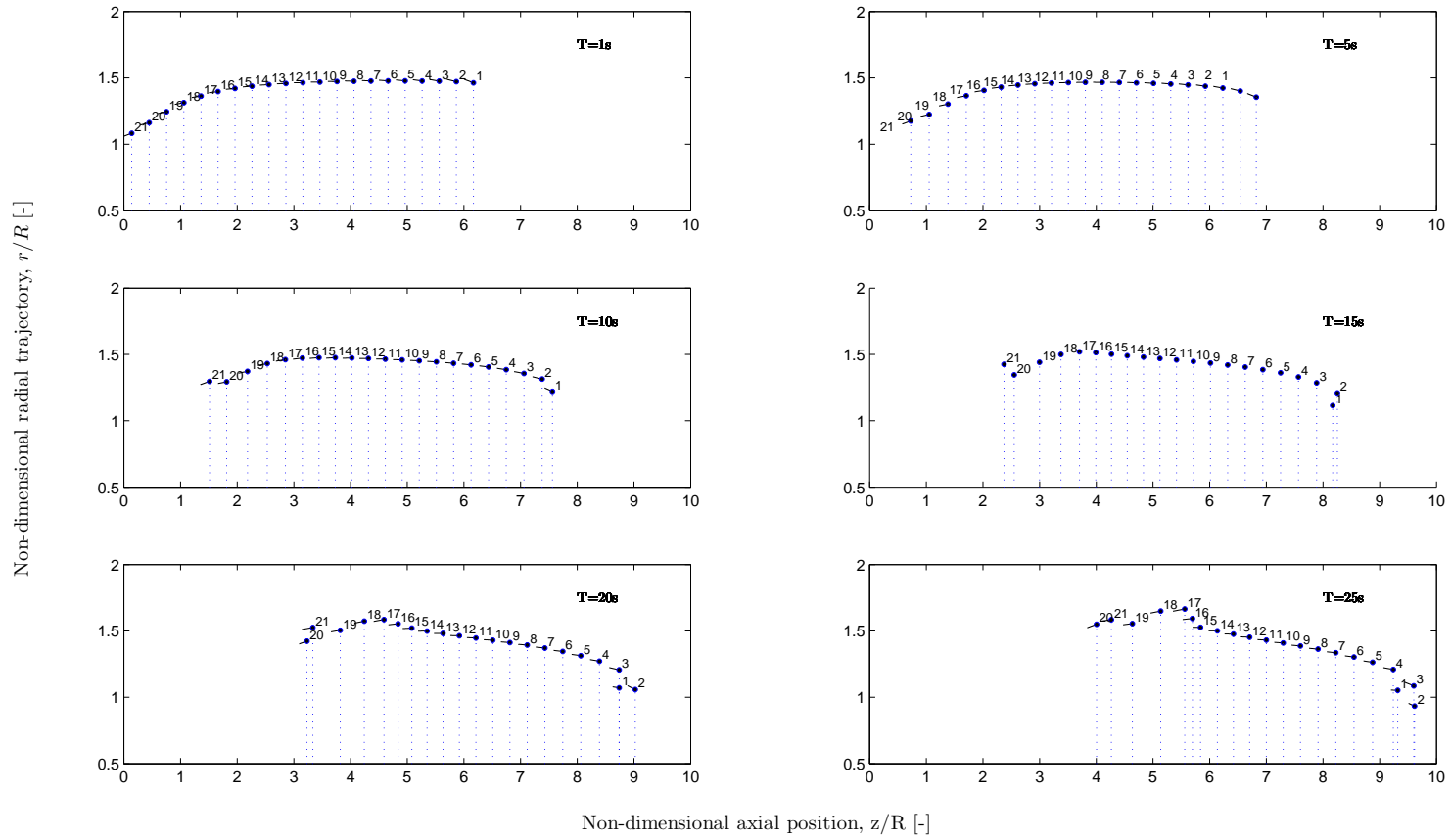


Figure 6.3: Radial trajectory for an ideally expanded vortex ring array with $B = 3$; snapshots are shown at 5s intervals.

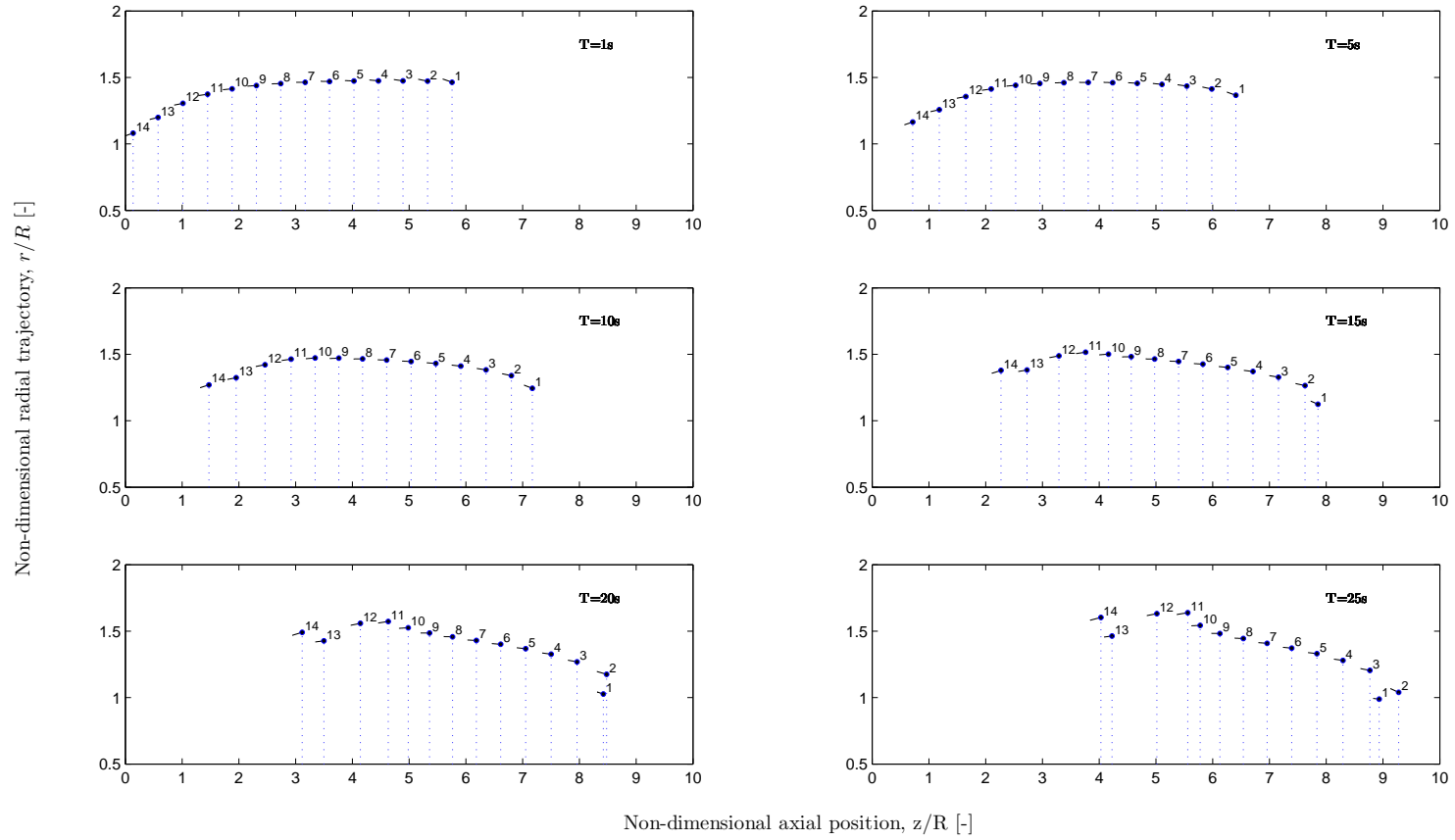


Figure 6.4: Radial trajectory for an ideally expanded vortex ring array with $B = 2$; snapshots are shown at $5s$ intervals.

6.3 Leapfrogging

The insights provided thus far have indicated the importance of the wake pitch and relative strength of the wake elements, for the overall development and behaviour of the wake. Recall the theoretical and experimental evidence of the instability modes of the helical rotor wake, as described Chapter 2, where evidence was presented for instabilities in marine propellers [12, 7], helicopter [14] and wind turbine wakes [13, 25, 23].

This observation of the tip vortex mutual interaction mode is in principle similar to the leapfrogging behaviour of the vortex rings where the nature of the instability mode is periodic. This draws comparisons with the evidence given in Medici and Alfredsson [2] of the low periodic frequency signal, whilst measuring the 3D velocity components in the wake of a model turbine, which the authors attribute to a process similar to vortex shedding behind bluff bodies and, in particular, solid disks.

In light of the uniqueness of their results and the considered periodic dynamics of interaction vortex rings, it is here hypothesized that the mutual interaction of vortex ring elements which come into close proximity may contribute to this observed periodic behaviour.

Medici et al. [2] define the Strouhal number St in order to examine characteristic signal frequencies:

$$St = \frac{fD}{U_\infty} \quad (6.2)$$

where D was their rotor diameter and U_∞ is the freestream velocity (0.18m and 8.3m/s). The same definition is used in the present study to facilitate the comparison.

For this study, two identical vortex rings (designated *Ring 1* and *Ring 2*) are defined in space, separated by the pitch h . An interaction study is subsequently performed by considering the mutual and self induced effects of the vortex rings to predict their radial and axial trajectories, which would enable identification of the characteristic frequency of the arrangement. As outlined in Chapter 5, the prevalent parameters governing mutual interactions are

1. the relative ring radii, R_1/R_2
2. the relative ring strengths, Γ_1/Γ_2
3. the linear pitch of the vortex rings, $h = z_1 - z_2$

Using the results in [2] for the case of axial flow, it was required to deduce the above listed parameters from the data provided from their work. The following simple relations were defined in order to formulate useful model inputs:

1. the two-bladed model turbine used in this case had a radius of approximately 0.09m, and this was assigned as the equal ring radii
2. equations 4.27 and 4.28 were employed to estimate the strength of each ring, from knowledge of the operational tip speed ratio and the thrust coefficient

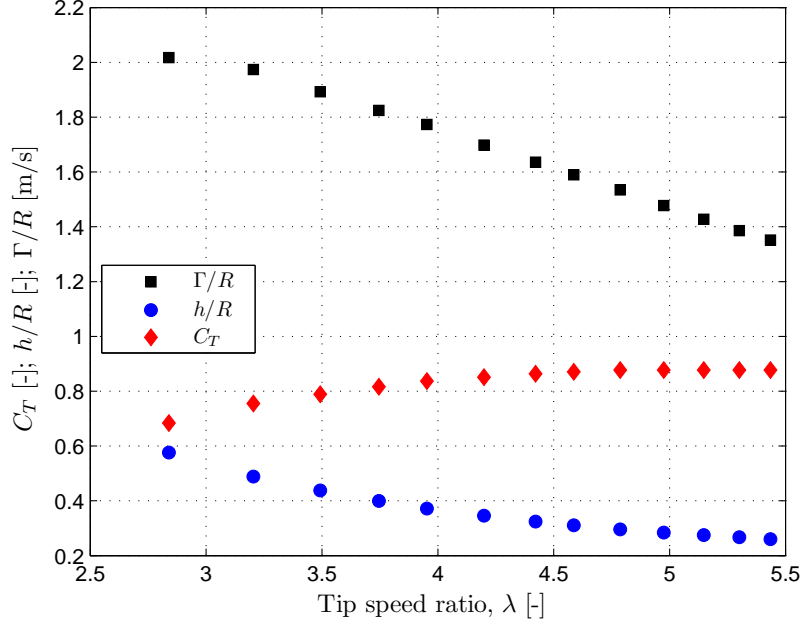


Figure 6.5: Pitch, strength and thrust simulation parameters extracted from [2]

3. The ring-to-ring pitch is estimated for a double-start helical wake system using the following approximation, similar to equation 6.1:

$$h/R \approx (1 - a_z) \cdot \frac{2\pi}{B\lambda}, \quad (6.3)$$

where a_z is an estimate for the average induction factor, estimated from simple momentum theory and knowledge of C_T .

The deduced inputs for the model are displayed in Figure 6.5, having extracted the data from Medici et al. [2].

For the desired dataset, $\lambda_{opt} = 3.66$ and $C_{T(opt)} = 0.794$. Extracting the data points presented in [2] corresponding to the salient tip speed ratio of $\lambda = 4.2$, the simplified analysis using equations 4.27, 4.28 and 6.3 yields $\Gamma/R = 2.53 \text{ m/s}$, $h/R = 0.52$ and $R = 0.09 \text{ m}$ as simulation inputs. The resulting temporal and spatial trajectories are displayed in Figure 6.7 and the comparison for the full set of data is shown in Figure 6.6.

Observing the temporal evolution of the rings, it is clearly seen that the period of oscillation of the ring radii is approximately 0.14 s , or 7.14 Hz . In terms of the non-dimensional St number, this corresponds to a value of 0.16 , compared with approximately $St = 0.15$ as reported in the benchmark data.

There is seeming agreement at this operating point between the two frequencies. However, the behaviour of St with tip speed ratio in both cases is completely opposite, suggesting that, despite the comparable magnitudes, there is no correlation between the dynamics of vortex ring interaction and the periodicity in the results of Medici et al. [2]. This can be explained by the fact that for higher tip speed ratio and thrust coefficient, a finer ring

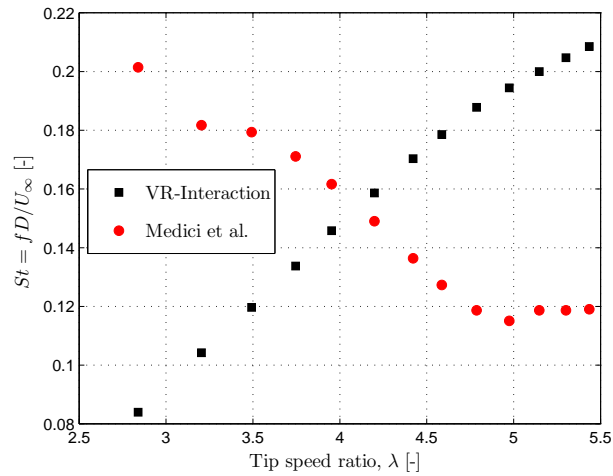
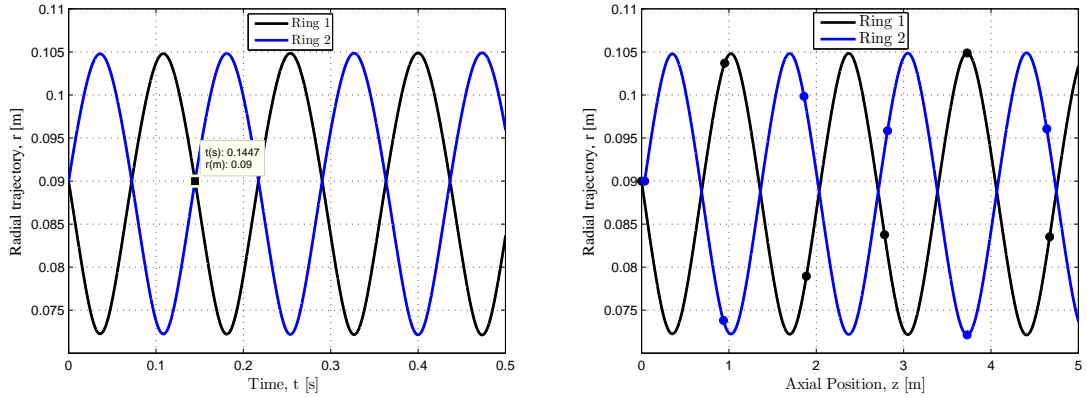


Figure 6.6: St as a function of tip speed ratio in axial flow, $U_\infty = 8.3m/s$

pitch is obtained, resulting overall in stronger interaction and a higher St . In a separate complementary study, shown in Figure 6.8, the leapfrogging frequency of two vortex rings is shown as a function of the strength and pitch for rings of $R = 0.09m$. An increase in the ring strength and a decrease in pitch results in altogether stronger interaction and higher frequencies. This strong dependence of the interaction on the filament spacing is also visually confirmed in the detailed analysis of Felli et al. [7].



(a) Temporal evolution of VR-system trajectory (b) Spatial evolution of VR-system trajectory; circular markers (•) spaced at $\Delta t = 0.1s$ intervals.

Figure 6.7: Characteristic leapfrogging frequency obtained using data extracted from Medici and Alfredsson [2]

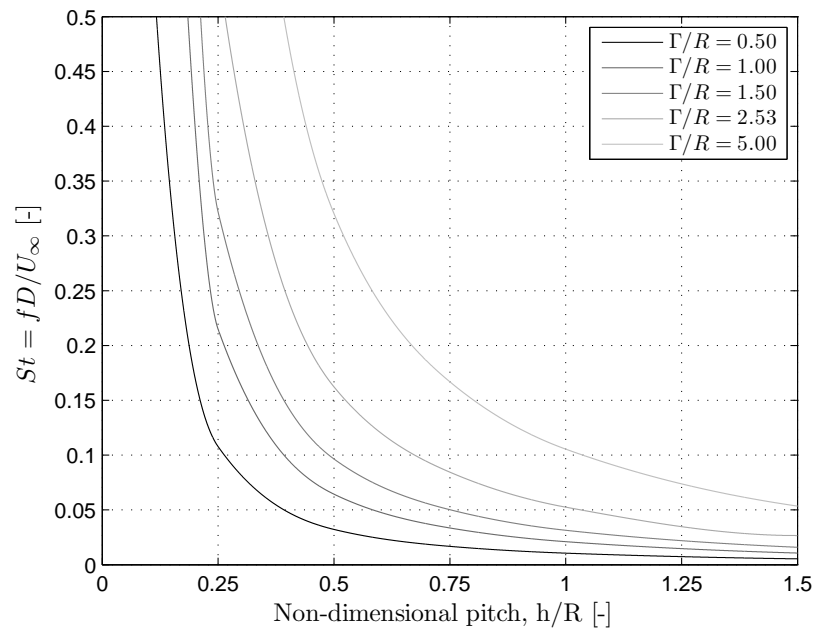


Figure 6.8: Leapfrog frequency as a function of pitch and strength

6.4 Free-Wake results

From the previous sections, it was shown that mutual-behaviour of vortex ring elements and the overall evolution of vortex ring arrays are particularly sensitive to the proximity of successive rings, as well as to the ring strength. An increase in both, leads to stronger interaction and a coupling action between successive rings is observed, after which the model becomes invalid since it is not able to simulate filament entanglement.

The Discrete FW-VRM was used for simulations of freely-convecting vortex rings to study the effects of inflow and ground effect instabilities on the evolution of the wake. The results presented in this section at most evaluated at the ideal operational thrust coefficient of $C_T = 8/9$. In general it was observed that close to this value, the simulated dynamic behaviour of the vortex rings became overly chaotic. Model limitations therefore constrain the interpretation of results at large thrust coefficient. The FW-VRM is limited in this sense, and some cases older wake rings "flipped" about their axes which does not reflect true physical behaviour (this is mainly due to the method of turning moment calculation in relation to the rotor frequency time stepping scheme).

Three wake development scenarios are presented with respect to the following different external conditions for thrust coefficient $C_T = \{0.32, 0.64, 0.89\}$:

- yawed flow, for a range of yaw angle $5^\circ < \Psi < 30^\circ$
- shear flow, for a range of the shear exponent $0.05 < m < 0.50$
- operation in ground effect, with relative hub heights, $1.4 < HH/R < 4.0$

6.4.1 Effects of yawed inflow

Lateral wake deflection is observed in the case of yawed inflow. Sample wake centreline trajectories are shown in Figure 6.9a. An increasing yaw angle causes a corresponding offset in the wake centreline, in the direction of the yawed wind direction. Interestingly, the model also predicts a degree of skewing in the wake, qualitatively shown in Figure 6.9b. The wake skew angle has been estimated between the rotor plane and a location $1D$ downstream. The wake induced velocity on the local flow causes the wake structure to veer towards the downwind side. This phenomenon has been widely observed in numerous wind tunnel experiments and numerical simulations (see for example the work of Sant [45] and Jimenez [36]).

6.4.2 Effects of a sheared inflow profile

In the presence of a sheared velocity profile, the higher wind speed in the upper section of the rotor gives rise to a downward curving rotation of the wake structure, in this case rotating the wake vortex rings in the $-\beta$ (see Figure 4.10) direction. Local effects due to the self-induced velocity however cause an overall upward shift of the wake structure. This is illustrated in Figure 6.11a, where the impact of stronger shear is also shown to cause a larger wake deflection. A stronger operating thrust coefficient also tends to increase the

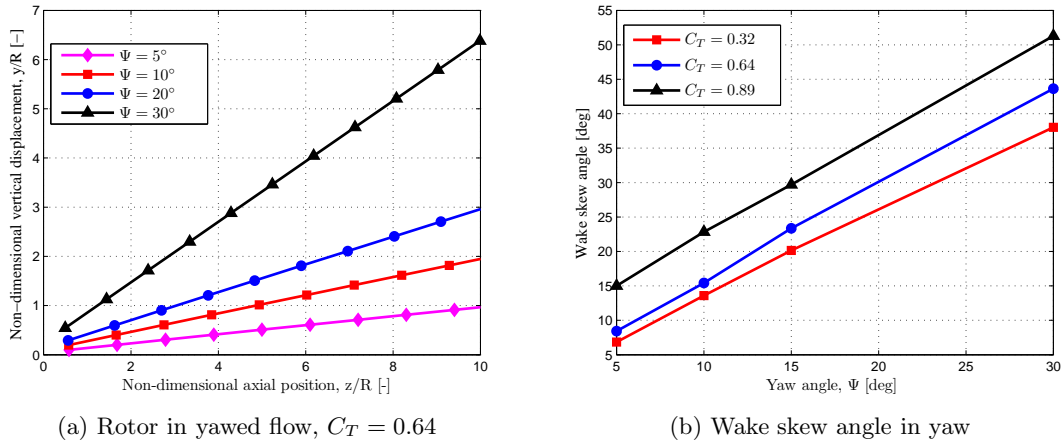


Figure 6.9: Wake development in sheared flow

deflection of the wake as shown in Figure 6.11b. These trends have been reported in a number of recent numerical studies (e.g. [32] and [9]).

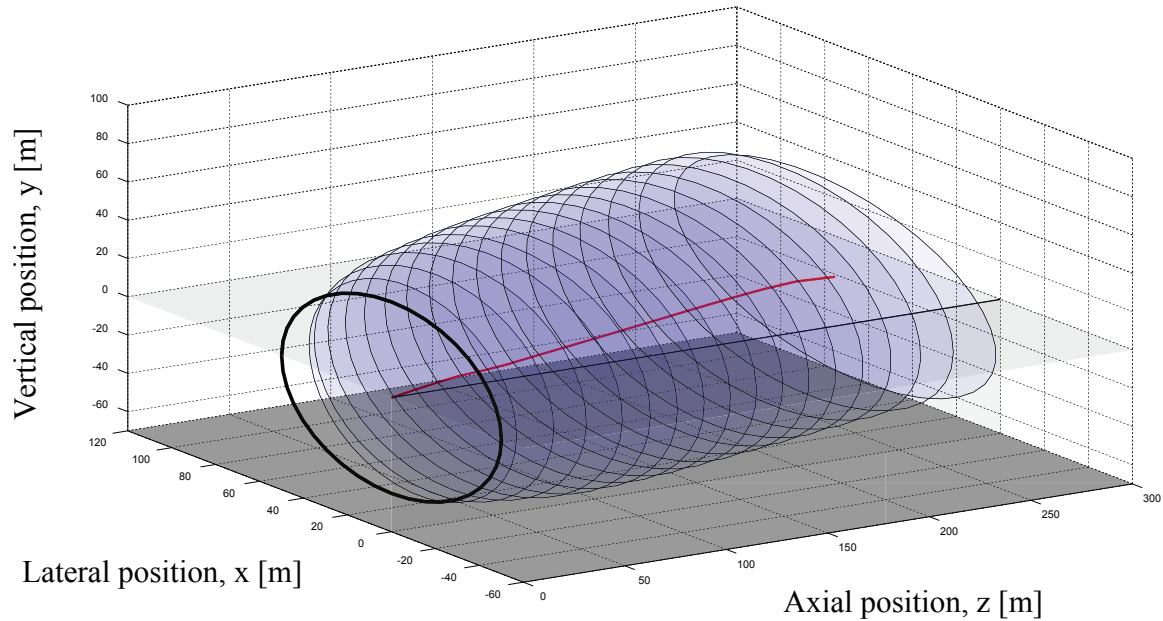
A combination of yawed and shear inflows has been illustrated in Figure 6.12, for an optimal thrust coefficient of $C_T = 0.889$.

6.4.3 Ground Effect

The proximity of the rotor wake and the ground, effectively augments the flow beneath the rotor and wake, in inverse relation with height above the ground plane (see Appendix E for detailed velocity contours). This would cause an upward curving rotation of the wake structure and the wake should tend to "lean" forward in the positive tilt direction ($+\beta$ direction in Figure 4.10). However, local vertical components of the vortex ring self-induced velocity come into play as the rings tilt. Hence the net effect is for the wake to tilt positively and shift downwards towards the ground. This downward shift in the wake structure has been observed experimentally ([46],[47]) as well as in numerical simulations ([48]) and is being attributed here to the self induction of the wake itself. In this manner of description, the mechanism by which the wake structure shifts downward when in ground effect is similar to the up-shifting behaviour observed in shear flow. These concepts are presented schematically in Table 6.3 and Figure 6.15.

The downshifting tendency can also be understood with reference to Grasso [9]. Recall that the latter presented results for the rotor wake in ground effect, where the lower portion of the wake was seen interact more strongly due to the effect of flow acceleration because of the ground. The relative tilt that would be implied within this observation suggests that indeed, the radial variations in pitch due to the ground would induce a short wave and long wave instability.

As expected, the down-shift imparted onto the wake gradually increases as the relative hub height decreases (Figure 6.14a). The down-shift is also more prominent for higher values of the thrust coefficient (Figure 6.14b). Thrust values above the optimum resulted in rather



(a) Isometric view

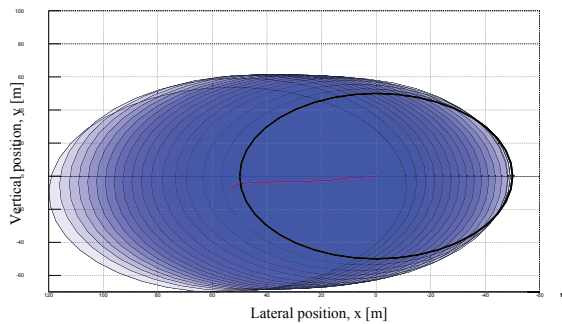
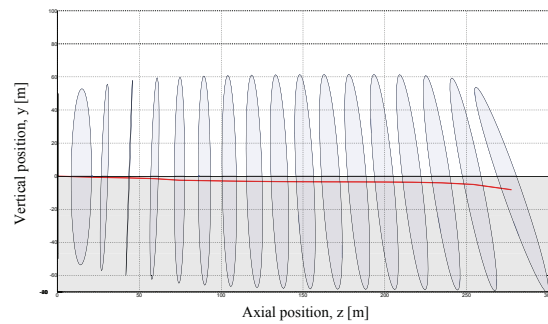
(b) Front view (xy plane)(c) Side view (yz plane)

Figure 6.10: Wake views: *red line* - wake centreline trajectory, *black line* - projection of rotor axis. $R = 50$, $R/HH = 1.4$, $\Psi = 10^\circ$, $C_T = 0.889$.

chaotic centreline trajectories as substantial vortex ring interaction led to unrealistic ring orientations and displacements.

Although these results are largely qualitative, it is good to place the observations within context. From a wind farm perspective, a $7D$ (or equivalently $14R$) spacing in the predominant wind direction is typical. From both Figures 6.14a and 6.14b, a fetch of approximately $10R$ is shown. As explained previously, the current model proved unreliable for larger distances due to rigorous vortex ring interactions.

For offshore wind turbines, the down-shifting effect could be expected to play a more prominent role in offshore wake aerodynamics since rotors are relatively closer to the ocean surface, compared with their respective onshore counterparts. The observed down-shifting behaviour would seem to imply that for offshore wind turbines, the rotor wakes

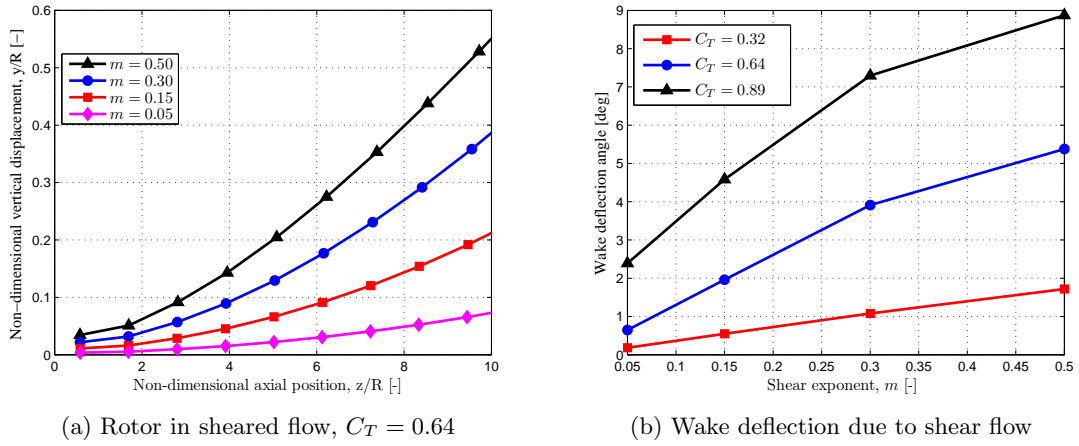


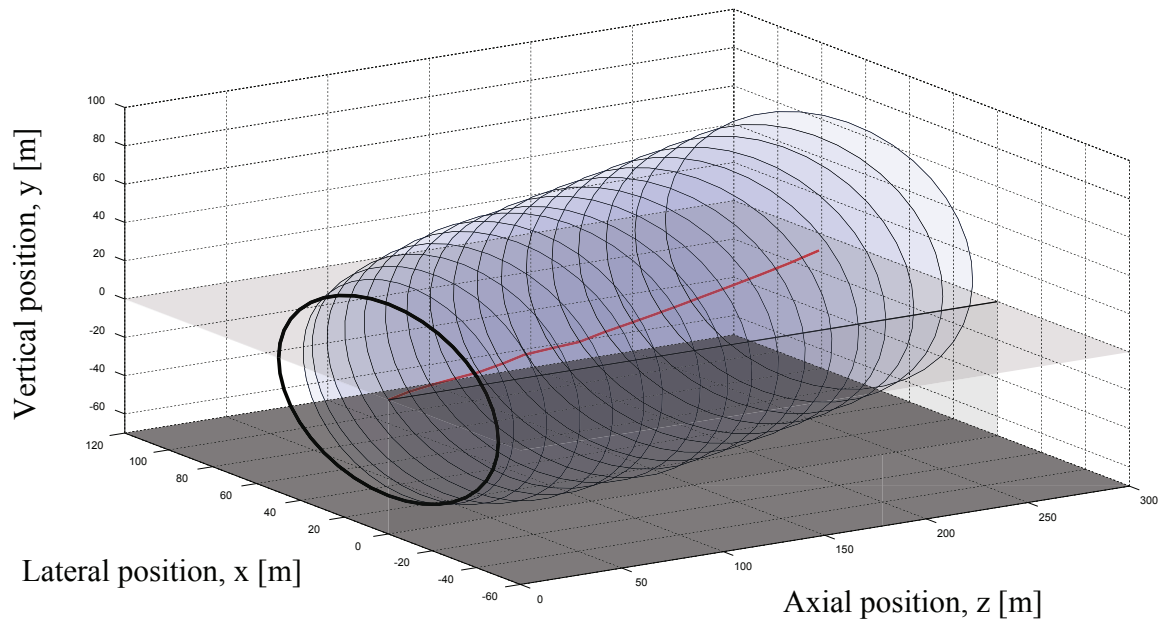


Figure 6.11: Wake development in sheared flow

could be expected to dissipate quicker due to increased interaction between the wake elements and between the wake and the ocean surface, resulting in lower overall wind farm losses.

Table 6.3: Schematic descriptors for Figures 6.15b and 6.15a

Figure symbol	Description
\rightarrow	Imposed velocity field
\leftarrow	Self-induced ring velocity decomposed into normal and
	Turning effect
	Sense of ring strength



(a) Isometric view

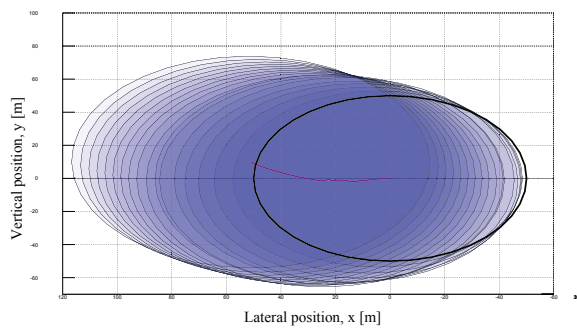
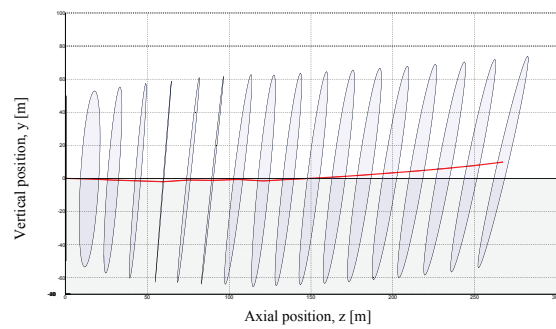
(b) Front view (yx plane)(c) Side view (yz plane)

Figure 6.12: Wake views: *red line* - wake centreline trajectory, *black line* - projection of rotor axis. $R = 50$, $R/HH = 1.4$, $m = 0.1$, $\Psi = 10^\circ$, $C_T = 0.889$.

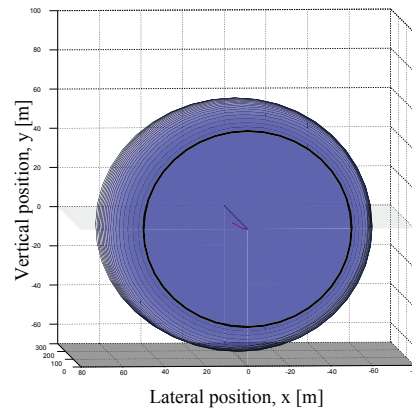
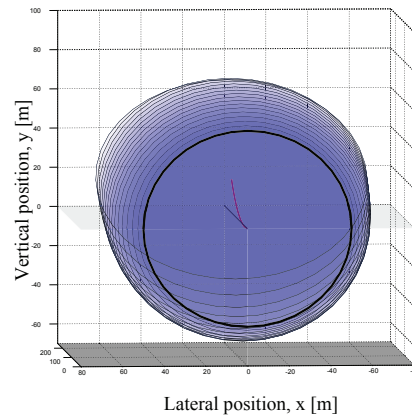
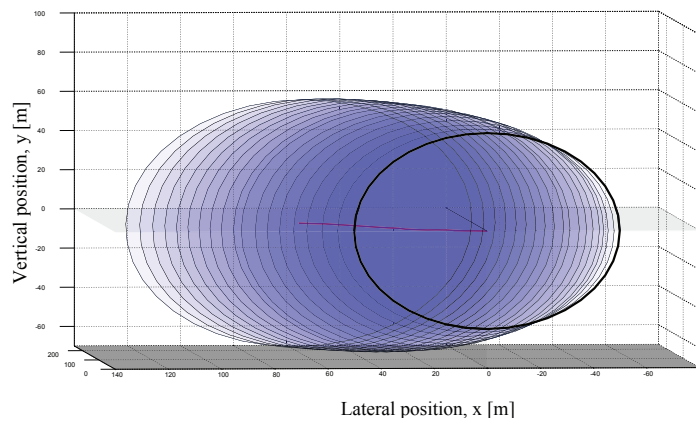
(a) Wake IGE, $HH/R = 1.4$ (b) Wake IGE and shear flow. $HH/R = 1.4$, $m = 0.15$ (c) Wake IGE and yawed flow. $HH/R = 1.4$, $\Psi = 15^\circ$

Figure 6.13: Frontal (xy plane) wake views for 6 revolutions: *red line* - wake centreline trajectory, *black line* - projection of rotor axis. $R = 50$, $R/HH = 1.4$, $C_T = 1.0$.

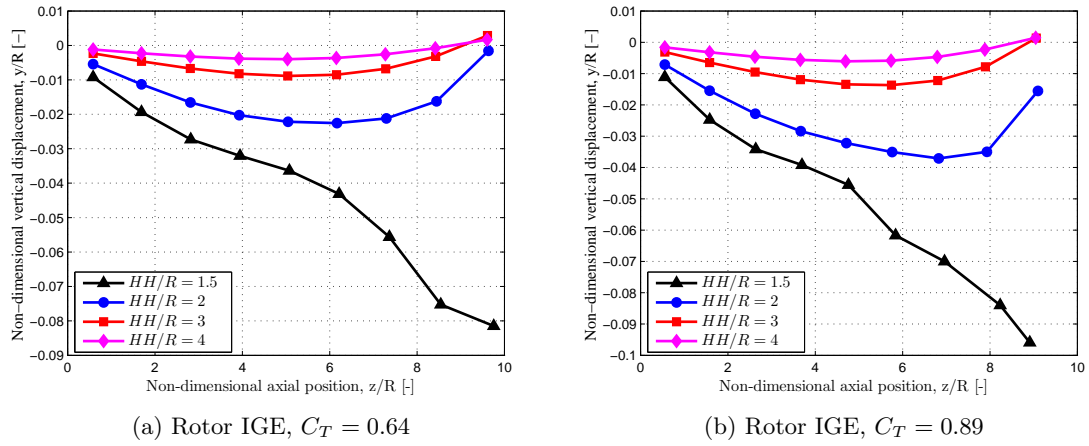


Figure 6.14: Rotor in ground effect

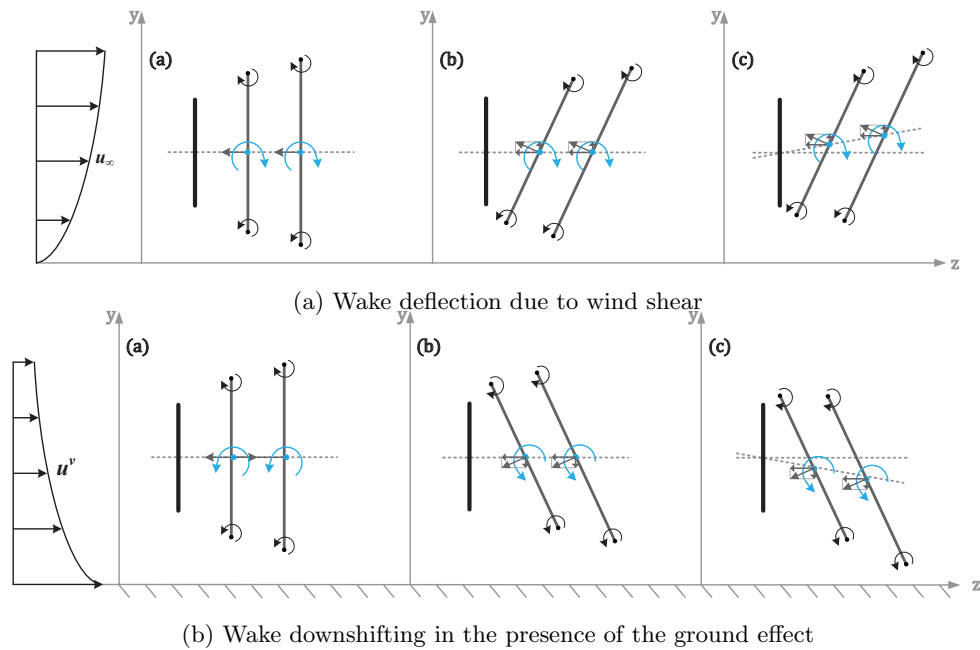


Figure 6.15: Illustrations of non-uniform wake evolution due to shear and ground effect

6.5 Detailed wake interactions

As described in Chapter 2, Widnall's theoretical model identified three possible wake instability modes. The short-wave mode is thought to occur due to the self-induced motion of helical filaments. In the current model however, a single helical wake revolution is collapsed onto a single vortex ring. Despite having taken into account the self induced axial motion of the ideal vortex rings, this motion is described by an axial velocity normal to the ring plane, acting at its centroid. Thus, short-wave modes cannot manifest in the current formulation. The mutual instability mode however can be captured using this model.

Felli et al. [7] observe that prior to the onset of the mutual inductance mode, radial pitch variations between adjacent helical structures were present. With the ring model, such radial variations can only be present insofar that adjacent vortex rings attain some relative orientation between one another. With a fully developed wake, this explained by the fact that the pitch perturbation causes a locally unbalanced velocity field.

In the wake simulations presented, this exact phenomenon cannot be fully observed since the rings are rigidly bound to the circular shape, with uniform strength. However, in the absence of any perturbations, it is seen that no leapfrogging action occurs. Drawing on the insights of Chapter 5 regarding the effect of velocity field compensation by adjacent rings, this result is expected.

It is additionally clear that in the initial phase of wake development, the radial expansion due to the momentum loss in the wake (modelled using axial vortex cylinder theory) is the dominating mechanism. It was shown that radial perturbations or imbalances in vortex ring arrays serve to augment the instability of the system. However the fact that during the initial phase of wake development the expansion process dominates implies that indeed, it might be expected that after the wake the streamlines have levelled out, interaction instabilities might be expected. This was observed in Felli et al. [7], where they define the onset of the instability as the region where the local streamtube gradient reaches 50% of the maximum streamtube slope. However, the cause-effect relation between the expansion of the streamtube and the onset of the instability is not clear. Their visualisations would suggest that prior to the onset of the mutual interaction mode, slight wake expansion can be observed. This is most likely due to the self-inductance of the propeller wake onto itself, where strong tip vortices close to the rotor plane set up an expanding radial field on the downstream wake region.

6.5.1 Instability in ground effect

Unfortunately, difficulties in modelling were encountered due to the starting effects, which were outlined in the last section of Chapter 4. After the initial domineering expansion region, the mutually induced effects come into play and as expected, the oldest wake ring (i.e. the first ring initiated in the simulation) experiences an particularly large contraction as a result of the upstream rings, which tend to reinforce each other's radial fields. Thus, the observed rapid shrinkage of the end rings which results ultimately in a reversal of flow is due to the starting effect. The onset of instabilities from this mechanism are thus not realistic.

Additionally, newly shed rings experience expansion due to the upstream rings, however in the developing wake model, the release of a new ring tends to stabilise the upstream ring and limits its expansion. The wake expansion due to the expanding cylinder theory dominates initially, but as this velocity contribution diminishes, the vortex rings generally start to experience contraction.

In general, in the absence of artificial flow perturbations, no mutual inductance effects were observed in preliminary simulations. The mutual induced velocity of adjacent rings in an expanded wake tend to stabilise the system, with the exception of the old wake rings, which as explained, experience an unrealistic contraction and flow reversal.

However, simulations in ground effect showed that the downshifting tendency of the wake centreline, and misalignment of vortex rings relative to one another, were enough to initiate trigger a mutual inductance mode, i.e. the observation that two or more vortex rings begin to interact. This is observed in panels (e) and (f) of Figure 6.16.

This would seem to indicate that, in accordance with the observation of Grasso [9], heightened wake interaction due to the augmented velocity profile in the lower portion of the wake could give rise to sufficient radial pitch variations in the helical wake structure, causing the onset of instabilities.

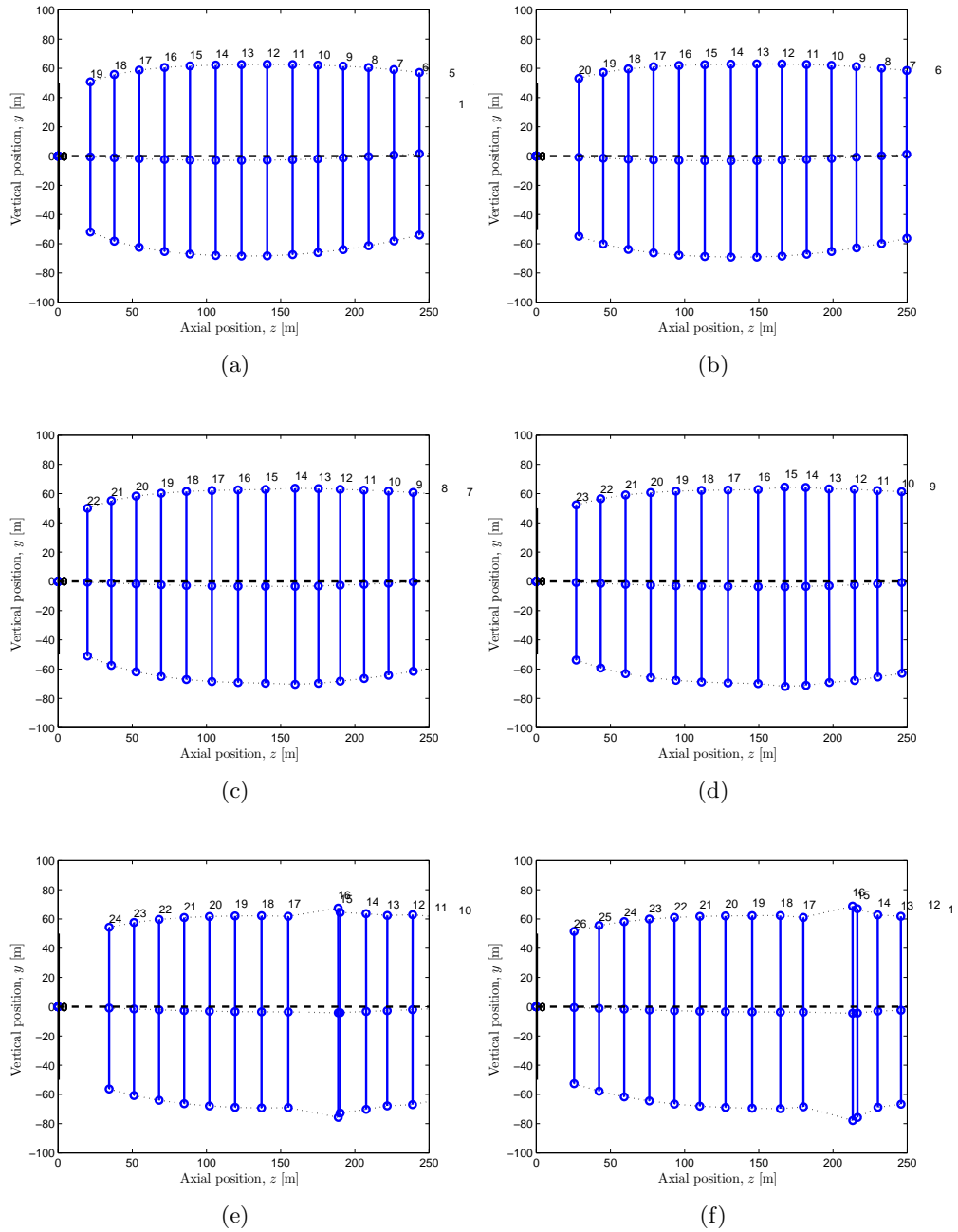


Figure 6.16: Snapshots of the development of the wake in ground effect, exhibiting the mutual inductance mode, resulting from the misalignment and interaction of respective wake elements. Panels (a) through (b) are equispaced in time by $3s$; $C_T = 0.889$, $HH/R = 1.5$.

Conclusions and recommendations

7.1 Conclusions

Key conclusions are drawn with respect to the stability of the wake, as well as the effectiveness of using vortex ring methods to model the wake.

Wake stability

- The simple FW-VRM described has been shown to correctly predict trends in the wake development of HAWTs. Wake skewing and tilting has been observed at different angles of yaw and in shear flow. For all angles of yaw tested, the wake skew angle was found to be consistently larger than the yaw angle, in accordance with theory and experimental evidence. Upward and downward shifts in the wake structure were observed in shear flow and operation in ground effect respectively. The simplicity of the model has allowed for a useful insight into the effect of the wake self-induction in response to externalities such as shear, yaw and the presence of the ground.
- The deflection of the wake in shear and yawed flow, and the downward shift in the presence of the ground presents an opportunity for controlling the wake trajectory. A unique field test on the potential of yaw misalignment for wake control was conducted by ECN which in fact holds a patent on the topic [49]. Their goal was to characterise the displacement of the wake, by measuring the velocity deficits behind the turbine in order to define the wake region. Their efforts were however inconclusive since the extent of wake deflection lay within the range of experimental uncertainty, and thus no conclusions could be drawn with confidence.
- The effect of the ground on the development of the wake and instabilities is seen to not only downshift the wake, but perhaps more importantly, it gives rise to interactions between adjacent vortex rings. In light of the sensitivity of the stable

development of the wake, this could be seen to affect the onset of intrinsic wake instabilities.

- Vortex filament interactions have been addressed mainly in relation to the periodic velocity signals reported in Medici et al. [2]. Although comparable in magnitude, no correlation was found between the vortex shedding frequency proposed in [2] and the interaction frequency of vortex rings. Wake interaction has however been observed experimentally in propeller wakes and this study has illustrated that in normal wind turbine operating conditions, mutual interaction is indeed possible. This points towards the possible role mutual interaction plays in the evolution of the transitional wake region and the need to experimentally investigate this phenomenon further.
- The role of atmospheric turbulence on the meandering of a wind turbine wake may likely be the single most influential factor determining the *transport* of a wind turbine wake. However, through simple means it has been shown that additional external factors can indeed *trigger* destabilising mechanisms within the wake.

Vortex ring modelling

Fundamental to the work conducted in this thesis was the use of the ideal vortex rings.

- Despite the simplicity of FW-VRM, it has been demonstrated that the use of these fluid elements can be beneficial for offering insights into complex physical flow phenomena. Simple engineering models, based on simplified physical models are gaining popularity in the wind energy research community, due to their simple but insightful nature (see Chapter 3).
- From the experience gained with the use of a ring model, it appears beneficial to extend it's use to rotor performance modelling. This is especially true in the cases of yaw and sheared flow, since the commonly used Blade Element Momentum method generally relies on empirical corrections to deal with non-axial flow conditions. The simple wake representation using vortex rings allows the description of a wake in non-uniform conditions in a simplified manner, and could potentially provide a better prediction for the rotor inflow velocities and performance.

7.2 Recommendations

Wake stability

- Due to time constraints, the full implementation of the combined FW-VRM interaction model could not be attained. The latest results presented at the end of Chapter 6 indicated that in ground effect, the rings were sufficiently perturbed, such that the mutual-inductance instability appeared in the wake vortex rings, at a location approximately. It could therefore be interesting to continue refining the model, in order to obtain further insights into the effects of shear, and prescribed turbulence on the triggering of these instability modes of vortex ring wake models.

- A detailed wake experiment is envisioned, similar to the one presented in Felli et al. [7], on a wind turbine rotor. Despite similarities between the wakes of propellers and wind turbines, one variable that could play a role in the visualisations is the relative blockage ratio presented by the hub. Furthermore, it would be interesting to study the influence of shear on the evolution of the tip vortices. As explained for the case of an inclined vortex ring, the mutual interaction mode is rather sensitive to misalignment in the adjacent vortex filaments. It can therefore be expected that with a sheared velocity profile, filament entanglement would occur more readily, leading to quicker transition to turbulence. The relation between the number of turbine blades and wake stability could furthermore be incorporated into such a study; this pertains mainly to two- and three-bladed rotors, where the former could potentially be favoured for use in far shore wind farms.
- A further experiment is proposed with the aim of validating the wake in ground effect observations presented in this thesis. Vortex ring tilting corresponds with numerical simulations of Grasso [9] and Madsen et al. [9]. It would therefore be interesting to obtain wake visualisations of a model rotor in ground effect, at different hub heights and operating states. Given the strong dependence of wake stability on the relative filament spacing, the appearance of a self-induced and mutual inductance instability mode becomes more likely. This study would therefore serve to validate work performed so far on wakes in ground effect, and also to clarify the observations of Crespo et al. [48].

Vortex ring models

- One unexplored strength of the FW-VRM is its potential as a *rotor performance and analysis tool*. An extension to the current method would be to additionally represent wake vorticity using a root vortex ring, as well as a number of intermediary rings between the root and tip vortex rings so as to model a rotor with a non-uniformly distributed load. It could therefore be an interesting exercise to compare the current simplified free wake model with results obtained from more complex numerical simulations. The capability of handling non-uniform flows presents an opportunity of complementing or altogether replacing BEM models in non-axial flow regimes.
- An emerging concept is that of *Active Wake Control*. Knowledge of wake development is not only better understood, it has also been proposed to actively exploit off-axis wake development, such as wake skewing because of yawed inflow, to actively "drive" turbine wakes according to a certain desired trajectory. Despite the known loss of power and increased turbine loading resulting from yawed operation, it is thought that actively yawing turbines can lead to a net positive effect on the total energy capture of the wind farm.

The present FW-VRM could be adapted for such a simulation, giving some indication of the extent and practicality of wake *avoidance* within a wind farm. In contrast to complex numerical wind farm simulations, applying the FW-VRM could provide a quick overview of possible control strategies and wind farm layouts to optimize the energy capture.

References

- [1] G.C. Larsen, H.A. Madsen, F. Bingöl, J. Mann, S. Ott, J.N. Sørensen, V. Okulov, N. Troldborg, M. Nielsen, K. Thomsen, T.J. Larsen, and R. Mikkelsen. Dynamic wake meandering modeling. Technical Report Risø-R-1607(EN), Risø National Laboratory: Roskilde, 2007.
- [2] D. Medici and P.H. Alfredsson. Measurements on a wind turbine wake: 3d effects and bluff body vortex shedding. *Wind Energy*, 9(3):219–236, 2006.
- [3] V.V. Meleshko. Coaxial axisymmetric vortex rings: 150 years after helmholtz. *Theoretical and Computational Fluid Dynamics*, 24:403–431, 2010.
- [4] Global Wind Energy Council. Global wind report: Annual market update 2011. Technical report, GWEC, 2012.
- [5] J. Sørensen and V. Okulov. Modeling of the far wake behind a wind turbine. In Joachim Peinke, Peter Schaumann, and Stephan Barth, editors, *Wind Energy*, pages 245–248. Springer Berlin Heidelberg, 2007.
- [6] M. Van Dyke. *An Album of Fluid Motion*. The Parabolic Press, Stanford, California, 1982.
- [7] M. Felli, R. Camussi, and F. di Felice. Mechanisms of evolution of the propeller wake in the transition and far field. *Journal of Fluid Mechanics*, 682:5–53, 2011.
- [8] S. Øye. A simple vortex model of a wind turbine rotor. *Proceedings third IEA Symposium on the Aerodynamics of Wind Turbines, ETSU*, Harwell, Didcot, UK, 1989.
- [9] F. Grasso. Awsm ground and wind shear effects in aerodynamic calculations. Technical Report ECN-E-10-016, ECN, 2010.
- [10] H.A. Madsen, V. Riziotis, F. Zahle, M.O.L. Hansen, H. Snel, F. Grasso, T.J. Larsen, E. Politis, and F. Rasmussen. Blade element momentum modeling of inflow with shear in comparison with advanced model results. *Wind Energy*, 2011.

- [11] European Wind Energy Association. Pure power: Wind energy targets for 2020 and 2030. Technical report, EWEC, 2011.
- [12] M. Felli, R. Camussi, and G. Guj. Effect of the number of blades on propeller wake evolution. *Experiments in Fluids*, 4:409–418, 2008.
- [13] P. Alfredsson and J-A. Dahlberg. A preliminary wind tunnel study of windwall wake dispersion in various flow conditions. Technical Report Technical Note AU-1499 Part 7, Swedish Defence Research Agency, Stockholm Sweden, 1979.
- [14] J. Stack and F.X. and Caradonna. Flow visualizations and extended thrust time histories of rotor vortex wakes in descent. In *AHS 4th Decennial Specialists' Conference on Aeromechanics*, 2004.
- [15] G. España, S. Aubrun, and P. Devinant. Is the meandering of a wind turbine wake due to atmospheric length scales? In Joachim Peinke, Martin Oberlack, and Alessandro Talamelli, editors, *Progress in Turbulence III*, volume 131 of *Springer Proceedings in Physics*, pages 91–94. Springer Berlin Heidelberg, 2009.
- [16] G. España, S. Aubrun, S. Loyer, and P. Devinant. Spatial study of the wake meandering using modelled wind turbines in a wind tunnel. *Wind Energy*, 14(7):923–937, 2011.
- [17] G. España, S. Aubrun, S. Loyer, and P. Devinant. Wind tunnel study of the wake meandering downstream of a modelled wind turbine as an effect of large scale turbulent eddies. *Journal of Wind Engineering and Industrial Aerodynamics*, 101:24–33, 2012.
- [18] J. Whale, C.G. Anderson, R. Bareiss, and S. Wagner. An experimental and numerical study of the vortex structure in the wake of a wind turbine. *Journal of Wind Engineering and Industrial Aerodynamics*, 84:1–21, 2000.
- [19] F. Bingöl, G.C. Larsen, and J. Mann. Wake meandering - an analysis of instantaneous 2d laser measurements. In *The Science of Making Torque from Wind*, 75, 2007.
- [20] G. Hassan. Dynamic loads in wind farms ii - final report joule project. Technical Report JOU2-CT92-0094, 1996.
- [21] S.E. Widnall. The stability of a helical vortex filament. *Journal of Fluid Mechanics*, 54:641–663, 1972.
- [22] H. Levy and A.G. Forsdyke. The stability of an infinite system of circular vortices. *Proceedings of the Royal Society of London. Series A, Containing Papers of a Mathematical and Physical Character No. 768*, 114(768):594–604, 1927.
- [23] S. Ivanell, R. Mikkelsen, J.N. Sørensen, and D. Henningson. Stability analysis of the tip vortices of a wind turbine. *Wind Energy*, 2010.
- [24] V.L. Okulov. On the stability of multiple helical vortices. *Journal of Fluid Mechanics*, 521:319–342, 2004.

- [25] M. Sherry, J. Sheridan, and D. 3 Lo Jacono. Horizontal axis wind turbine tip and root vortex measurements. In *15th Int Symp on Applications of Laser Techniques to Fluid Mechanics*, Lisbon, Portugal, 2010.
- [26] M.J. Stock. Summary of vortex methods literature (a living document rife with opinion), 2007.
- [27] J. D. Anderson. *Fundamentals of Aerodynamics*. McGraw-Hill, 5th edition, 2005.
- [28] W.R.M. van Hoydonck, R.J.J. Bakker, and M.J.L. Tooren. A new method for rotor wake analysis using non-uniform rational b-spline primitives. Technical Report NLR-TP-2010-465, National Aerospace Laboratory NLR, 2010.
- [29] G. H. Xu and S. J. Newman. A full-span free-wake model using circular-arc vortex elements and incorporating rotor trim analysis. *Journal of Aerospace Engineering*, 220:145–153, 2006.
- [30] J.M. Stubblefield. Numerical-based ducted propeller design using vortex lattice lifting line theory. Master’s thesis, Massachusetts Institute of Technology, 2008.
- [31] S. Widnall. Potential flow calculations of axisymmetric ducted wind turbines. MIT, July 2009.
- [32] D. Micallef, C.J. Simao Ferreira, T. Sant, and G.J.W. van Bussel. An analytical model of wake deflection due to shear flow. In *the proceedings of conference Torque 2010, the science of making torque from wind.*, 2010.
- [33] B. Sanderse, S. P. Van der Pijl, and B. Koren. Review of computational fluid dynamics for wind turbine wake aerodynamics. *Wind Energy*, 14:799819, 2011.
- [34] H. Lu and F. Porte-Agel. Large-eddy simulation of a very large wind farm in a stable atmospheric boundary layer. *Physics of Fluids*, 23, 065101, 2011.
- [35] S.P. van der Pijl and J.G. Schepers. Improvements of the wakefarm wake model. In *Presented at the Workshop on wake modelling and benchmarking of models of Annex XXIII (Offshore Wind Energy Technology Deployment) of IEA Wind, Denmark*, 2006.
- [36] A. Jimenez, A. Crespo, and E. Migoya. Application of a les technique to characterize the wake deflection of a wind turbine in yaw. *Wind Energy*, 13:559–572, 2010.
- [37] M. Abramowitz and I.A. Stegun. *Handbook of Mathematical Functions*. Dover Publications, 1965.
- [38] B. Montgomerie. A contribution to wind turbine wake dynamics algorithms. In *Wake Conference June 8-9*, Gotland University, Visby, Sweden, 2011.
- [39] L.E. Fraenkel. On steady vortex rings with small cross-section in an ideal fluid. *Proceedings of the Royal Society of London*, A316:29–62, 1970.
- [40] Jie-Zhi Wu, Hui-Yang Ma, and Ming-De Zhou. *Vorticity and vortex dynamics*. Springer, 2006.

-
- [41] G.H. Vatistas, V. Kozel, and W.C. Mih. A simpler model for concentrated vortices. *Experiments in Fluids*, 11(1):73–76, 1991.
- [42] R.E. Wilson. Wind turbine flow field model. *J. ASME*, 108:344–345, 1986.
- [43] Wayne Johnson. *Helicopter Theory*. Princeton University Press, 1980.
- [44] T.T. Lim. A note on the leapfrogging between two coaxial vortex rings at low reynolds numbers. *Physics of Fluids*, 9:239, 1997.
- [45] T. Sant. *Improving BEM-based Aerodynamic Models in Wind Turbine Design Codes*. PhD thesis, University of Malta and Delft University of Technology, 2007.
- [46] A. M. Talmon. The wake of a horizontal axis wind turbine model, measurements in uniform approach flow and in a simulated boundary layer. Technical Report Report 85-01021, TNO Division of Technology for Society, 1985.
- [47] A. M. Talmon. A wind tunnel investigation into the effects of tower and nacelle on wind turbine wake flow. Technical Report Report 84-08479, TNO Division of Technology for Society, 1984.
- [48] A. Crespo, J. Hernández, E. Fraga, and C. Andreu. Experimental validation of the upm computer code to calculate wind turbine wakes and comparison with other models. *J. Wind Eng. Ind. Aerodynamics*, 27:77–88, 1988.
- [49] G.P. Corten, K. Lindenburg, and P. Schaak. Assembly of energy flow collectors, such as windpark, and method of operation.

Appendix A

Governing Equations

In this chapter, the main governing equations describing the flow are described from first principles.

For an incompressible fluid, continuity is given by

$$\nabla \cdot \mathbf{u} = 0 \quad (\text{A.1})$$

where the velocity field may be expressed in terms of the velocity potential, such that

$$\mathbf{u} = \nabla \times \phi \quad (\text{A.2})$$

where ϕ is the velocity potential and is a function of spatial coordinates.

We also know that for an irrotational flow, the vorticity can be expressed as the curl of the velocity field,

$$\boldsymbol{\omega} = \nabla \times \mathbf{u} = 0 \quad (\text{A.3})$$

Substituting eqn. [A.2](#) in eqn. [A.3](#),

$$\boldsymbol{\omega} = \nabla(\nabla \cdot \phi) - \nabla^2 \phi = 0 \quad (\text{A.4})$$

Since ϕ is indeterminate to the extent of a gradient, it is possible to express the vector velocity potential as

$$\boldsymbol{\omega} = -\nabla^2 \phi = 0 \quad (\text{A.5})$$

It was shown in Saffman that the stream function for the axisymmetric circular line vortex system with a uniform vorticity distribution (or thin vortex ring) can be written as,

$$\psi = \frac{\Gamma}{4\pi}(rR_i) \int_0^{2\pi} \frac{\cos(\theta - \theta_i)}{|\mathbf{r} - \mathbf{r}_i|} d(\theta - \theta_i) \quad (\text{A.6})$$

implying that the velocity potential $\phi = (0, \psi/r, 0)$. This satisfies the Poisson equation A.5.

The direction vector between a point on the thin ring and an arbitrary point in space is

$$\begin{aligned} |\mathbf{r} - \mathbf{r}_i| &= [(z - z_i)^2 + r_i^2 R^2 - 2r_i R \cos(\theta - \theta_i)]^{0.5} \\ &= [A + B \sin(\theta_i)]^{0.5} \end{aligned}$$

A.0.1 Closed form induced velocity expressions

The Biot-Savart form of the velocity expression is then obtained in the following manner:

$$\begin{aligned} \mathbf{u} &= \nabla \times \left(\frac{1}{R_i} \psi \hat{e}_{\theta_i} \right) \\ &= \nabla \times \left(\frac{\Gamma}{4\pi} R_i \int_0^{2\pi} \frac{-\sin(\theta_i)}{|\mathbf{r} - \mathbf{r}_i|} d\theta_i \hat{e}_{\theta_i} \right) \\ &= \frac{\Gamma}{4\pi} R_i \int_0^{2\pi} \frac{R_i - r \sin(\theta_i)}{|\mathbf{r} - \mathbf{r}_i|^3} d\theta_i \hat{e}_z + \frac{\Gamma}{4\pi} R_i \int_0^{2\pi} \frac{(z - z_i) \sin(\theta_i)}{|\mathbf{r} - \mathbf{r}_i|^3} d\theta_i \hat{e}_r \quad (\text{A.7}) \end{aligned}$$

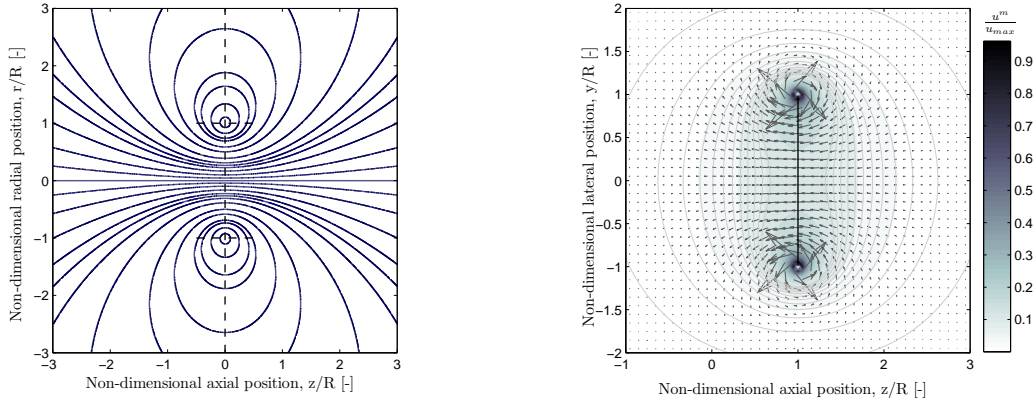
$$u_z = \frac{\Gamma}{4\pi} R_i \left[\left(R_i + r \frac{A}{B} \right) I_2 - \frac{r}{B} I_1 \right] \quad (\text{A.8})$$

$$u_r = \frac{\Gamma}{4\pi} R_i \left(\frac{z - z_i}{B} \right) [I_1 - I_2] \quad (\text{A.9})$$

where $I_1 = \frac{4}{a} K(m)$ and $I_2 = \frac{4}{a^3} \frac{E(m)}{(1-m)}$

where $K(m)$ and $E(m)$ are complete elliptic-type integrals of the first and second kind. The argument m is called the elliptic parameter and is a function of the relative spacing between the ring centre and the evaluation point.

$$m = \frac{4rR_i}{[(z - z_i)^2 + (r + R_i)^2]} \quad (\text{A.10})$$



(a) Flow streamlines in a meridional plane arising due to an ideal vortex ring in an unbounded domain

(b) Actual IVR array contribution

Figure A.1: Flow field of an ideal vortex ring

A.0.2 Closed form solution of the stream function

It is useful to evaluate the stream function in closed form for understanding the flow field for the vortex ring elements to be studied. First, let $\Theta = \theta - \theta_i$. Then, from A.6,

$$\begin{aligned} \int_0^{2\pi} \frac{\cos(\Theta)}{|\mathbf{r} - \mathbf{r}_i|} d\Theta &= \frac{1}{rR_i} \int_0^\pi \left[\left(\frac{2}{\sqrt{m}} - \sqrt{m} \right) \left(1 - m \cos^2 \frac{\Theta}{2} \right)^{-0.5} - \right. \\ &\quad \left. \frac{2}{\sqrt{m}} \left(1 - m \cos^2 \frac{\Theta}{2} \right)^{0.5} \right] d\Theta \\ &= \frac{2}{\sqrt{rR_i}} \left[\left(\frac{2}{\sqrt{m}} - \sqrt{m} \right) K(m) - \frac{2}{\sqrt{m}} E(m) \right] \end{aligned}$$

noting that $\theta = \pi/2$ due to axisymmetry.

Therefore the closed form of the stream function is given by

$$\psi = \frac{\Gamma}{4\pi} \sqrt{rR_i} \left[\left(\frac{2}{\sqrt{m}} - \sqrt{m} \right) K(m) - \frac{2}{\sqrt{m}} E(m) \right] \quad (\text{A.11})$$

A.0.3 Elliptic Integrals

The correct treatment of these special functions is of paramount importance given that the closed form solutions which are adopted, depend on the evaluation of the elliptic integrals.

Matlab conveniently has these functions available in the built-in library. The evaluation method follows that of the arithmetic geometric mean implemented and validated by [37]. The integrals evaluated by this method are highly accurate, and a reasonable compromise between accuracy and computation time is found at a tolerance level of around 1×10^{-20} .

We are interested in the complete form of the Legendre elliptic integral, which means that the upper limit of the integral (the Jacobi amplitude) is set to it's highest value of $\pi/2$

These integrals are normally readily defined in terms of the elliptic modulus, k , as follows:

$$K(k) = \int_0^{\pi/2} \frac{d\Theta}{\sqrt{[1 - k^2 \sin^2 \Theta]}} \quad (\text{A.12})$$

$$E(k) = \int_0^{\pi/2} \sqrt{[1 - k^2 \sin^2 \Theta]} d\Theta \quad (\text{A.13})$$

The function retrieves the complete integral values based on the input argument. It is important to note here that the way these are defined in the software requires that the *parameter* is provided. Other forms replace the parameter with the elliptic modulus k (used as shown in eqns. A.12 and A.13) or the modular angle, α . These are related as follows:

$$0 \leq \{k^2 = m = \sin^2 \alpha\} \leq 1 \quad (\text{A.14})$$

For use of the in built Matlab library, the parameter must be used as the input argument. This manifests itself as follows. With reference to eqns. A.12 and A.13, let $s = \sin \Theta$. Therefore, $ds = \cos \Theta \cdot d\Theta$. Therefore, the elliptic integrals may alternatively be expressed as,

$$K(m) = \int_0^1 \frac{ds}{\sqrt{[(1 - s^2)(1 - ms^2)]}} \quad (\text{A.15})$$

$$E(m) = \int_0^1 \frac{\sqrt{[1 - ms^2]}}{\sqrt{[1 - s^2]}} ds \quad (\text{A.16})$$

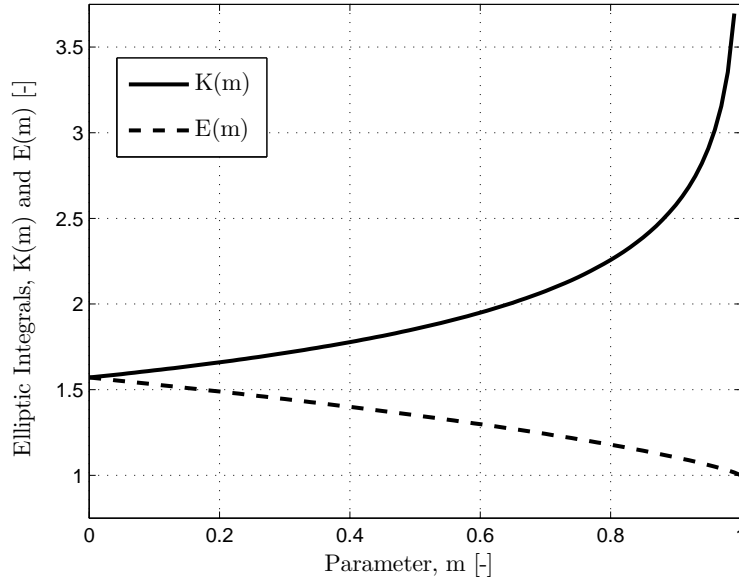


Figure A.2: Complete elliptic integral characteristics, as a function of the parameter m

A.1 Coordinate Systems

The equations for the induced velocities from a thin, axisymmetric vortex ring are defined in local cylindrical coordinates.

It is important to define beforehand an established set of well-defined coordinates which best describe the flow in the most simple manner. We are clearly interested in global as well as local ring coordinates. In summary:

- $\{X, Y, Z\}$ system: global Cartesian coordinate axes in which all velocities and displacement vectors are ultimately evaluated
- $\{x_r, y_r, z_r\}$ system: local vortex ring Cartesian coordinate axes
- $\{r, \theta, z\}$ system: local vortex ring cylindrical coordinate axes. z and z_r coincide for a ring in any orientation. These also coincide with Z for a vortex ring centered with β and χ equal to zero, i.e. no tilt or skew.

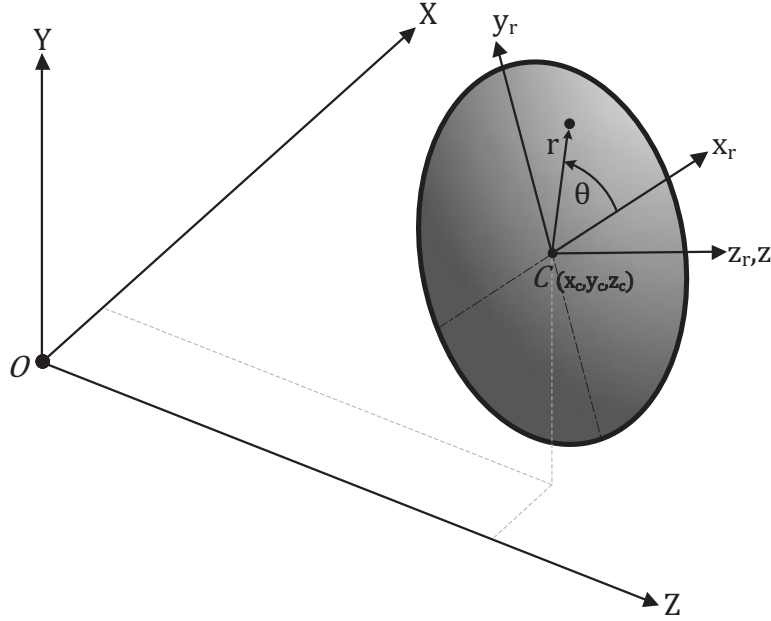


Figure A.3: Principal Coordinate Systems

A.2 Transformation matrices

$$\begin{pmatrix} x_r \\ y_r \\ z_r \end{pmatrix} = \begin{pmatrix} r \cdot \cos(\theta) \\ r \cdot \sin(\theta) \\ z \end{pmatrix} \quad (\text{A.17})$$

Considering the complete case, i.e. where the rings are both tilted *and* skewed, the calculation of the induced velocity becomes slightly more involved. The basic equations are the same, however, they give results relative to the ring plane.

The first step is to resolve the local x and y ring coordinates into the absolute coordinate system. The following transformation operates on the local coordinates to give the absolute $\{X, Y, Z\}$:

$$\begin{pmatrix} \cos(\chi) & -\sin(\beta) \sin(\chi) & 0 \\ 0 & \cos(\beta) & 0 \\ -\sin(\chi) & -\sin(\beta) \cos(\chi) & 0 \end{pmatrix} \quad (\text{A.18})$$

$$\begin{pmatrix} X \\ Y \\ Z \end{pmatrix} = C_\beta C_\chi \cdot \begin{pmatrix} x_r \\ y_r \\ z_r \end{pmatrix} + \begin{pmatrix} x_c \\ y_c \\ z_c \end{pmatrix} \quad (\text{A.19})$$

The self induced velocity of the ring vortex acts to propel the ring along its axis of symmetry. The self induced component is added to the mutually induced components. Thus the self induced velocity must be resolved into absolute coordinates. The following

matrices are defined for this purpose:

$$c_\beta = \begin{pmatrix} \cos(\beta) & 0 & 0 \\ 0 & \sin(\beta) & 0 \\ 0 & 0 & \cos(\beta) \end{pmatrix} \quad (\text{A.20})$$

$$c_\chi = \begin{pmatrix} \sin(\chi) & 0 & 0 \\ 0 & 1 & 0 \\ 0 & 0 & \cos(\chi) \end{pmatrix} \quad (\text{A.21})$$

$$\begin{pmatrix} v_x \\ v_y \\ v_z \end{pmatrix} = VELc_\beta c_\chi \quad (\text{A.22})$$

Appendix B

Expressions for an inclined vortex ring

B.0.1 Induced velocities at an arbitrary point from inclined ideal vortex rings

An important feature of the code developed is the simple method implemented for evaluating the induced velocities from the ideal vortex ring elements used. Studying the ideal equations derived for the induced velocities, it is clear that in axisymmetric form, the following geometric quantities are required:

1. the relative axial spacing between the evaluation point and the vortex ring plane
2. the radial distance between the evaluation point and the central axis through the vortex ring
3. the relative angular location of the evaluation point and the central ring axis

The equivalent point method was adopted to satisfy the above requirements and reference is made to Fig. B.1 on which this derivation is based. This method essentially entails a rotation of the vortex ring in consideration and the evaluation point (denoted as $C_1(z_1, y_1)$), about the ring centre (p_i, q_i) . The resulting situation is shown in the right schematic of Fig. B.1. The 'new' effective coordinates of the evaluation point $C_2(z_2, y_2)$, relative to the vortex ring central point give requirements 1-2, and ensure that in the upright domain, the relative position of the evaluation point and the vortex ring perimeter are the same. Additional checks are then performed to determine the relative angular location of the point in order to properly determine the radial induced velocity.

Equivalent Point Method

As stated above, the distance to the perimeter of the ring must be equal in both cases. Mathematically this is stated as

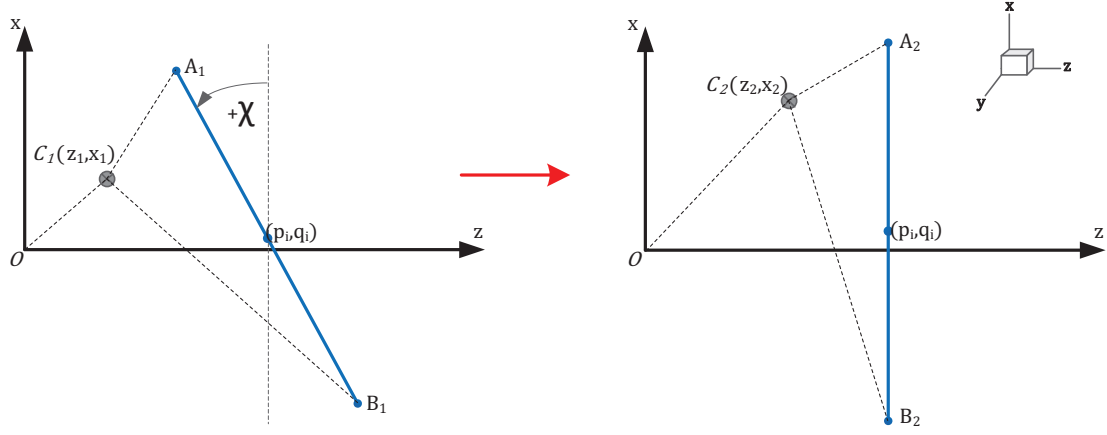


Figure B.1: (Left) Original ring orientation with evaluation point in the $x-z$ plane; (Right) Transformed coordinates about ring centre (p_i, q_i)

$$|\overrightarrow{C_1A_1}| = |\overrightarrow{C_2A_2}| \quad (\text{B.1})$$

$$\text{and } |\overrightarrow{C_1B_1}| = |\overrightarrow{C_2B_2}| \quad (\text{B.2})$$

Graphically, it can be thought that the locus of C about the ring extremities A and B must be the same. Stated analytically, and taking say relation B.1, the circle prescribed by rotating C_1 about A_1 gives:

$$|\overrightarrow{C_1A_1}|^2 = [(R_i \cos \chi_i + q_i) - x_1]^2 + [(-R_i \sin \chi_i + p_i) - z_1]^2 \quad (\text{B.3})$$

Similarly,

$$|\overrightarrow{C_1B_1}|^2 = [(R_i \cos \chi_i - q_i) + x_1]^2 + [(R_i \sin \chi_i + p_i) - z_1]^2 \quad (\text{B.4})$$

In analytical terms, the locus of point C_2 about say point A_2 can be described as a general circle equation. This should be equivalent to the distance $|\overrightarrow{C_1A_1}|$:

$$|\overrightarrow{C_1A_1}| = [z - p_i]^2 + [x - (R_i + q_i)]^2 \quad (\text{B.5})$$

Considering the point C_2 and rewriting eqn. B.5,

$$|\overrightarrow{C_1A_1}| = [z_2 - p_i]^2 + [x_2 - (R_i + q_i)]^2 = |\overrightarrow{C_2A_2}| \quad (\text{B.6})$$

Moreover, in the transformed domain, the displacement $|\overrightarrow{C_2B_2}|$ is given by:

$$|\overrightarrow{C_1B_1}| = [-z_2 + p_i]^2 + [x_2 + (R_i - q_i)]^2 = |\overrightarrow{C_2B_2}| \quad (\text{B.7})$$

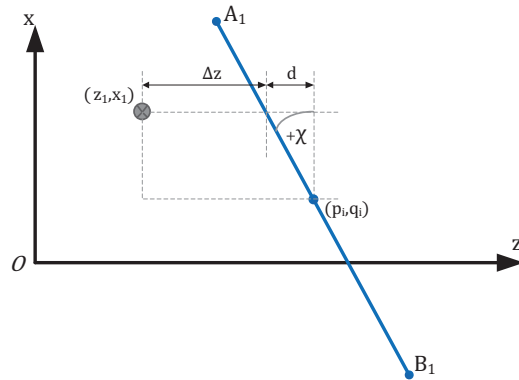


Figure B.2: Schematic showing the method for the correct root selection in eqn. B.11

The unknowns to be solved for here are the coordinates of C_2 , z_2 and x_2 . Subtracting eqn. B.3 from eqn. B.4 and denoting this quantity as Δ_1

$$\Delta_1 = 4R_i [(p_i - z_1) \sin \chi_i - (q_i - x_1)] \quad (\text{B.8})$$

From the transformed domain we obtain a similar expression after subtracting eqn. B.6 from eqn. B.7. This quantity should also be equal to Δ_1 . Hence,

$$\Delta_1 = 4R_i [x_2 - q_i] \quad (\text{B.9})$$

Equating eqn. B.8 and eqn. B.9 a solution for the unknown coordinate y_2 is obtained:

$$x_2 = (x_1 - q_i) \cos \chi_i + (p_i - z_1) \sin \chi_i + q_i \quad (\text{B.10})$$

To obtain an expression for the relative axial location, the newly found x_2 is substituted into eqn. B.6. Hence,

$$z_2 = p_i + a [(p_i^2 - 2p_i z_1 + z_1^2) \cos^2 \chi_i + (q_i^2 - 2q_i x_1 + x_1^2) \sin^2 \chi_i - (x_1 - q_i)(p_i - z_1) \sin(2\chi_i)]^{0.5} \quad (\text{B.11})$$

where a is a multiplier which takes a value dependent on the correct root to be chosen. From simple geometric considerations and with reference Fig. B.2,

$$\begin{aligned} \Delta z &= z_1 - [p_i - d] \\ &= z_1 - [p_i - (x_1 - q_i) \tan \chi_i] \end{aligned} \quad (\text{B.12})$$

The root is then selected according to the following:

$$a = \begin{cases} -1, & \text{for } \{\Delta z < 0\} \\ +1, & \text{for } \{\Delta z > 0\} \\ 0, & \text{for } \{\Delta z = 0\} \end{cases} \quad (\text{B.13})$$

B.0.2 Combined tilting and skewing

A similar analysis can be performed for a tilted ring, as shown in Fig. B.3. By applying the EPM successively for skew and tilt, the required spacings can be obtained. The equations for a tilted ring have a similar form and are given below:

$$y_2 = (y_1 - q_i) \cos \beta_i + (p_i - z_2) \sin \beta_i + q_i \quad (\text{B.14})$$

$$z_3 = p_i + a \left[(p_i^2 - 2p_i z_2 + z_2^2) \cos^2 \beta_i + (q_i^2 - 2q_i y_1 + y_1^2) \sin^2 \beta_i - (y_1 - q_i)(p_i - z_2) \sin(2\beta_i) \right]^{0.5} \quad (\text{B.15})$$

For selecting the correct root it is again necessary to evaluate:

$$\Delta z = z_2 - [p_i - (y_1 - q_i) \tan \beta_i] \quad (\text{B.16})$$

where multiplier a is selected according to B.13.

Thus, the procedure for finding the relative axial position, radial position and relative angular position of the evaluation point and an arbitrarily aligned vortex ring is as follows:

1. Calculate the equivalent coordinates in the $x - z$ plane, i.e. x_2 and z_2
2. Use the updated axial position z_2 for the second application of the EPM
3. Update the equivalent coordinates (z_3, y_2) in the $y - z$ plane

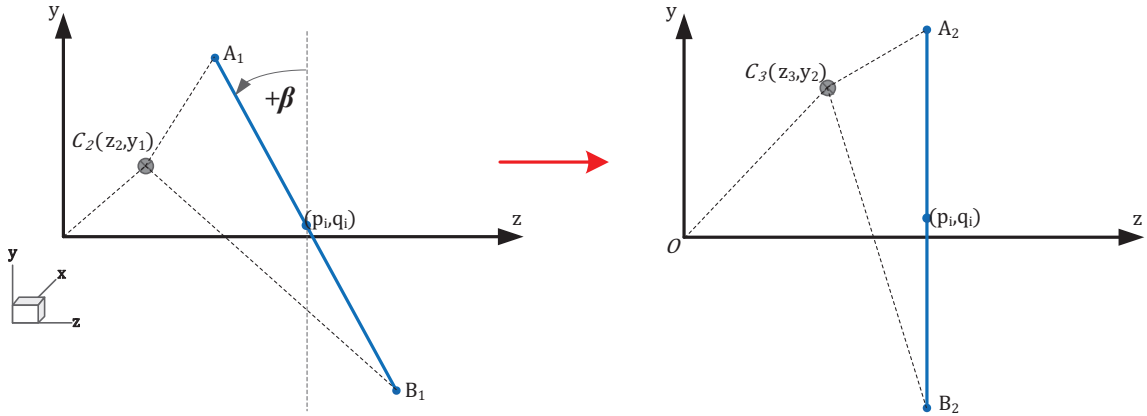


Figure B.3: (Left) Original ring orientation with evaluation point in the $y - z$ plane; (Right) Transformed coordinates about ring centre (p_i, q_i)

Finally, the radial distance of the evaluation point from the central ring axis is simply

$$r = \sqrt{(x_2^2 + y_2^2)} \quad (\text{B.17})$$

Vortex ring approximation using straight vortex line filaments

C.1 Biot Savart Law for the induced velocity from a line filament

The induction due to a straight, continuous segment of vorticity is given by the *Biot-Savart* law. Initially, use of this relation was a carry-over from the field of electro-magnetics, and the analogy is indeed strikingly similar.

Consider a directed segment along the approximated vortex ring as shown in Figure C.1. A small element $d\mathbf{l}$ along this segment, displaced by a vector \mathbf{r} from an arbitrary point P in space, induces a velocity as such:

$$\mathbf{V} = \frac{\Gamma}{4\pi} \frac{d\mathbf{l} \times \mathbf{r}}{|\mathbf{r}|^3} \quad (\text{C.1})$$

For this simple 2D case, the vector product can sufficiently be replaced by

$$d\mathbf{l} \times \mathbf{r} = |d\mathbf{l}| \cdot |\mathbf{r}| \sin(\alpha) \quad (\text{C.2})$$

Therefore,

$$\frac{d\mathbf{l} \times \mathbf{r}}{|\mathbf{r}|^3} = \frac{dl \cdot r \cdot \sin(\alpha)}{r^3} = \frac{dl \cdot \sin(\alpha)}{r^2} \quad (\text{C.3})$$

Furthermore, the following simple geometric relations are identified:

$$l = \frac{-h}{\tan(\alpha)} \quad (\text{C.4})$$

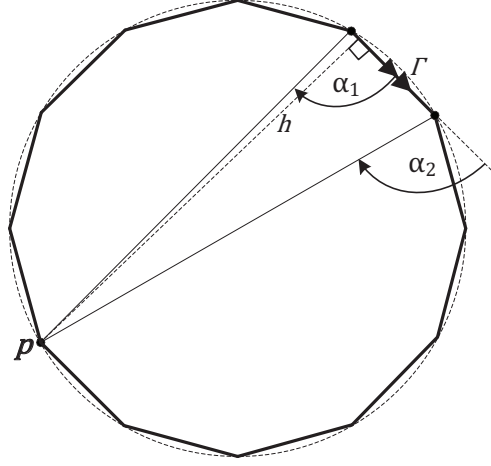


Figure C.1: Vortex ring approximation using a closed loop of consecutive straight line filaments. Notation is shown for filament i for an arbitrary ring composed of n discrete vortex filaments.

$$r = \frac{h}{\sin(\alpha)} \quad (\text{C.5})$$

Taking the differential form of (C.4),

$$dl = \frac{-h}{\sin^2(\alpha)} d\alpha \quad (\text{C.6})$$

Substituting C.6 and C.5 in C.3, and back into the main BS equation (C.9), we get the main Biot-Savart integral. Studying the diagram in Figure C.1, it is evident that the limits of integration are dependent on the position of point P .

$$V = -\frac{\Gamma}{4\pi h} \int_{\alpha_1}^{\alpha_2} \sin(\alpha) d\alpha = -\frac{\Gamma}{4\pi h} [\cos(\alpha)]_{\alpha_1}^{\alpha_2} \quad (\text{C.7})$$

Hence the induced velocity from the line vortex segment at any point P , subtending angles α_1 and α_2 to the extremities of the lines segment, is given by

$$V = \frac{\Gamma}{4\pi h} [\cos(\alpha_1) - \cos(\alpha_2)] \quad (\text{C.8})$$

C.2 Correction for finite core size

Within the vortex core, for $r < r_c$, viscous effects are present which are inherently not taken into account in the potential flow description. Inside the vortex core, the fluid rotates almost as a rigid solid rotating body with a velocity proportional to the radial location from the core centre. Outside the vortex core, $r > r_c$, the flow field is then described using potential flow theory.

Two commonly adopted core models which essentially describe vortex flow are used. The models may then be implemented through a viscous correction coefficient to modify the BS velocity as such,

$$\mathbf{V} = \frac{\Gamma}{4\pi} \frac{d\mathbf{l} \times \mathbf{r}}{|\mathbf{r}|^3} \quad (\text{C.9})$$

where,

$$K_v = \frac{h^2}{(h^{2k} + r_c^{2k})^{1/k}} \quad (\text{C.10})$$

The use of the viscous parameter in this way effectively removes the singularity predicted by the Bio-Savart law for the swirl velocity and modifies the velocity field depending on the proximity to the core.

Referring back to equation C.8, expressing the total velocity induced at a location of the ring in terms of the degree of the discretisation n (i.e. the number of representative line filaments), the predicted ring velocity using this method of approximation manifests itself as,

$$u_{z,p} = \sum_{i=1}^n \frac{h_{ip}^2}{(h_{ip}^{2k} + r_c^{2k})^{1/k}} \cdot \frac{\Gamma}{4\pi h_{ip}} [\cos(\alpha_{1,ip}) - \cos(\alpha_{2,ip})] \quad (\text{C.11})$$

Verification Trajectories of Meleshko et al. [3]

The spatial interaction trajectories for the dual and triple vortex ring system used for verifying the model are detailed in Meleshko et al. [3]. The plots are reproduced here for completeness.

Figure D.1 shows sample trajectories for a dual ring system which results in only a slip through motion and one depicting leapfrogging motion. This author also presents the range for the initial ring system parameters such that leapfrogging can occur. Such a graph is useful in determining the predicted stability of a vortex ring system containing two vortex rings.

Very good predictions were obtained through what are now known as *Dyson's Theorems*. Regions of permissible initial ring parameters, namely the relative ring radii, spacing and strengths are shown in Figure D.1b.

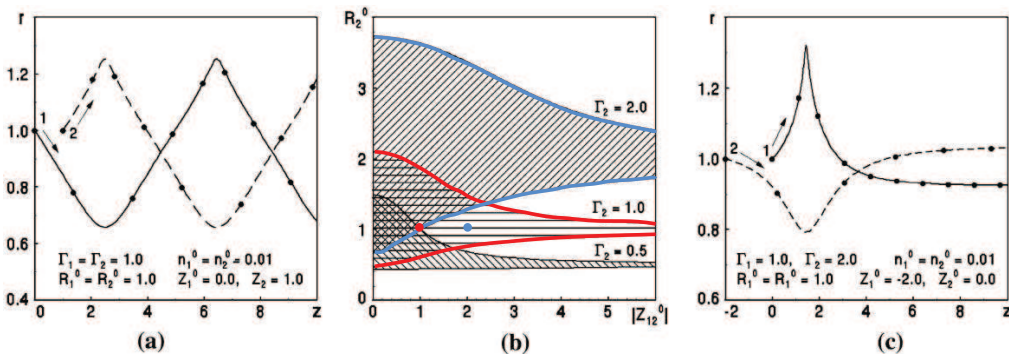
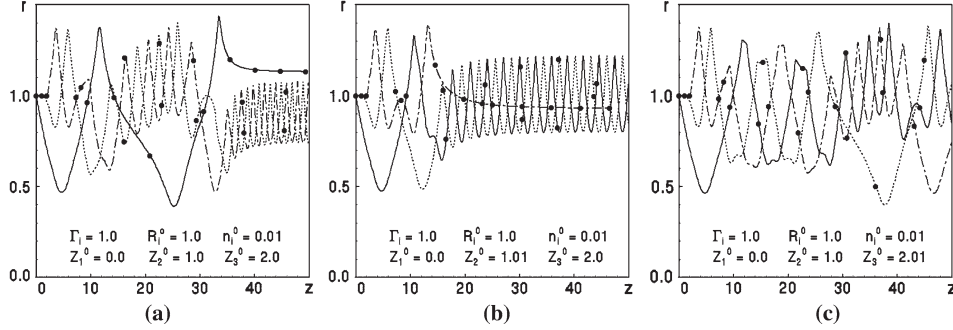
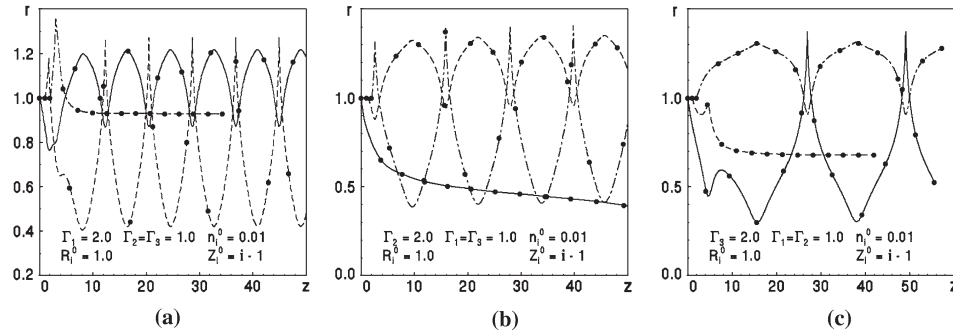


Figure D.1: Trajectories of a dual vortex ring system with equal and similar strength. (a) Mutual threading (b) Initial radii and ring separation constraints at various strengths giving rise to leapfrogging - shaded regions display possible combinations (c) Slip-through motion. *Source:* Meleshko et al. [3].

The spatial trajectories for the triple ring system are presented in Figure D.2a for a system with a vortex ring pitch disturbance and for a disturbance in the relative strengths in Figure D.2b.



(a) Triple vortex ring system trajectories, with constant strength and radius, and a small variation in initial axial spacing. *Source:* Meleshko et al. [3].



(b) Triple vortex ring system trajectories, with (a) identical ring parameters and spacing; (b,c) and a variation in the initial relative strengths. *Source:* Meleshko et al. [3].

Figure D.2: Vortex Ring trajectories computed with a fourth order Runge-Kutta estimation

Appendix E

Vortex ring array velocity fields

The mutual interaction of vortex rings is illustrated in this Appendix in the form of velocity contours. Additional insight is obtained with respect to the ground effect through isolating the perturbation caused by the ground mirroring effect - this is seen in subfigures (c) in the following figures of this Appendix. The effect of the presence of the ground plane on the flow profile of the vortex rings decreases with increasing displacement from the ground plane and although the contribution to the velocity field is only slight, it distorts the velocity field and hence destabilises the ring system.

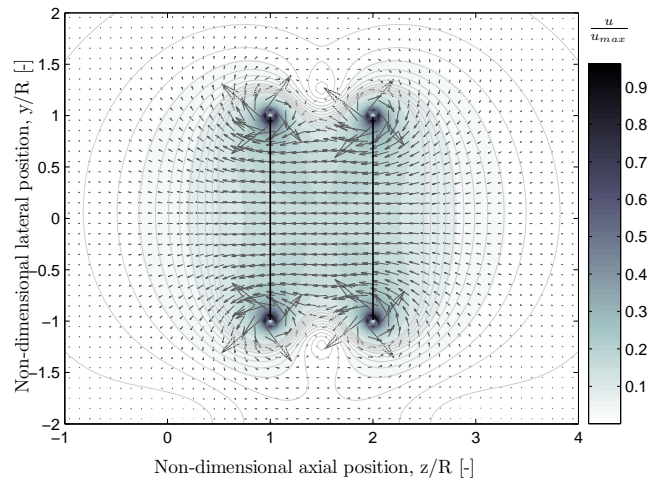
In Figures E.1 and E.2, the velocity field due to an upright and inclined dual vortex ring array is shown respectively. Similarly, Figures E.3 and E.4 depict a triple vortex ring system. The ring radii, spacing and strength are equal to unity and the rings have the same sense of rotation. The relative distance from the ground plane $HH/R = 2$ in all cases shown.

The velocities shown are the total field velocity u , the mutual induced component u^m and the ground (or virtual) induced component u_v . These have been normalised by the maximum total velocity u_{max} so as to show the relative influence of the mutually and virtually induced components.

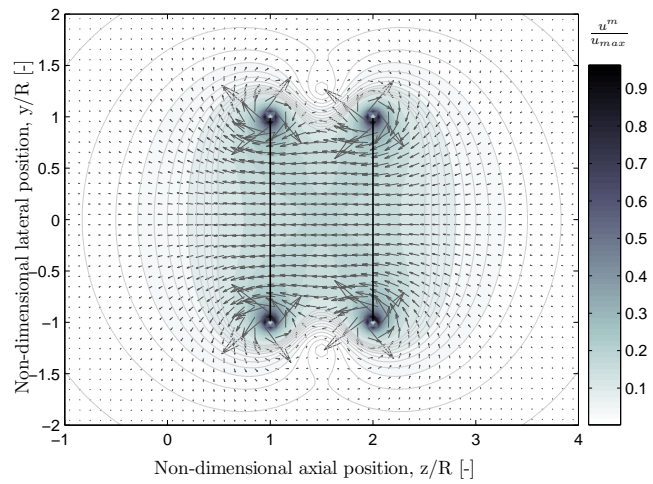
The total velocity plot of Figure E.3 shows that this has a stabilising effect on the middle ring from the first and third ring and in general applies to larger ring systems, as shown for clarity in Figure E.5a. The axial induced at the centre ring is highest due to the compounding effect of the adjacent rings, whereas the opposite can be said of the radial induced velocity component where it should theoretically be perfectly balanced by the upstream and downstream rings.

Note that as should be the case, the mutually induced velocity field shows symmetry about the ring system centreline and meridian plane in both upright cases. The ground effect also gives rise to a symmetric velocity field about the meridian plane, but as already mentioned, the magnitude decreases on moving away from the ground plane. In the inclined cases, an asymmetric velocity field results from the inclined rings, and the ensuing distorted effect from the ground, as is seen for instance in Figure E.4c. The slightly distorted contours

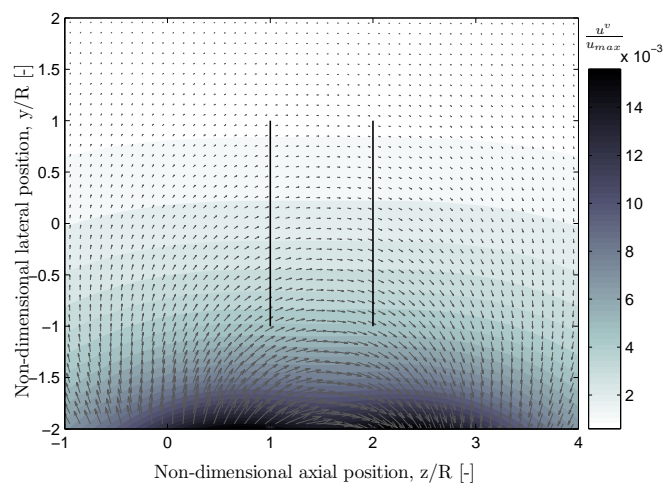
in the total velocity plots (subfigures (a)) are thus also a result of the ground effect. The implementation of the ground model can additionally be verified by looking at velocities induced at the ground plane. The resultant normal components are seen to be cancelled completely, satisfying the zero-flow boundary condition at the ground plane.



(a) Net induced velocities

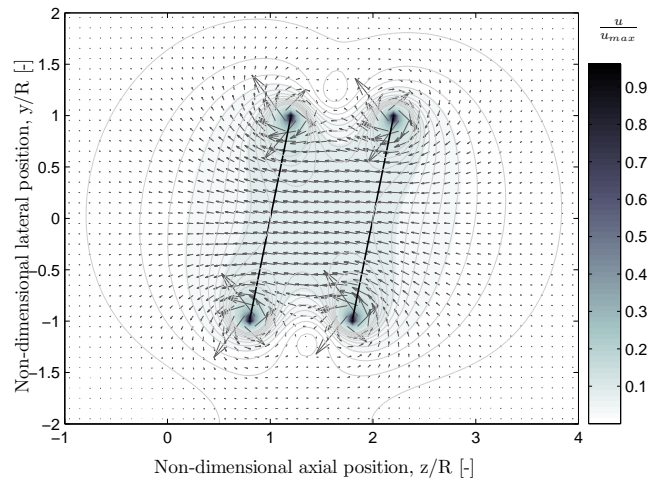


(b) Actual IVR array contribution

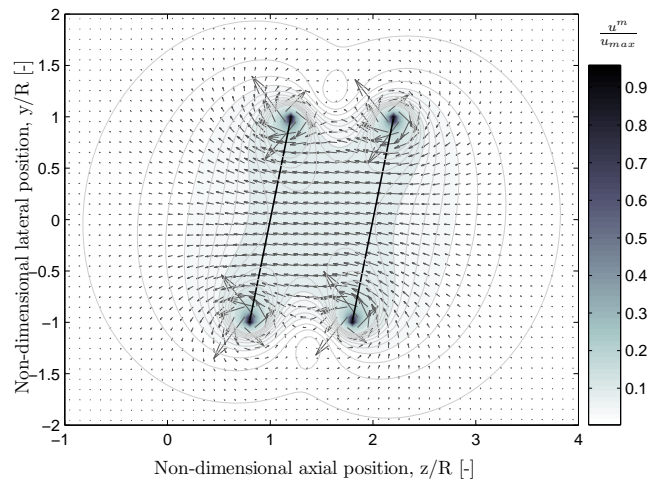


(c) Virtual IVR array contribution (ground effect)

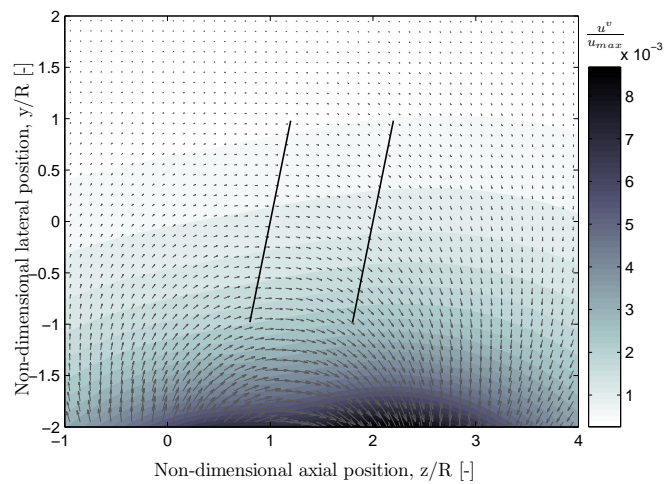
Figure E.1: Influence of ground effect on an array of 2 equispaced, upright IVRs; Unit strength, $HH/R = 2$



(a) Net induced velocities

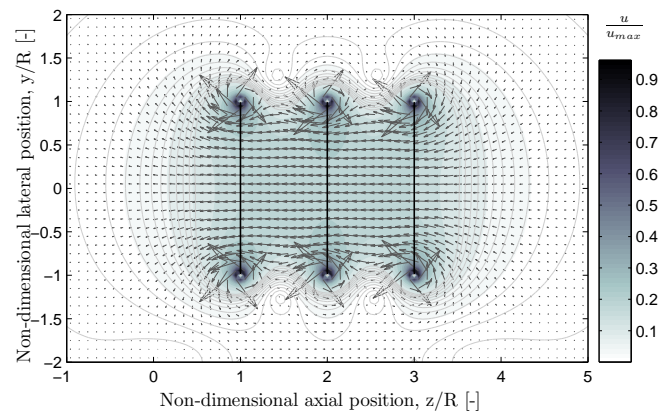


(b) Actual IVR array contribution

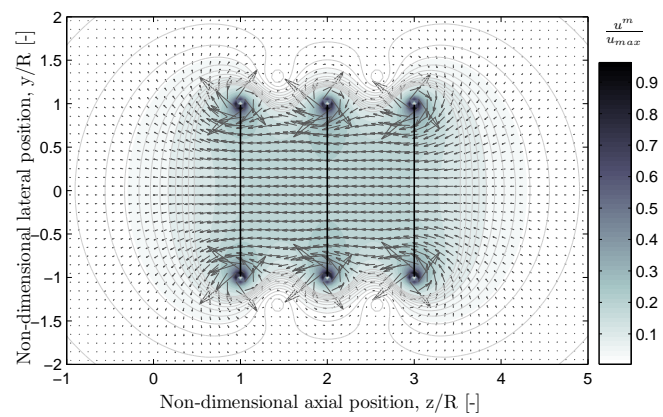


(c) Virtual IVR array contribution (ground effect)

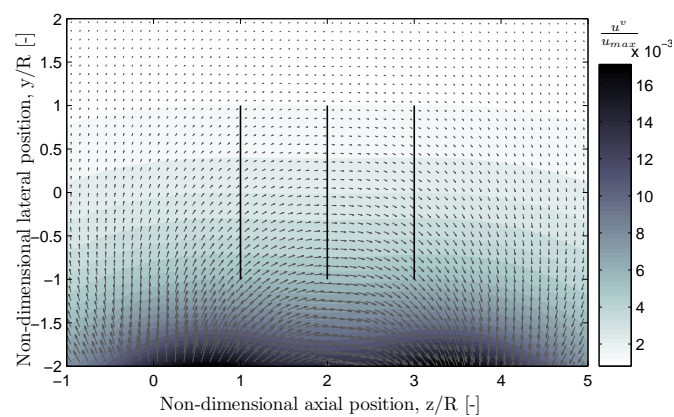
Figure E.2: Influence of ground effect on an array of 2 equispaced, $-0.2rad$ IVRs; Unit strength, $HH/R = 2$



(a) Net induced velocities

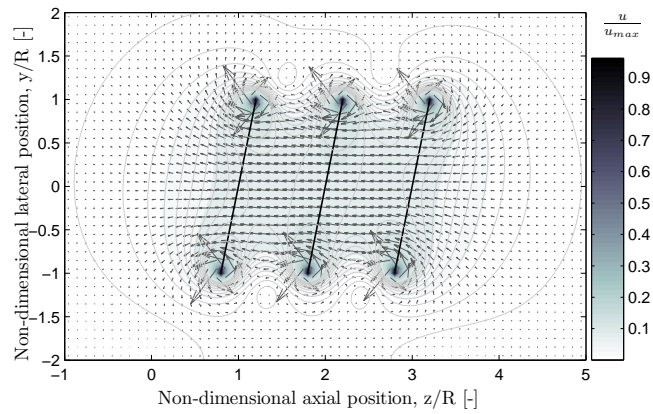


(b) Actual IVR array contribution

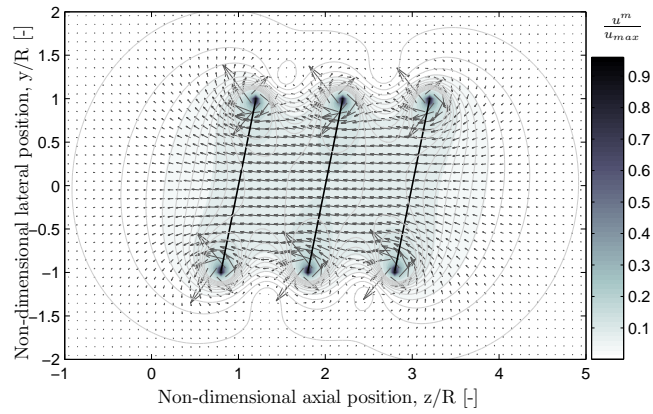


(c) Virtual IVR array contribution (ground effect)

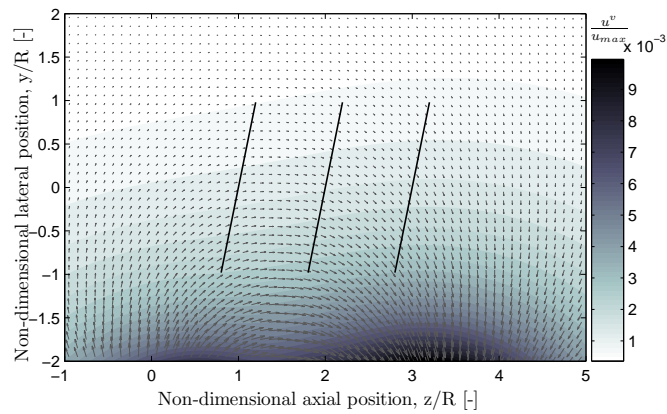
Figure E.3: Influence of ground effect on an array of 2 equispaced, upright IVRs; Unit strength, $HH/R = 2$



(a) Net induced velocities

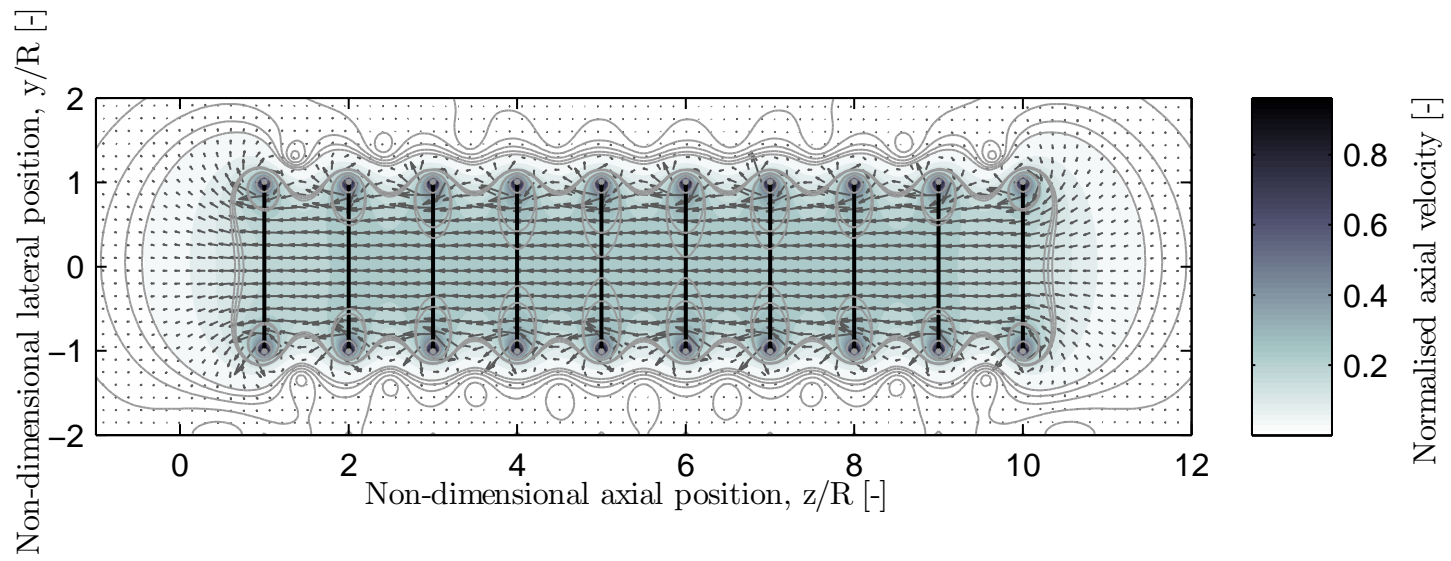


(b) Actual IVR array contribution



(c) Virtual IVR array contribution (ground effect)

Figure E.4: Influence of ground effect on an array of 3 equispaced, $-0.2rad$ IVRs; Unit strength, $HH/R = 2$



(a) Net induced velocities

Figure E.5: Total velocity contours for a 10 ring vortex ring system in ground effect

Wake visualisations

F.1 Discrete FW-VRM

F.1.1 Starting effect on ring dynamics

As described in section, it is understandable that the first ring initiated in the simulation (denoted as the *old* ring) experiences a significantly different velocity field to new rings, or rings located at mid-wake. In comparison with mid-wake rings in particular, the old rings experience an unbalanced field and thus tend to behave in a much more dynamically chaotic manner. Some of the observations on these *old* rings which led to their behaviour being "disregarded" include the following traits:

- overlapping of other vortex rings, suggested interaction of vortex filaments
- rotation beyond realistic limits, sometimes even performed a full rotation about the centroid

As with most other parameters studied, this unrealistic behaviour becomes more prominent with stronger ring vorticity, as well as with older wake age. One such case is illustrated in Figure F.1.

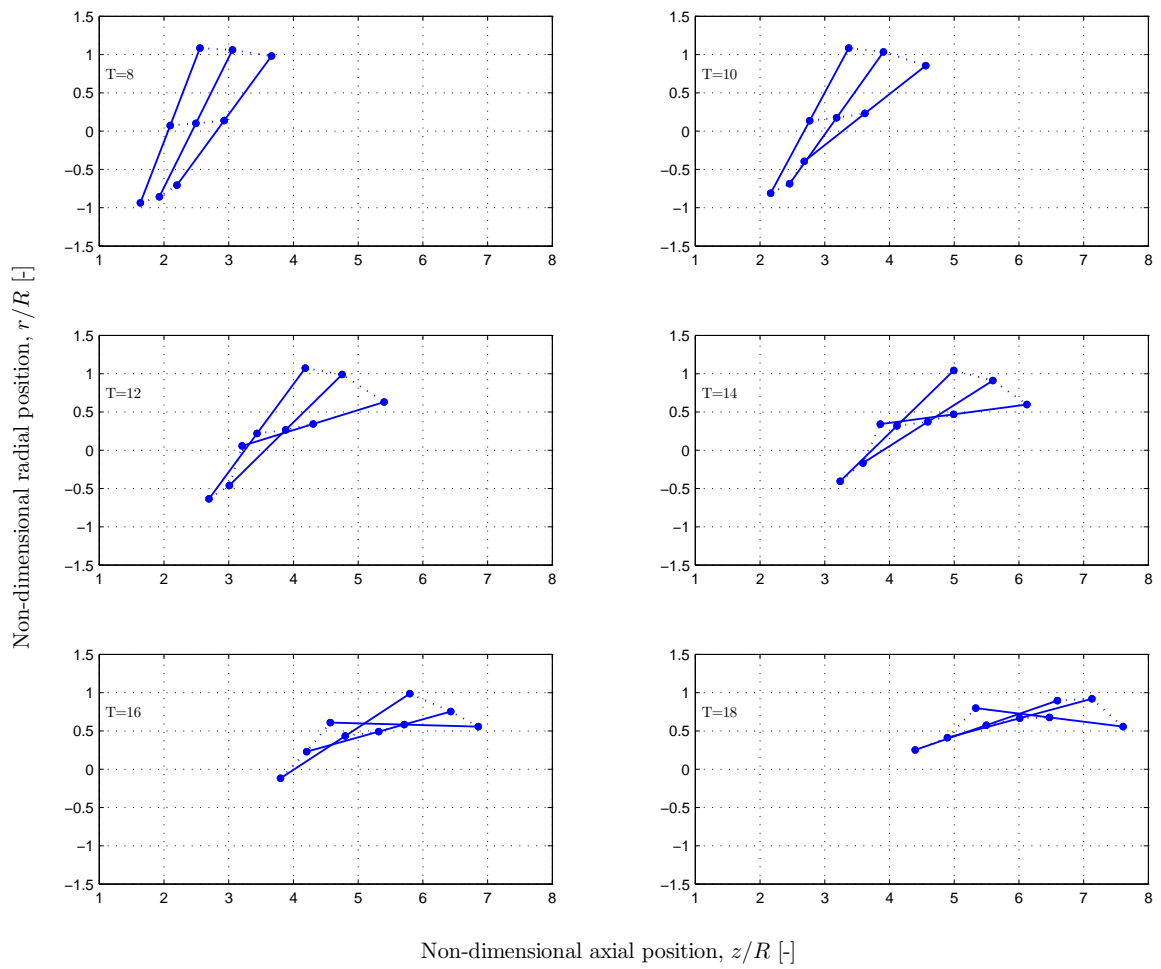


Figure F.1: Effect of unbalanced velocity field on the dynamics of the first three starting rings; $C_T = 0.889$, $m = 0.2$.